Nikolaos K. Voulgarakis

Nonlinear Localization In Model Systems And Materials

Physical properties of nonlinear localized modes in extended systems, quasi-one-dimensional PtCl and crystalline Si

A Dissertation
submitted to the Physics Department, University of Crete
in partial fulfillment of the requirements for the Degree
of Doctor of Philosophy in Physics

University of Crete

Department of Physics
2002

To my parents and my sister

PhD Thesis

Nonlinear Localization in Model Systems and Materials

Physical properties of nonlinear localized modes in extended systems, quasi-one-dimensional PtCl and crystalline Si.

Thesis author: N. K. Voulgarakis

Thesis supervisor: Prof. G. P. Tsironis

Thesis committee:

G. P. Tsironis — Thesis supervisor

S. H. Anastasiadis — Member

E. N. Economou — Member

N. Flytzanis — Member

P. C. Kelires — Member

N. Kylafis — Member

I. E. Perakis — Member

Physics Department - University of Crete
Heraklion - Greece

December - 2002

ACKNOWLEDGMENTS

Firstly, I wish to express my appreciation to my supervisor, Professor George Tsironis, for providing me with valuable guidance and assistance during the preparation of this dissertation. Without his patience and encouragement this work would have never been completed.

I would also like to thank D. Hennig, G. Kalosakas, G. Archontis, S. Skourtis, P. Kelires, and G. Hadjisavvas for their pleasant and fruitful collaboration.

Many thanks to my close friends for all the unforgettable moments we have shared during the last nine years in Heraklion. Special thanks go to postgraduate students of the Physics Department for their moral support and being there when I needed them.

Finally, I want to thank my parents Katerina and Kostas, and my sister Koula for their love, patience, and never ending support. Special thanks go to my sister for helping me to keep myself in one piece in the difficult periods of this study.

Contents

CHAPTER 1

INTRODUCTION

Understanding the physical mechanism and processes involved in microscopic energy storage and transfer in extended systems is a topic of importance for condensed matter physics and additionally may have important ramifications for molecular biology and biologically motivated physics. This issue provides with a challenge that has motivated many theoretical physicists during the last century and remains of great interest today. Generally, most theoretical studies associated with this problem revolve around the following two-fold question: What is the origin of energy localization and how does localized energy can propagate coherently, with no dispersion throughout a lattice? Although the first part of the question is sufficiently addressed in the literature, the mechanism for localized energy transfer is still an open problem.

It is well known that in translationally invariant systems modeled through harmonic lattices there is absence of localization: treating the system quantum mechanically we find that energy eigenvalues form energy bands accompanied by band gaps and the corresponding eigenstates are extended. Nevertheless, localized modes can exist in linear systems when lattice periodicity is broken, for instance when the spacing between the atoms is slightly irregular. The energy eigenvalues of localized modes occur in the band gap of the energy spectrum. This phenomenon, first discussed by P.W. Anderson [1], is referred to as Anderson localization. These localization effects are strongest in one dimensional systems but can also exist in two and three dimensions when the disorder is sufficiently strong [2].

Localized states can also exist in translationally invariant systems if the latter are characterized by some type of nonlinearity. In general these *nonlinear localized states* can be classified in two categories depending on the origin of their anharmonicity. In the first category, nonlinearity is an intrinsic property of the system typically arising in chains of coupled anharmonic oscillators while in the second class, anharmonicity arises effectively through the coupling with other degrees of freedom, as in the case of electrons interacting with phonons. Systems described by coupled fields can be studied effectively in terms of a single field that contains however nonlinearity; this is accomplished through appropriate elimination procedure, where one of the fields is eliminated in the framework of a specific approximation.

The present dissertation focuses exclusively on issues related to energy localization induced by both intrinsic and effective anharminicity. In the next two sections, we briefly review polarons and breathers that are the most representative examples of nonlinear localized modes.

1.1 Polarons

Problems involving electron-phonon interaction are among the most investigated ones in solid state physics. When a free electron moves in a ionic crystal it distorts locally the lattice and this lattice deformation leads to the creation of an effective potential that could trap the electron. This process is usually called *self-trapping*, because the distortion that tends to bind the electron is created by the electron itself. The localized electron accompanied by its own lattice distortion is called *polaron*, a term derived from the fact that this type of self-localization was initially found in polar materials.

The history of studies of electron self-localization in crystals due to the interaction with phonons begins in 1933, when Landau introduced the concept of polaron in an attempt to explain the optical properties in alkali halides [3]. Following this original work, a great deal of theoretical studies have been devoted to the phenomenon of polaron formation and its dynamical properties [4–15]. Despite of this extensive work, the polaron problem remains unsolved due to its high complexity stemming from the electron-phonon interaction. Standard perturbation and variational approaches are usually limited to a particular parameter regime. Numerical approaches, such as Monte Carlo calculations [16] and exact diagonalizations [17] can give accurate results but

they are computationally expensive and restricted only in small systems. Despite of the great difficulty of the problem, several successful analytical and numerical approaches have developed that deal with physical properties of polarons.

Polaron theory can also be extended in the case of two electrons interacting with phonons. In that case the localized state of the two electrons with opposite spins is called bipolaron; the theoretical analysis of bipolarons is similar to that of polarons. The most sophisticated approach to the bipolaron theory was given by Alexandrov and Ranninger [18] in 1981. They found that in the limit of strong electron-phonon coupling, small bipolarons can behave as a quantum boson liquid that condenses into a superfluid state. As a result, a charged superfluid liquid can be superconducting. The most attractive result of this theory is the prediction of existence of high T_c superconducting states. However there are two serious criticisms to bipolaronic superconductivity that dispute its validity for realistic physical parameters: *(i)* Bipolaron effective mass is so large that their quantum character completely disappears and *(ii)* High T_c temperature estimations in the limit of high carrier concentration neglect the strong bipolaron interaction that can destroy the bipolaron structure. Starting from the first criticism, Emin and Hillery [19] and Proville and Aubry [20] have extended bipolaron theory assuming long range electron-electron interaction and intersite bipolaron formation respectively and show that bipolarons effective mass is remarkably reduced. As a result bipolarons can be mobile. The second disadvantage of bipolaronic superconductivity has not been sufficiently analyzed. Further studies should be done to investigate the limit of large electron densities and how this situation affects the bipolaron structure.

Another extension of polaron theory was proposed by Davydov [21] in 1973 in order to explain how the energy released by hydrolysis of adenosine triphosphate (ATP) is stored and transferred in proteins. He suggested that ATP could be converted in Amide I vibrational energy ($C = 0$ stretching) of the fundamental peptide group (H$-$N$-$C$=$O) of proteins. Moreover, he proposed that Amide I vibrational energy would not disperse due to the coupling with the longitudinal displacements of the hydrogen bonded peptide groups. Treating the lattice vibration classically and Amide I quantum mechanically the problem is finally reduced to that of a polaron; Amide I is self-trapped in

the protein due to the interaction with the lattice. In the continuum limit, where the Davydov model is reduced to the Nonlinear Schrodinger equation (NLS), this self trapped state can propagate coherently throughout the protein with constant velocity. This solution is also referred to as Davydov soliton. Solitons present a different case of nonlinear localization and will be discussed briefly in the following section.

1.2 Discrete Breathers

Rigorously, solitons are localized solutions of completely integrable continuous nonlinear systems. Solitons can be either static (topological solitons) or travel with a constant velocity (non-topologiacal solitons). Another type of a soliton-like mode that is additionally time-periodic is a breather that has been found in the Sine-Gordon equation that present a special family of integrable systems. These solutions are exact, however they are unstable and disappear under small perturbations. The reason for the breather decay is very simple. Since the breather frequency lies in the *unbounded* spectrum of the continuous system a small perturbation can easily turn on a resonance with linear modes. The latter, due to their extended character, can carry away the energy and any attempt for having localized solution is destroyed. Recently, Sievers and Takeno [22] found, a more generic long-lived breather solution that exists in *discrete nonlinear* systems. This spatially localized and time-periodic solution is termed *Discrete Breather (DB)* or *Intrinsic Localized Mode* (ILM). Both discreteness and nonlinearity are equally important for the stability of DBs. Discreteness gives bounded phonon spectrum and nonlinearity controls the breather frequency. Consequently, we can construct time periodic solutions in the phonon gaps where the DB frequency is not in resonance with linear modes. The existence of DBs as exact solutions of discrete nonlinear systems was proven by rigorous theorems [23, 24] under quite general conditions. Since then, a large number of theoretical and numerical studies have been devoted to developing efficient construction methods and studying mobility [25] and thermodynamic [26–29] properties of discrete breathers. Recently there has also been an increasing interest in the quantum character of breathers. Numerical diagonalization in anharmonic lattices [30] or strong electron-lattice coupled systems [31] has shown the existence of many-phonon bound states. As the number of bounded phonons

increases the corresponding bandwidth decreases, i.e the states become more localized. This analysis has been performed in the case of two-phonon bound states (biphonons) quite early following an approach borrowed from Cooper pair formation.

Inspite the intense theoretical activity the only experimental candidate for DBs has been the anomalous temperature dependence of the Amide-I ($C = O$ stretching) band in ACN, attributed to a vibrational polaron formation [32–34]. Very recently, however, Resonant Raman scattering (RRS) measurements in PtCl, a quasi one-dimensional charge density wave compound, have shown a strong red-shift of the overtones [35], that is related to many-phonon bound states. Furthermore discrete breathers have been experimentally observed in coupled optical wave guides [36, 37], in magnetic systems [38], in arrays of coupled Josephson junctions [39, 40], and possibly in myoglobin [41].

Perhaps, one of the most dynamic and developing field of nonlinear science is its terminology. We already have mentioned terms such as: polaron, bipolaron, soliton, self-trapped state, breather, discrete breather, ILM. In the literature one can find many more: lattice breathers, vibrons, polarobreather, rotobreather etc. Fortunately, the origin of localization is not as chaotic as the terminology. Localized solutions exist because the system is nonlinear. Consequently, a term as Nonlinear Localized Mode (NLM) probably would be better and more generic. In the present dissertation we shall avoid to introduce one more term for nonlinear localization. We shall use "polaron" for the electron-phonon interaction induced localization and "DB" or "ILM" for the vibrational energy localization. Historically, the term "Discrete Breather" was introduced by Peyrard, "Intrinsic Localized Mode" by Sievers and Takeno and as we already have mentioned, "polaron" by Landau.

1.3 Thesis Organization

The present dissertation has two parts; the first part is devoted to polarons (Chapters 2-5) while the second one to discrete breathers (Chapters 6-7). More specifically, in Chap. 2, we start with a brief review of polaron theory in the framework of the Holstein model. Subsequently, we introduce the Anharmonic Holstein Model (AHM) and study the polaron ground state

and its dynamical properties [42]. In Chap. 3, we consider a generalized Holstein model in which both electron and Amide I vibrational energy interacts with the lattice and study energy localization and transfer in a $\beta-$sheet protein model [43]. An extension of polaron theory in the case of many quanta Holstein model (MQHM) is presented in Chap. 4. In Chap. 5, we use the MQHM to fit experimental observations of intrinsic localized modes in PtCl [44]. In Chap. 6 we present a brief review of discrete breather theory and study thermodynamic properties of nonlinear lattices out of thermodynamic equilibrium [45]. In Chap. 7, we develop a practical method of breather construction that is efficient in complex systems [46]. Using this method we study DB properties in real systems such as benzene and silicon [47].

Part I

Polarons

CHAPTER 2

THE ANHARMONIC HOLSTEIN MODEL

In this Chapter, we study the semiclassical Holstein model with a hard nonlinear on-site potential in one, two and three dimensions. Using stationary solutions, we obtain the ground-state phase diagram as a function of the parameter characterizing the on-site nonlinear potential as well as the electron-phonon coupling. The basic result is that in the presence of the nonlinear on-site potential, medium and large polaron formation is also possible in two and three dimensions. Linearizing the equations of motion around the stationary solution, we calculate the normal modes and study their stability. Normal mode analysis shows the existence of a low-frequency pinning mode not only in 1D but also in 2D and 3D. This result enables us to construct numerically one- and two-dimensional moving polarons and study their mobility properties. The dramatic reduction of the polaron effective mass is the most characteristic effect of the lattice nonlinearity.

2.1 Introduction

Properties of electron self-localization in crystal lattices due to interaction with phonons constitutes one of the fundamental problems in condensed matter physics. This question has long history starting almost seven decades ago, when Landau [3] first introduced the concept of polaron, *i.e* the quasiparticle formed by an electron accompanied by its own lattice distortion. In the preceding decades many theoretical works [5–7, 9, 8, 10–15] have been devoted to the phenomenon of polaron formation. In general, the analytical studies are based on the adiabatic treatment of continuous or discrete models in the weak or strong electron-phonon coupling, following either variational or perturbation methods. Analytical results are in good agreement with the numerical calculations of finite-cluster exact diagonalizations [17] or Quantum Monte Carlo methods [16]. The general result is that while in one dimension (1D) the polaron (small or large) is always the ground state at any non-vanishing coupling strength, in higher dimensions only small polaron formation is possible and a minimum coupling is required for this purpose. Thus, due to their small size, two and three dimensional polarons are expected to be pinned rather than mobile. In one-dimensional large polarons on the other hand, where the continuum limit is valid, Davydov [21] has shown that solitary states are formed that can propagate uniformly in molecular chains. Furthermore, over the last two decades, real-time numerical simulations [13, 48, 49] in one dimensional models gave additional insight to the question of polaron formation and its dynamical properties.

It should be mentioned that all the above studies are restricted in the special case where the phonon on-site potential is quadratic. This assumption is sufficient to describe the main aspects of the polaron problem in the weak coupling limit, where the presence of the electron does not displace substantially the oscillators from their equilibrium position and the linear approximation is adequate. In the opposite limit of strong electron-lattice interaction, the oscillators are greatly perturbed from the equilibrium position and higher terms of the potential expansion should be taken into account. Although it would be interesting physically to consider such nonlinear effects, this aspect has not been addressed sufficiently and only in low dimensions [50–52].

The main aim of the work to be described below is the study of the Holstein model [7] including on-site lattice anharmonicity in one, two and three dimensions. We have assumed only hard lattice nonlinearity since, as will be explained in what follows, it results in more interesting dynamical behavior of the polaron.

The organization of this chapter is the following: In Sec. 2.2 we briefly review the Holstein model [7] and the main polaron properties. In the following sections we study the effects of lattice anharmonicity in the polaron formation and mobility properties. More specifically, in Sec. 2.3, we introduce the anharmonic Holstein model and derive the semiclassical equations of motion. In Sec. 2.4, we calculate numerically the adiabatic ground-state and discuss its modifications effected by the lattice nonlinearity. The following three sections are devoted to the polaron dynamical properties. More specifically in Sec. 2.5, we consider small oscillations around the adiabatic polaron solution and calculate its normal modes focusing our interest in the lower frequencies. The linear stability of the polaron solution is checked in Sec. 2.6. and the investigation of the possibility of having mobile polarons is performed in Sec. 2.7. Finally, in Sec. 2.8 we summarize and discuss our results.

2.2 The Holstein model

The starting point of the most quantitative calculations in the polaron theory is the Holstein Hamiltonian [7]. It is made up of the sum of three terms

$$H = H_{el} + H_{lat} + H_{int}, \tag{2.1}$$

The first term describes an electron in the tight binding approximation:

$$H_{el} = -J \sum_{i=1}^{N} \sum_{n_i} c_i^{\dagger} c_{n_i}, \tag{2.2}$$

where $c_i^{\dagger}$ and c_i are the electron creation and annihilation operators respectively at site i, and J is the hopping integral between the site i and its nearest neighbors n_i. The second term is the Hamiltonian of N identical anharmonic Einstein oscillators each with mass M :

$$H_{lat} = \frac{1}{2M} \sum_{i=1}^{N} p_i^2 + \frac{M\omega_0^2}{2} \sum_{i=1}^{N} x_i^2 \tag{2.3}$$

where p_i and x_i are the momentum and the displacement from the equilibrium position of the i-th oscillator respectively, and ω_0 is the harmonic vibrational frequency. The last term is the electron-lattice interaction

$$H_{int} = g\sum_{i=1}^{N} x_i c_i^{\dagger} c_i, \tag{2.4}$$

that is assumed to be only on-site. The electron-lattice coupling strength is given by g.

Treating the lattice classically and the electron quantum mechanically, we find that under straight-forward transformations the model is described by the following equations of motion [12]:

$$i\gamma\frac{dC_i}{d\tau} = -\sum_{n_i} C_{n_i} + ku_iC_i \tag{2.5}$$

and

$$\frac{d^2u_i}{d\tau^2} + u_i + k|C_i|^2 = 0, \tag{2.6}$$

where $\tau = \omega_0 t$ (dimensionless time), C_i is the normalized time-dependent probability amplitude to find the electron on site i, $u_i = \sqrt{M\omega_0^2/J}\ x_i$ (dimensionless displacement), $k = g/\sqrt{JM\omega_0^2}$ (dimensionless coupling), and $b = \beta\frac{J}{(M\omega_0^2)^2}$(nonlinear parameter). The parameter $\gamma = \hbar\omega_0/J$, is the so-called adiabatic parameter and gives a measure of the electronic effective mass (m_0) relative to the oscillators mass (M). This is clear if it is written as

$$\gamma = \alpha\sqrt{\frac{2m_0}{M}}, \tag{2.7}$$

where α is the the dimensionless lattice constant.

The total energy of the system is given by:

$$E_{tot} = -\sum_{i=1}^{N}\sum_{n_i} C_i^* C_{n_i} + \sum_{i=1}^{N}[\frac{1}{2}(\frac{du_i}{d\tau})^2 + \frac{1}{2}u_i^2] + k\sum_{i=1}^{N}|C_i|^2 u_i \tag{2.8}$$

where the first sum corresponds to the electronic kinetic energy (E_{el}), the second sum to to the lattice energy (E_{lat}), and the last one the interaction energy (E_{int}).

Here, it is worthwhile to review briefly what is known regarding the ground state properties of the polaron within the Holstein model (see for

example Ref. [11] and [12]). In the one dimensional case the polaron is always the ground state of the system independently of the electron-phonon coupling value. As a result, there is a smooth transition between small polarons, formed in the limit of the strong electron-lattice interaction and large polarons that are produced in the weak coupling limit. In two and three dimensions the picture changes qualitatively since the adiabatic energy has two minima one corresponding to polaronic and the other to delocalized states. While in 3D these minima are always separated by an energy barrier, in 2D there is a coupling region where the barrier vanishes and the delocalized state becomes unstable. Generally, there are two critical coupling values k_{c_1} and k_{c_2} that determine three different regions. For $k \geq k_{c_2}$ the polaron is always the ground state of the system. In the region where $k_{c_1} \leq k < k_{c_2}$ the polarons are metastable, *i.e* polaron formation is possible but its energy is higher than the energy of the corresponding delocalized state . For coupling values $k < k_{c_1}$ the ground state is completely delocalized with energy, in the limit of infinite lattice, $E_d = -2d$ (in units of J), where d =1,2 and 3 the dimensions of the lattice. It is important to notice that in all cases where polarons exist they are extended only to few lattice sites. Thus in 2D and 3D we do not have large polarons, except in the anharmonic Holstein model (AHM), as will be explained below.

2.3 Introduction to the Anharmonic Holstein Model

In order to study the effects of lattice nonlinearity in the Holstein model we introduce the hard ϕ^4 on-site potential

$$V(x_i) = \beta \frac{1}{4} x_i^4. \tag{2.9}$$

in the lattice Hamiltonian Eq. (2.3). The parameter that controls the lattice nonlinearity is given by β.

The main aim of this section is to study the ground state of the anharmonic Holstein model in the adiabatic approximation. According to the notation of the previous section, this treatment is valid when $\gamma \to 0$, *i.e* in the limit where the oscillators are much heavier than the electron ($M >> m_0$). In this case one can assume that the oscillators remain static ($\frac{du_i}{d\tau} = 0$) but respond to the probability amplitude that the electron is on a given site. The

localized solution in this approximation is what we shall call (stationary) polaron.

Since we have ignored the motion of the oscillators, the Hamiltonian becomes time independent and thus the probability amplitudes C_i can be written in the form

$$C_i = \Phi_i e^{-i\frac{E}{\gamma}\tau}, \tag{2.10}$$

where the coefficients Φ_i are time-independent and E is the electronic part of the total energy ($E = E_{el} + E_{int}$).

Using the stationary condition ($\frac{du_i}{d\tau} = 0$) and after substituting Eq. (2.10) into Eq. (2.6) we obtain a third order algebraic equation

$$bu_i^3 + u_i + k|\Phi_i|^2 = 0, \tag{2.11}$$

where $b = \beta\frac{J}{(M\omega_0^2)^2}$ is the dimensionless nonlinear parameter. The real solutions of Eq. (2.11) correspond to the displacement of the i-th oscillator. Since b and k are positive, it is easy to check that this equation has only one real and negative solution; let us represent this solution as $-|u_i(k, b, |\Phi_i|^2)|$. According to the previous analysis, the final form of the electronic eigenvalue equation is

$$E\Phi_i = -\sum_{n_i} \Phi_{n_i} - k|u_i(k, b, |\Phi_i|^2)|\Phi_i \tag{2.12}$$

2.4 Polaron ground state in the Anharmonic Holstein Model

The ground-state of the system is calculated following the same numerical procedure as in the work of Ref. [12]. In general, numerical calculations of the adiabatic ground state of the anharmonic Holstein model suggest that by increasing the nonlinear parameter the polarons become more extended in 1D as well as in 2D and 3D for a given electron-lattice coupling. This feature is clearly seen in Fig. **??**, where we present the polaron-size increase due to nonlinearity in all three dimensions. This behaviour is attributed to the fact that oscillators become more rigid by the presence of the hard on-site potential. Therefore, the potential well $-k|u_i(k, b, |\Phi_i|^2)|$ causing electron localization reduces and as a result the formation of larger polarons is favored.

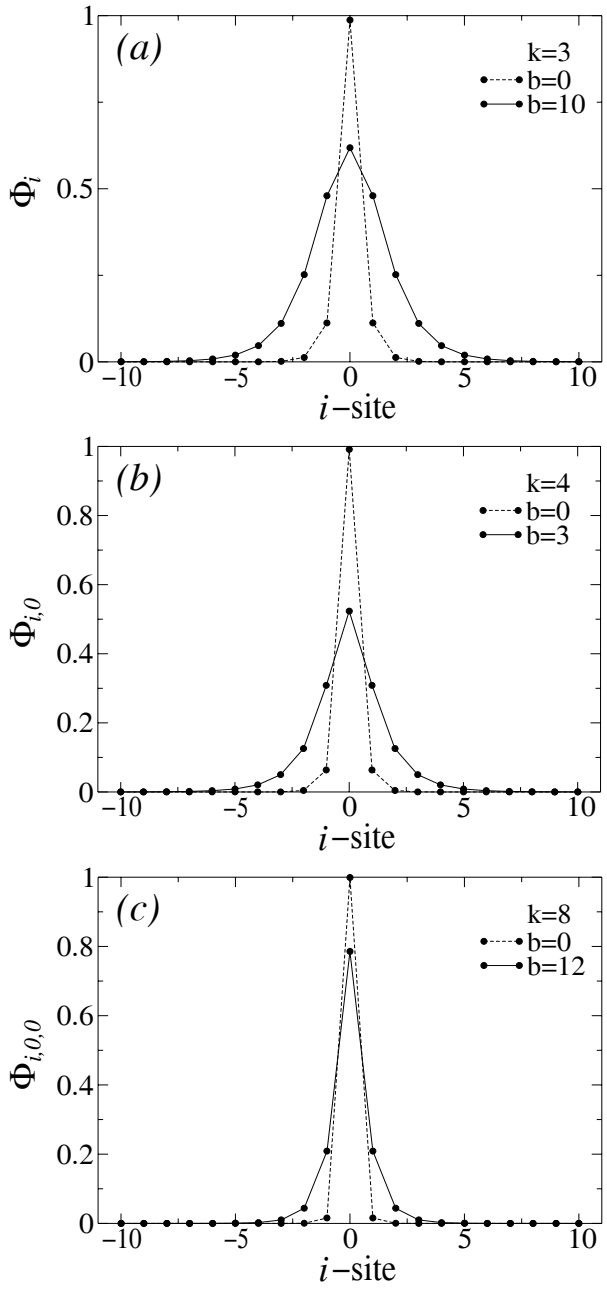

Figure 2.1: Polaron profile in (a) 1D, (b) 2D and (c) 3D for b=0 (dashed line) and for (a) b=10, (b) b=3, (c) b=12 (solid lines). In (a) k=3, (b) k=4, (c) k=8 The total number of sites is $N = 21^d$, where d =1,2 and 3 is the dimension of the lattice.

Similar results were obtained by Zolotaryuk *et al.* [53] through variational approach of a two-dimensional anharmonic model. It is important to notice that this polaron-size increase occurs only in the case of hard on-site lattice anharmonicity. In the case of soft anharmonicity the oscillators become more flexible and this leads to more polaron localization.

While in one dimensional case the polaron is always the ground state of the system at any no-zero coupling and for any value of b, in 2D and 3D the presence of nonlinearity changes the conditions of polaron formation. The first remarkable result, as shown in Fig. 2.2, is that the energy of both stable and metastable states is shifted closer to the energy of the delocalized states. This occurs because this polaron extension favors the kinetic term of the total energy.

It is important to notice that despite the remarkable reduction of the energy barrier due to lattice anharmonicity, the polaron metastable regions always exist for a range of coupling values. This result is also confirmed through variational approach of the ground-state energy. We comment that best variational results for the ground-state energy have been obtained using an exponential trial function for small or medium polarons and hyperbolic secant for large polarons. In the same figure is observed that the critical values k_{c_1} and k_{c_2} depend on the nonlinear parameter b. More specifically there is an increasing dependence of the critical coupling values on b. This is clearly seen in Fig. 2.3 where the ground state phase diagram is shown in 2D and 3D including the polaron metastable region as a function of the nonlinear parameter b and the electron-lattice k. It is also worthwhile noticing that in 2D case the metastable region reduces , for increasing values of b and approaches almost asymptotically a specific coupling value $k_s \simeq 3.4$. Thus for $k > k_s$ the polaron is always the ground state of the system independently of nonlinearity. Similar behavior has not been observed in 3D even for large but reasonable values of b and k. Following the area close to the line $k_{c_2}(b)$ for increasing values of b we observe a smooth transition between small and large polarons. It should be remarked that in order to obtain large polarons quite large values of b are required, while medium-size polaron formation is possible even for small value of b. Note that far away from this line the polaron-size is very small.

This increase of the polaron size in all three dimensions effected by the

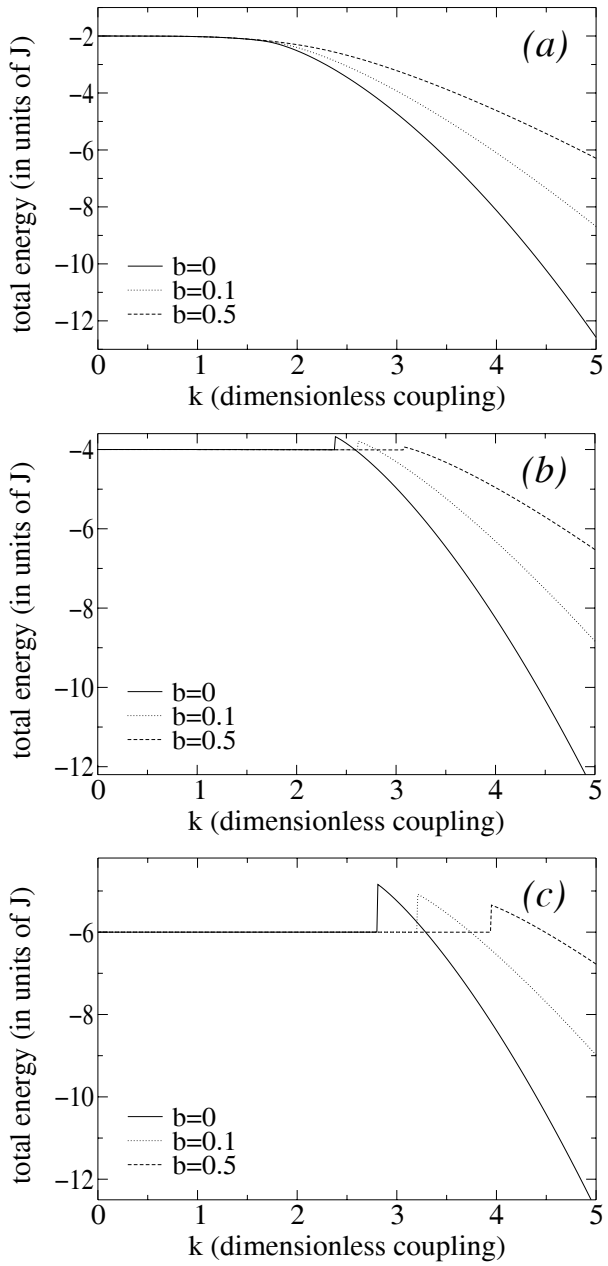

Figure 2.2: The total energy as a function of the coupling k in (a) 1D, (b) 2D and (c) 3D each for three different values of the nonlinear parameter: (i) b=0 (solid lines),(ii) b=0.1 (dotted lines), (iii) b=0.5 (dashed lines).

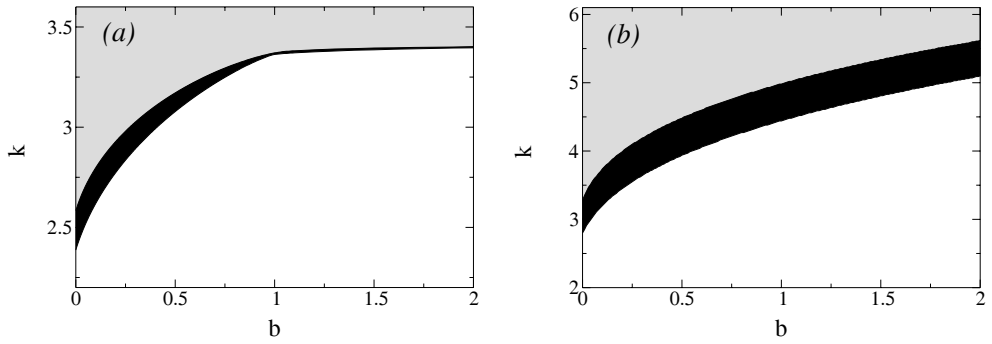

Figure 2.3: The ground-state phase diagram for (a) 2D, and (b) 3D. The grey area on the top of the diagrams corresponds to polaronic states while the white one on the bottom to delocalized states. The dark region in the middle corresponds to metastable polaronic states.

presence of hard lattice nonlinearity indicates interesting dynamical behavior since the medium or large polarons are expected to be mobile. The study of polaron dynamical properties in the anharmonic Holstein model is the main aim of the next two sections.

2.5 Polaron normal modes

In this section we focus on the study of the polaron normal modes in the nonadiabatic limit ($\gamma \neq 0$). For this purpose we consider small perturbations from the stationary solution Φ_i^0 and u_i^0:

$$C_i(\tau) = [\Phi_i^0 + \epsilon_i(\tau)]e^{-i\frac{E_0}{\gamma}\tau} \tag{2.13}$$

and

$$u_i(\tau) = u_i^0 + \delta_i(\tau), \tag{2.14}$$

where, in general, $\epsilon_i(\tau)$ are complex, $|\epsilon_i(\tau)|$ and $\delta_i(\tau)$ are very small time-dependent variables and E_0 corresponds to the electronic part of the stationary-solution energy. The linearized equations for the system are derived by substituting Eq. (2.13)-(2.14) into Eq. (2.5)-(2.6) and keeping only first order terms in $\epsilon_i(\tau)$ and $\delta_i(\tau)$. We obtain:

$$i\gamma\frac{d\epsilon_i}{d\tau} = -\sum_{n_i} \epsilon_{n_i} + (ku_i^0 - E_0)\epsilon_i + k\Phi_i^0\delta_i \tag{2.15}$$

and

$$\frac{d^2\delta_i}{d\tau^2} + [1 + bV''(u_i^0)]\delta_i + k\Phi_i^0(\epsilon_i + \epsilon_i^*) = 0, \tag{2.16}$$

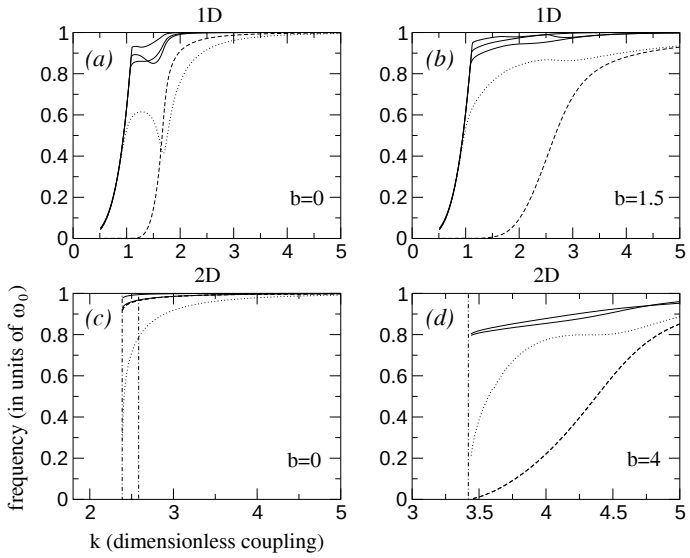

Figure 2.4: The five lower eigenfrequncies as a function of the coupling for two different values of b in (a), (b) 1D and (c), (d) 2D. The dashed lines correspond to pinning modes and the dotted to breathing mode. The dashed-dotted lines in (c) and (d) determine the k_{c_1} and k_{c_2}. For $b = 4$ in (d) the difference between the two critical values is not evidence.

Polaron normal modes are calculated by applying a Fourier transform of the linearized equations and expanding the electronic Fourier coefficients in the basis of the unperturbed problem. The analytical procedure followed in this work is similar to that of Ref. [12]. We present results through numerical diagonalizations of the eigenfrequency matrix in 1D and 2D focusing on the lower frequency polaron modes. In what follows, we restrict our study in the case of intermediate electron mass ($\gamma = 0.1$).

Let us first recall the existing results for the polaron normal modes in the case of the linear oscillators [12]. In 1D, as it is clearly seen in Fig. 2.4 (a), the nature of the lower mode changes from breathing to pinning mode in the transition region of small to large polarons. Contrary to this, in 2D (3D) the lower mode is always a breathing mode, while the next excited one is a doubly (triply) degenerated pinning mode. The abrupt change of the lower frequencies seen in Fig. 2.4 (a) for the 1D case for small k is associated to the fact that their character changes from phononic to electronic due to the considerable electronic motion in this parameter region. Similar behaviour has been observed in 2D (and 3D) despite the fact that it is not seen in the two-dimensional example of Fig. 2.4 (c). This phenomenon is more obvious

as the adiabatic parameter γ increases (for more details see Ref. [12]).

In the anharmonic case the eigenfrequency spectrum changes drastically. Not only are the electronic modes modified, but also a remarkable spreading of the phononic frequencies from 1 (in units of ω_0) is observed. In this work we present results only for the lower modes as they are easier excited. Fig. 2.4 (b)-(d) show the five lower polaron eigenfrequencies in 1D and 2D as a function of the electron-lattice coupling for different values of b. We note that the lowest frequency excited mode can be a pinning mode not only in 1D but also in 2D. Furthermore, it is observed that as the nonlinearity increases the frequency of the pinning mode is shifted to zero. This is significant since an excitation of a low frequency pinning mode could create suitable conditions for the polaron propagation in the lattice. This possibility as well as the linear stability of the polaron solutions are studied in the next section.

2.6 Linear stability analysis

Due to the condition of Eq. (2.10) the time evolution of the polarons described by (2.5) and (2.6) is periodic into the $4N$-dimensional phase space of the vector $\mathbf{V}(\tau) = \{ReC_i(\tau), ImC_i(\tau), u_i(\tau), \dot{u}_i(\tau),\ i = 1, ..., N\}$. The period of motion is $T = 2\pi\gamma/E_0$ and the frequency $\omega_T = E_0/\gamma$. The linear stability of these solutions is performed through Floquet analysis.

Integrating the corresponding linearized equations (2.15) and (2.16) over one period of time we construct the Floquet matrix $\mathbf{F}$ which gives the evolution of the initial set of the variables $\delta\mathbf{V}(0) = \{Re\epsilon_i(0), Im\epsilon_i(0), \delta_i(0), \dot{\delta}_i(0), i = 1, ..., N\}$ after time nT:

$$\delta\mathbf{V}(nT) = \mathbf{F}^n\delta\mathbf{V}(0), \tag{2.17}$$

where n is a positive integer number. Taking into account the restriction $\Sigma_i\Phi_i^0 Re\epsilon_i = 0$ (to first order of ϵ_i) due to the normalization condition, $\Sigma_i|C_i|^2 = 1$, we eliminate one of the variables $Re\epsilon_i$. Therefore, the dimension of $\mathbf{F}$ is reduced by one [12]. The linear stability of each polaron solution requires that all the $(4N-1)$ eigenvalues $r_n e^{i\theta_n}$ of Floquet matrix are lying on the unit cycle (i.e $r_n = 1$). Floquet analysis not only investigates the linear stability of the polarons but also gives us specific information regarding their normal modes. The relation between the eigenvalues of $\mathbf{F}$ and the

eigenfrequency of the corresponding normal mode is given by

$$\omega_\theta = \omega_T(\frac{\theta}{2\pi} + m), \tag{2.18}$$

where θ is in rad and m is an arbitrary integer number. Floquet matrix diagonalization for many sets of the system parameters has shown that all the corresponding polaron solutions are linear stable. An example of polaron linear stability in 1D and 2D is displayed in Fig. 2.5 (a) and 5(c) for different values of b and k, and for $\gamma = 0.1$.

2.7 Polaron mobility properties

Through Floquet analysis it is also possible to construct mobile polarons by applying a well-known numerical procedure used originally for discrete breathers [25]. This method is based on a appropriate perturbation of the velocity variables $\{\dot{u}_i\}$ in the direction of the corresponding part of the pinning-mode. More specifically, we follow the time evolution of polarons by integrating the Eq. (2.5) and (2.6) using the following initial conditions:

$$\mathbf{V}(0) = \{\Phi_i^0, 0, u_i^0, 0\} + \lambda\{0, 0, 0, \mathbf{v}_i\},\ i = 1, ...N, \tag{2.19}$$

where λ is the perturbation parameter and $\mathbf{v}$ the normalized velocity part of the pinning mode. It is important to notice that due to the lattice discreteness a minimum energy barrier must be overcomed in order to obtain mobile polarons, or equivalently the perturbation strength must be greater than a (minimum) critical value λ_c. This energy barrier, corresponding to an effective Peierls-Nabarro barrier, increases as the polaron becomes more localized and finally in the limit of small polaron, discreteness completely traps the polarons and rendens them immobile. As a result this method is applicable only in the case of medium or large polarons. In general, for large values of λ the polarons motion is accompanied with energy radiation and thus after some time the polaron solution can disappear. We also mention that while several pinning modes can be used to construct mobile polarons, in our study we chose only the lowest frequency pinning mode. This is done not only because this mode is easier excited but also because improves numerically the stability of polaron motion.

We note that in 2D, due to the square lattice symmetry the pinning-mode is doubly degenerate and as a consequence there are two eigenvectors

$\mathbf{v_1}$ and $\mathbf{v_2}$, one in each diagonal direction. Thus in the two-dimensional case $\mathbf{v} = \alpha_1\mathbf{v_1} + \alpha_2\mathbf{v_2}$, where α_1 and α_2 are real numbers. Depending on the values of α_1 and α_2, the polaron can be driven in different lattice directions. The principal lattice axis direction($i.e\ a_1 = a_2$) is the most stable for the polaron motion since it can propagate in it for a long time without any diversion. In all other directions the polaron faces great difficulties to keep the initial direction. It has been observed that after some time it diverges and moves chaotically. In Fig. 2.5 (b) and (d) we present an illustration of the time evolution of one- and two-dimensional polarons respectively after the kicking with the velocity part of the pinning mode shown in the insets of the Fig. 2.5 (a) and (c). Note that the two polarons have approximately the same mobility.

A characteristic quantity to describe polarons mobility is their effective mass m^*. [54, 55] In the case of an electron in the tight-binding approximation its effective mass is $m_0 = \hbar^2/2\alpha^2 J$ or in units of $J/\alpha^2\omega^2$, $m_0 = \gamma^2/2$ (dimensionless electron mass). In our case, considering the initial kinetic energy of the polaron to be equal to the perturbation energy [25] ($i.e\ \frac{1}{2}m^*v^2 = \frac{1}{2}\sum_i(\lambda\mathbf{v}_i)^2$) we obtain the following expression for the polaron effective mass:

$$\frac{m^*}{m_0} = \frac{(\lambda/v)^2}{\gamma^2/2} \tag{2.20}$$

where v is the dimensionless polaron velocity (in units of $\alpha\omega_0$), and $\mathbf{v}$ is normalized.

Extensive numerical simulations in one and two dimensions imply that the polarons become lighter as nonlinearity increases. The dependence of polaron effective mass on the nonlinear parameter b is presented in Fig. 2.6 (a) and (b) for 1D and 2D respectively. In both cases the values of the system parameters are chosen so that the formation of medium or large polarons to be possible. Thus in 1D for $k = 1.45$ polaron motion is possible even for $b = 0$. Contrary to this in 2D the presence of lattice anharmonicity is necessary in order to construct moving polarons. For the two-dimensional case presented in Fig. 2.6 (b), the polaron motion for $k = 4$, is possible only for values of b greater than 4 approximately. In two dimensions the polaron mobility is studied only in the principal axis direction. In both cases the perturbation strength is $|\lambda| = 0.05$ and $\gamma = 0.1$.

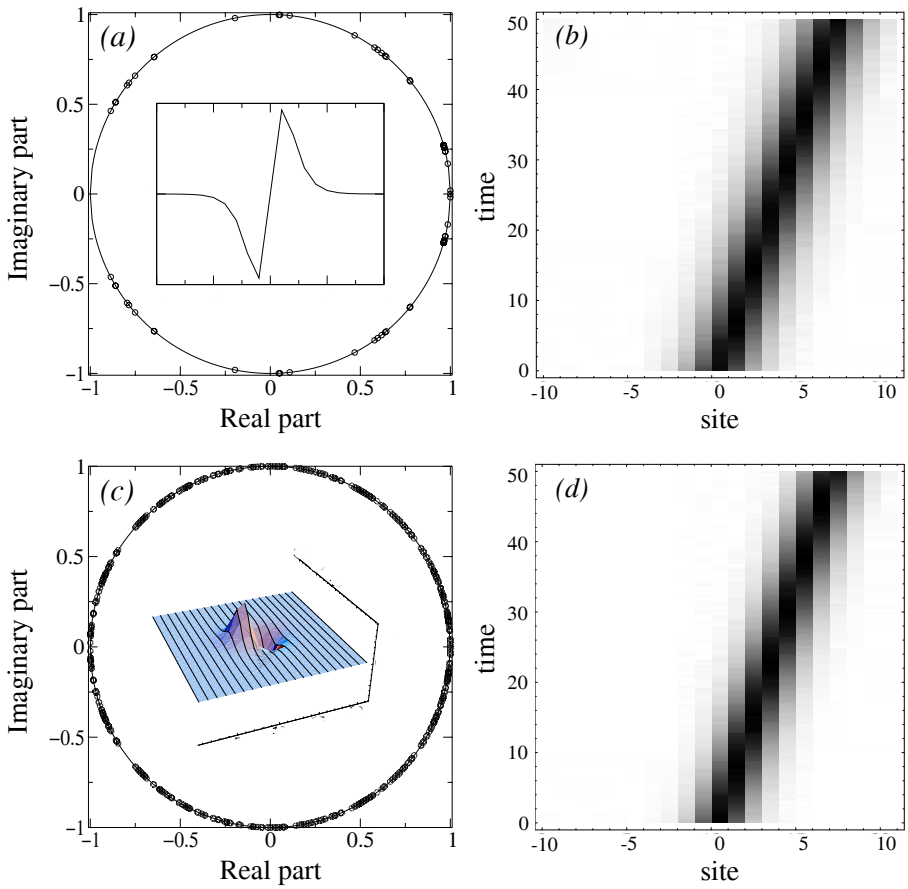

Figure 2.5: Floquet matrix eigenvalues for (a) 1D and (c) 2D. In the insets we show the corresponding normalized velocity parts of the pinning modes which were used to kick the polarons. In (b) and (d) is presented the time-evolution of the one- and two-dimensional mobile polaron respectively after the kicking. The darker sites correspond to higher values of probability $|C_i|^2$ and $|C_{i,0}|^2$ in 1D and 2D respectively. The values of the parameters are $k = 1.45$, $b = 0.1$ in 1D and $k = 4$ and $b = 8$ in 2D while in both cases $\gamma = 0.1$ and $|\lambda| = 0.05$.

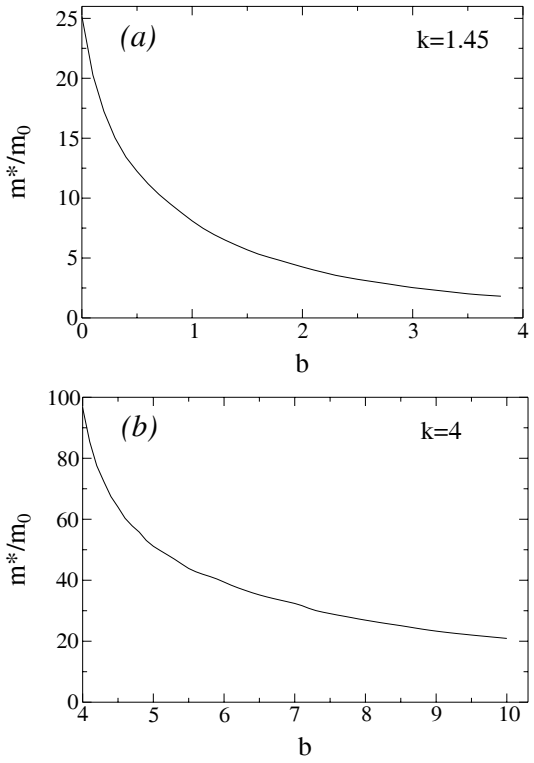

Figure 2.6: The ratio of polaron effective mass m^* to the electron effective mass m_0 as a function of the nonlinear parameter b in (a) 1D and (b) 2D. For the two dimensional case the effective mass is obtained through numerical simulations only for the principal lattice axis directions. In 1D $k = 1.45$ while in 2D $k = 4$. In both case the perturbation parameter is $|\lambda| = 0.05$ and $\gamma = 0.1$.

Although we present mobility results for one and two dimensions, the polaron effective mass is expected to behave in three dimensions similarly as in 2D, since the large polaron formation is also possible as it is described in Sec. III. Thus the reduction of the polaron effective mass due to the hard lattice nonlinearity is expected to be general, not only in 1D and 2D but also in 3D.

2.8 Conclusions

We presented a study of the effects of the on-site lattice nonlinearity in the well-known semiclassical Holstein model in 1D, 2D and 3D. Numerical calculations of the ground state in the adiabatic limit have shown that while in 1D the polaron is always the ground state of the system, in higher dimensions

there are two critical values k_{c_1} and k_{c_2} for the electron phonon coupling that are dependent on the nonlinear parameter b ($i.e\ k_{c_1} \equiv k_{c_1}(b)$ and $k_{c_2} \equiv k_{c_2}(b)$) and determine three different parameter region: *(i)* for $k > k_{c_2}$ the polaron is the ground state the system, *(ii)* for $k < k_{c_1}$ the ground state is delocalized while *(iii)* for $k_{c_1} < k < k_{c_2}$ the polaron is metastable. Note that both of these critical values are increasing functions of b. In 2D k_{c_2} approaches almost asymptotically a specific value of coupling $k_s \simeq 3.4$. For $k > k_s$ the ground state is always the polaron independently of b. The main result is that there is a smooth transition from small to large polarons not only in 1D but also in higher dimensions. In 2D and 3D this transition occurs close to the line $k_{c_2}(b)$ for increasing values of b.

Applying Floquet analysis we have shown that the polaron solutions are linear stable. Normal mode analysis in the non-adiabatic limit shows the existence of a low frequency pinning mode in all dimensions. In absence of nonlinearity it has been shown that this occurs only in the one dimensional case. Furthermore the increase of the nonlinear parameter leads to a significant softening of the pinning mode indicating interesting polaron mobility properties. Perturbating the stationary solution in the direction of the velocity part of the pinning mode, we numerically construct moving polarons in one and two dimensions. Due to the lattice discreteness the construction of moving polarons requires that the perturbation energy must be greater than the corresponding Peierls-Nabarro barrier. In both one and two dimensional cases the polaron motion is possible only in the region of the medium or large polaron size. Thus, while in one dimension the polaron motion is possible even for $b = 0$, in two dimensions the presence of lattice nonlinearity is necessary in order to obtain moving polarons. Numerical simulations in one and two dimensions show a remarkable reduction of the polaron effective mass by increasing the lattice anharmonicity. This phenomenon is closely related to the fact that the on-site anharmonicity is *hard*. In the opposite limit of *soft* nonlinearity (e.g for $b < 0$) the increase of electron-phonon interaction due to the higher flexibility of the oscillators leads to more polaron localization. As a result the polaron effective mass increases or equivalently the polarons become less mobile. Based on the results of the present work it would be interesting to investigate the effects of lattice anharmonicity in the adiabatic Holstein-Hubbard model [56, 57] and its role in the formation and mobility

of the bipolarons [58].

CHAPTER 3

POLARON ASSISTED ELECTRON TRANSFER IN PROTEIN $\beta-$SHEET MODELS

In this chapter we consider electron transfer along $\beta-$sheet forms of proteins. The secondary structure of the proteins $\beta-$sheet is modeled by a two-dimensional oscillator network the constituents of which represent peptide units. Covalent and hydrogen bonds between the peptide units are presented by point-point interaction-potentials. Intra-peptide vibrational degrees of freedom are taken into account by harmonic oscillators while the electronic motion is described within the frame work of a tight-binding system. We construct polarons as stationary localized solution states utilizing a nonlinear map approach. The polaron state represents a self-trapped electron in companion with its intrapeptide deformation field and the static deformation of the protein scaffolding. Furthermore, in the dynamical study we focus interest on the initiation of polaron motion utilizing its pinning modes. We show that both the covalent and the hydrogen channel provide a path for coherent electron transfer proteins in $\beta-$sheet. It is demonstrated that the interplay of the vibrations of the protein scaffolding and the electron dynamics assists long-lived coherently traveling localized excitation patterns along the lattice of peptide units.

3.1 Introduction

Since the work of Davydov in the 1970's the relevance of solitons and/or polarons for the energy and particle transport in biomolecules has been recognized and has remained of great interest (see e.g. [21, 59–61]). Most of these studies of transport properties in biomacromolecules were based on one-dimensional nonlinear lattice models, and only recent two- and three-dimensional extensions with respect to solitonic transport of vibrational energy can be found e.g. in [62–64]. The theory of soliton-like electron transfer (ET) mechanism in one-dimensional chain models of proteins is described in [21, 59–61]. Recently, it was proposed that supersonic acoustic solitons can capture and transfer self-trapping modes in anharmonic one-dimensional lattices [65]. Regarding the enforcing role played by soliton motion in the functional processes in biomolecules, we note that in a recent work it has been proposed that the folding and conformation process of proteins may be mediated by solitons traveling along the polypeptide chains, while interacting with a field corresponding to the conformation angles of the protein [66]. Furthermore, in a nonlinear dynamics approach to DNA dynamics it has been suggested that solitons propagating along the DNA molecule may play an important role in the denaturation and transcription process [67–69].

In this chapter we study the transfer of an electron along the $\beta-$sheet secondary structure of proteins based on the concept of breathers and polarons. The secondary protein structure is modeled by a two-dimensional network of coupled oscillators, each element of it representing a peptide group. The peptide units are connected via point-point pair-potentials modeling the covalent and hydrogen bond interactions, respectively. The electronic system is described by a tight-binding lattice. It is assumed that each peptide unit possesses one internal (intramolecular) vibrational degree of freedom represented e.g. by the $C = O$ stretching mode. As will be shown, mutual couplings between both, the electron amplitude and the intramolecular and intermolecular vibrations, respectively, may lead to polaron formation.

The first part of the chapter is devoted to the study of the stationary problem. We construct localized solutions of the combined electron-vibration system. In order to accomplish this we first derive a generalized discrete non-

linear Schrödinger (DNLS) equation for the electronic amplitude and exploit a nonlinear map approach to construct standing electron-breather solutions. Having obtained the stationary electronic breather pattern, the bond deformations attributed to the polaronic ground state of the complete system can be deduced. Hereafter, we perform a normal mode analysis for the polarons to identify their pinning modes. The latter are then excited with a proper perturbation to initiate motion. We demonstrate that the formation of soliton-like bond vibrations in coexistence with a moving electron breather provide long-lived coherent ET. Finally, in Sec. 3.6 we give a summary of our results.

3.2 The protein $\beta-$sheet model

We consider the transfer of an electron along combined polypeptide chains encountered in secondary structure forms of peptides. The most common secondary structures are helices consisting of folded peptide chains and $\beta-$sheets formed by combined $\beta-$strands. In the latter case, the protein backbone is as extended as possible yielding a $\beta-$strand and $\beta-$sheets are formed when two or more $\beta-$strands are located next to each other allowing for hydrogen bondings between the amide (NH) and carbonyl (CO) groups in the protein backbones [70]-[71]. Refs. [72, 73] are devoted to the design of peptides adopting a $\beta-$sheet structure as well as the creation of native-like globular *de novo* proteins. Experimentally, solutions of identical synthetic *de novo* peptide molecules are used, which self-assemble into long $\beta-$sheet tape structures due to intermolecular hydrogen bonds [74, 75]. The secondary structure is determined by regular arrangements of the the peptide units as well as the hydrogen bonds, i.e. all peptide units are aligned and connected in the same way.

Within our two-dimensional model of an aggregate of combined $\beta-$strands the peptide groups are treated as single mass entities, the equilibrium positions of which are assigned to the sites of a two-dimensional (non-square) lattice labeled by a pair of indices (n, μ). The index n runs in horizontal direction (the x direction) along the sites (peptide groups) of a particular strand specified by μ which enumerates the strands vertically (in the y direction). The bond interactions between the peptide groups hold the $\beta-$sheet in

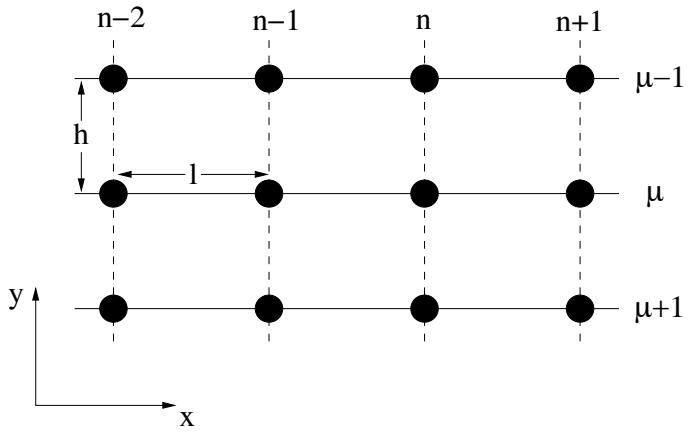

Figure 3.1: The two-dimensional structure of the $\beta-$sheet protein. The bullets representing the peptide units are horizontally (vertically) linked by covalent (hydrogen) bonds as sketched by full (dashed) lines.

its stable secondary structure. Nearest-neighbor units on a strand located at $(n\mu)$ and $(n \pm 1\mu)$ are covalently linked. Peptide groups of different strands oppositely situated at $(n\mu)$ and $(n\mu \pm 1)$ are connected through hydrogen bonds. The covalent (hydrogen) bonds are highly directional parallel to the $x-$axis ($y-$axis) so that we take only the displacements of the peptide groups in the x-y-direction into account and discard any motion in the z-direction. The two-dimensional peptide backbone of a $\beta-$sheet is sketched in Fig. 3.1

Since the strong covalent bonds (bond energies on the order of $50 \sim 250$ kcal/mole) are rather rigid compared to the comparatively weak and flexible H-bonds (bond energies $1 \sim 7$ kcal/mole) [71], it is reasonable to model the (small) distortions of the covalent bonds in a harmonic fashion. The vibrational dynamics of the elastic hydrogen bonds is treated anharmonically [76] by using Morse potentials. The Hamiltonian of the intermolecular interactions is given by

$$\begin{aligned} H_{inter} &= \frac{1}{2m}\sum_n\sum_\mu p_{n\mu}^2 + \sum_n\sum_\mu U_{cov}(r_{n\mu}) + U_{hyd}(q_{n\mu}) \\ &= \frac{1}{2m}\sum_n\sum_\mu p_{n\mu}^2 + \frac{1}{2}\alpha\sum_n\sum_\mu r_{n\mu}^2 \\ &+ \frac{1}{2}D\sum_n\sum_\mu \left(1-\exp[-aq_{n\mu}]\right)^2 , \end{aligned} \tag{3.1}$$

with the momentum vector $p_{n\mu} = (p_{n\mu}^{(x)}, p_{n\mu}^{(y)})$ associated with the displacements $(x_{n\mu}, y_{n\mu})$ of the peptide units from their equilibrium positions $(x_{n\mu}^{(0)}, y_{n\mu}^{(0)})$.

The deviations of the covalent and hydrogen bond lengths from their equilibrium lengths l and h, respectively, are expressed as

$$r_{n\mu} + l = \left[(l + x_{n\mu} - x_{n-1,\mu})^2 + (y_{n\mu} - y_{n-1,\mu})^2\right]^{1/2} , \tag{3.2}$$

$$q_{n\mu} + h = \left[(x_{n\mu} - x_{n\mu-1})^2 + (h + y_{n\mu} - y_{n\mu-1})^2\right]^{1/2} . \tag{3.3}$$

In Eq. (3.1) the parameter α regulates the stiffness of the covalent bonds, m is the mass of a single peptide unit, D determines the break-up energy of the hydrogen bond and a is the range parameter of the Morse potential. The point-point intermolecular interaction potentials are normalized to $U_{cov}(0) = U_{hyd}(0) = 0$ and $U'_{cov}(0) = U'_{hyd}(0) = 0$. Although the dynamics of the modulation of the covalent bonds evolves in harmonic potentials the corresponding dynamical equations are nonetheless nonlinear due to the relation in Eq.(3.2). The assumption of treating the lattice vibrations classically is tantamount to invoking a relatively strong coupling between the electron and the lattice vibrations.

With regard to ET the electronic part of the Hamiltonian is given by

$$\begin{aligned} H_e &= \sum_n \sum_\mu \epsilon_{n\mu} \, |c_{n\mu}|^2 - \sum_n \sum_\mu W(q_{n\mu}) \, \left[c^*_{n\mu} \, c_{n,\mu-1} + c_{n\mu} \, c^*_{n,\mu-1}\right] \\ &- \sum_n \sum_\mu V(r_{n\mu}) \, \left[c^*_{n\mu} \, c_{n-1,\mu} + c_{n\mu} \, c^*_{n-1,\mu}\right] , \end{aligned} \tag{3.4}$$

where $c_{n\mu}$ represents the probability amplitude of the electron to occupy the molecular site n on the strand of index μ and $\epsilon_{n\mu}$ is the on-site energy. The parameter $W(q_{n\mu})$ determines the inter-chain transfer matrix element providing vertical ET between hydrogen-bonded peptide units. The parameter $V(r_{n\mu})$ is the intra-chain transfer matrix element enabling horizontal ET from one peptide unit to the neighboring ones on a $\beta-$strand of index μ.

The local part of the vibrational Hamiltonian models an intramolecular (intrapeptide) vibrational degree of freedom, constituted e.g. by the amide-I vibration of each peptide unit. The dynamics of the intramolecular vibrations is simulated by a set of classical harmonic oscillators situated at sites $(n\mu)$

$$H_{intra} = \sum_{n\mu} \frac{1}{2M} P^2_{n\mu} + \frac{M\omega_0^2}{2} \sum_n Q^2_{n\mu} , \tag{3.5}$$

with $P_{n\mu}$ and $Q_{n\mu}$ being the momentum and coordinate, respectively corresponding to the displacement of an oscillator from its equilibrium position. M is the reduced mass and ω_0 the frequency.

The diagonal coupling between the electronic degree of freedom and the harmonic oscillators contained in the interaction Hamiltonian

$$H_{e-intra} = \kappa \sum_{n\mu} Q_{n\mu} |c_{n\mu}|^2 \,, \tag{3.6}$$

takes vibrational modulations of the local electronic on-site energy $\epsilon_{n\mu} = \epsilon_0 + \kappa\, Q_{n\mu}$ into account and k is the electron-vibration coupling parameter.

The transfer matrix elements, the values of which are determined by an overlap integral, are assumed to depend exponentially on the distance between the peptide units, which amounts to

$$V(r_{n\mu}) = V_0 \, \exp[-b r_{n\mu}] \,, \tag{3.7}$$

$$W(q_{n\mu}) = W_0 \, \exp[-d q_{n\mu}] \,, \tag{3.8}$$

with the coupling parameters b and d. It is through Eqs. (3.7) and (3.8) that the couplings between the electronic and bond vibrational degrees of freedom (d.o.f.) are introduced.

Finally, the interaction between the intra- and intermolecular vibrations is accounted for by

$$H_{intra-inter} = \sum_n \sum_\mu Q_{n\mu} \left[\beta_l \, (r_{n+1,\mu} + r_{n\mu}) \, + \, \beta_t \, (q_{n,\mu+1} + q_{n\mu}) \right] , \tag{3.9}$$

which couples each local intramolecular vibrational coordinate $Q_{n\mu}$ with the bond coordinates $r_{n\mu}$ and $q_{n\mu}$, respectively. The coupling constants are denoted by β_t and β_l.

Altogether the total Hamiltonian of our model includes exchange between electronic, intramolecular as well as intermolecular vibrational energy, respectively.

We scale the time according to $\tilde{t} = \omega_0 \, t$ and introduce dimensionless quantities

$$\tilde{W} = \frac{W_0}{V_0}, \;\; \tilde{D} = \frac{D}{V_0}, \;\; \tilde{Q}_{n\mu} = \sqrt{\frac{M\omega_0^2}{V_0}}\, Q_{n\mu}, \;\; \tilde{P}_{n\mu} = \sqrt{\frac{M\omega_0^2}{V_0}}\, P_{n\mu},$$

$$\tilde{x}_{n\mu} = \sqrt{\frac{M\omega_0^2}{\lambda V_0}}\, x_{n\mu}, \;\; (x_{n\mu} \longleftrightarrow y_{n\mu})$$

$$\tilde{p}^{(x)}_{n\mu} = \sqrt{\frac{\lambda}{M V_0}}\, p^{(x)}_{n\mu}, \;\; (p^{(x)}_{n\mu} \longleftrightarrow p^{(y)}_{n\mu})$$

$$\begin{aligned}
\tilde{a} &= \sqrt{\frac{V_0\lambda}{M\omega_0^2}}\,a, \quad (a \longleftrightarrow b,d) \\
\tilde{\beta}_{h,l} &= \frac{\sqrt{\lambda}}{\omega_0^2 M}\,\beta_{h,l}, \quad \tilde{\kappa} = \frac{1}{\sqrt{V_0 M\omega_0^2}}\,\kappa\,,
\end{aligned} \tag{3.10}$$

with the mass ratio $\lambda = M/m$. Subsequently, to simplify the notation the tildes are dropped. The corresponding scaled coupled equations of motion then read

$$\begin{aligned}
i\,\gamma\,\dot{c}_{n\mu} &= \kappa\,Q_{n\mu}c_{n\mu} - W\exp(-dq_{n\mu})\,c_{n\mu-1} - W\exp(-dq_{n,\mu+1})\,c_{n+1,\mu} \\
&- \left(\exp(-br_{n\mu})\,c_{n-1,\mu} + \exp(-br_{n+1,\mu})\,c_{n+1,\mu}\right)\,, \qquad (3.11)\\
\dot{P}_{n\mu} &= -Q_{n\mu} - \kappa\,|c_{n\mu}|^2 - \beta_l\,(r_{n+1,\mu} + r_{n\mu}) - \beta_t\,(q_{n,\mu+1} + q_{n\mu})\,, \qquad (3.12)\\
\dot{Q}_{n\mu} &= P_{n\mu}\,, \qquad (3.13)\\
\dot{p}^{(x)}_{n\mu} &= \left\{ -\alpha\,r_{n\mu} - \beta_l\,Q_{n\mu} - b\,\left[c^*_{n\mu}\,c_{n-1,\mu} + c_{n\mu}\,c^*_{n-1,\mu}\right]\right\}\,\frac{\partial r_{n\mu}}{\partial x_{n\mu}} \\
&- \left\{ \alpha\,r_{n+1,\mu} + \beta_l\,Q_{n\mu} + b\,\left[c^*_{n\mu}\,c_{n+1,\mu} + c_{n\mu}\,c^*_{n+1,\mu}\right]\right\}\,\frac{\partial r_{n+1,\mu}}{\partial x_{n\mu}} \\
&- \left\{ \beta_t\,Q_{n\mu} + dW\exp(-dq_{n\mu})\,\left[c^*_{n\mu}\,c_{n\mu-1} + c_{n\mu}\,c^*_{n\mu-1}\right]\right. \\
&+ \left. aD\,(1-\exp(-aq_{n\mu}))\,\exp(-aq_{n\mu})\right\}\,\frac{\partial q_{n\mu}}{\partial x_{n\mu}} \\
&- \left\{ \beta_t\,Q_{n\mu} + dW\exp(-dq_{n,\mu+1})\,\left[c^*_{n,\mu+1}\,c_{n\mu} + c_{n,\mu+1}\,c^*_{n\mu}\right]\right. \\
&+ \left. aD\,(1-\exp(-aq_{n,\mu+1}))\,\exp(-aq_{n,\mu+1})\right\}\,\frac{\partial q_{n,\mu+1}}{\partial x_{n\mu}}\,, \qquad (3.14)\\
\dot{x}_{n\mu} &= p^{(x)}_{n\mu}\,, \qquad (3.15)\\
\dot{p}^{(y)}_{n\mu} &= \left\{ -\alpha\,r_{n\mu} - \beta_l\,Q_{n\mu} - b\,\left[c^*_{n\mu}\,c_{n-1,\mu} + c_{n\mu}\,c^*_{n-1,\mu}\right]\right\}\,\frac{\partial r_{n\mu}}{\partial y_{n\mu}} \\
&- \left\{ \alpha\,r_{n+1,\mu} + \beta_l\,Q_{n\mu} + b\,\left[c^*_{n\mu}\,c_{n+1,\mu} + c_{n\mu}\,c^*_{n+1,\mu}\right]\right\}\,\frac{\partial r_{n+1,\mu}}{\partial y_{n\mu}} \\
&- \left\{ \beta_t\,Q_{n\mu} + dW\exp(-dq_{n\mu})\,\left[c^*_{n\mu}\,c_{n\mu-1} + c_{n\mu}\,c^*_{n\mu-1}\right]\right. \\
&+ \left. aD\,(1-\exp(-aq_{n\mu}))\,\exp(-aq_{n\mu})\right\}\,\frac{\partial q_{n\mu}}{\partial y_{n\mu}} \\
&- \left\{ \beta_t\,Q_{n\mu} + dW\exp(-dq_{n,\mu+1})\,\left[c^*_{n,\mu+1}\,c_{n\mu} + c_{n,\mu+1}\,c^*_{n\mu}\right]\right. \\
&+ \left. aD\,(1-\exp(-aq_{n,\mu+1}))\,\exp(-aq_{n,\mu+1})\right\}\,\frac{\partial q_{n,\mu+1}}{\partial y_{n\mu}}\,, \qquad (3.16)\\
\dot{y}_{n\mu} &= p^{(y)}_{n\mu}\,, \qquad (3.17)
\end{aligned}$$

with

$$\frac{\partial r_{n\mu}}{\partial x_{n\mu}} = \frac{l + x_{n\mu} - x_{n-1,\mu}}{l + r_{n\mu}}\,, \qquad \frac{\partial r_{n\mu}}{\partial y_{n\mu}} = \frac{y_{n\mu} - y_{n-1,\mu}}{l + r_{n\mu}} \tag{3.18}$$

$$\frac{\partial q_{n\mu}}{\partial x_{n\mu}} = \frac{x_{n\mu} - x_{n,\mu-1}}{l + q_{n\mu}}\,, \qquad \frac{\partial q_{n\mu}}{\partial y_{n\mu}} = \frac{h + y_{n\mu} - y_{n,\mu-1}}{h + q_{n\mu}}\,. \tag{3.19}$$

The (small) value of the adiabaticity parameter $\gamma = \hbar\,\omega_0/V_0$ expresses the time-scale separation between the fast intramolecular vibrations and the slow intermolecular ET. Through a simple phase transformation $\tilde{c}_n(t) = c_n(t)\,\exp[-i\,\epsilon_0 t]$ we remove the term proportional to $\epsilon_0-$from the electronic equation of motion. Furthermore, we approximate the distance dependence of the horizontal transfer matrix element as $V(r_{n\mu}) = V_0\,\exp[-b r_{n\mu}] \backsimeq V_0(1 - b r_{n\mu})$.

We remark that in the limit of $b = d = \beta_t = \beta_l = 0$ the intermolecular vibrations decouple from the electronic and intramolecular degrees of freedom, respectively and the reduced system can be viewed as a multi-strand extension of the standard (one-dimensional) Holstein model [7, 77] with anisotropic longitudinal and transversal transfer matrix elements V and W. Moreover, the one-dimensional standard Holstein system is covered in the limit $W = 0$.

In this study we use realistic parameter values for proteins [21, 59–61, 70]: $V \simeq 2.5\,eV$, $W \leqslant 1.0\,eV$, $D = (0.04 - 0.3)\,eV$, $m \simeq 100 \times m_{proton}$, $\omega_0 = 3.11 \times 10^{14}\,s^{-1}$, $a \approx b \approx d = (1 - 2)\,\mathring{A}^{-1}$, $\alpha = (0.96 - 4.82)\,eV/\mathring{A}^2$ and $\beta_l \backsimeq \beta_t \simeq 40 \times 10^{-3}\,eV/\mathring{A}^2$. The geometry of the $\beta-$sheet is characterized by typical horizontal distances $h = 2.75\,\mathring{A}$ and vertical distances $l = 3.3\,\mathring{A}$.

3.3 Stationary solutions and polarons

In the following we construct polaron solutions of the coupled system describing the interaction of the electron with the intramolecular vibrations as well as the intermolecular bond oscillators.

To obtain polaron states of the $\beta-$sheet system we consider the corresponding stationary system for which $\dot{P}_{n\mu} = \dot{p}^{(x)}_{n\mu} = \dot{p}^{(y)}_{n\mu} = 0$ must hold and the real time-independent stationary electronic amplitude $\Phi_{n\mu}$ is determined by the relation $c_{n\mu} = \Phi_{n\mu}\,\exp(-i\,Et/\gamma)$. With respect to Eq. (3.12) the stationarity condition leads to the instantaneous distortions

$$Q_{n\mu} = -\kappa|\Phi_{n\mu}|^2 - \beta_l(r_{n+1,\mu} + r_{n\mu}) - \beta_t(q_{n+1\mu} + q_{n,\mu})\,, \tag{3.20}$$

which reduces to

$$Q_{n\mu} \simeq -\kappa|\Phi_{n\mu}|^2 \tag{3.21}$$

for weak coupling parameters β_l and β_t.

Notice that in order to solve the stationary equations of the nonlinear system of Eqs. (3.11)-(3.15) we need to know both, the stationary electronic pattern as well as the stationary deformations of all the bonds. To tackle the complete stationary system we first examine a simpler case by using the approximation of Eq. (3.21) and neglect the low-energetic hydrogen-bond terms of the total Hamiltonian, i.e. we set $D = d = 0$. For vanishing momenta $\dot{p}^{(x)}_{n\mu} = \dot{p}^{(y)}_{n\mu} = 0$

$$\alpha(r_{n\mu}\frac{\partial r_{n\mu}}{\partial x_{n\mu}} + r_{n+1,\mu}\frac{\partial r_{n+1,\mu}}{\partial x_{n\mu}}) = -2b(\frac{\partial r_{n\mu}}{\partial x_{n\mu}}\Phi_{n\mu}\Phi_{n-1,\mu} + \frac{\partial r_{n+1,\mu}}{\partial x_{n\mu}}\Phi_{n\mu}\Phi_{n+1,\mu}), \tag{3.22}$$

and

$$\alpha(r_{n\mu}\frac{\partial r_{n\mu}}{\partial y_{n\mu}} + r_{n+1,\mu}\frac{\partial r_{n+1,\mu}}{\partial y_{n\mu}}) = -2b(\frac{\partial r_{n\mu}}{\partial y_{n\mu}}\Phi_{n\mu}\Phi_{n-1,\mu} + \frac{\partial r_{n+1,\mu}}{\partial y_{n\mu}}\Phi_{n\mu}\Phi_{n+1,\mu}), \tag{3.23}$$

must hold. Both Eqs. (3.22) and (3.23) are satisfied if the distortions of the covalent bonds satisfy the condition

$$r_{n\mu} = -\frac{2b}{\alpha}\Phi_{n\mu}\Phi_{n-1,\mu}\,. \tag{3.24}$$

Hence, combining Eqs. (3.21), (3.24) and the stationary equation for the electronic amplitude $\Phi_{n\mu}$ we end up with the following modified DNLS equation:

$$\begin{aligned} E\Phi_{n\mu} = &-(1+\frac{2b^2}{a}\Phi_{n\mu}\Phi_{n-1,\mu})\Phi_{n-1,\mu} - (1+\frac{2b^2}{a}\Phi_{n\mu}\Phi_{n+1,\mu})\Phi_{n+1,\mu} \\ &-W_0(\Phi_{n,\mu-1}+\Phi_{n,\mu+1}) - \kappa^2|\Phi_{n\mu}|^2\Phi_{n\mu} \end{aligned} \tag{3.25}$$

The above equation is the exact DNLS for a two-dimensional (standard) polaron system. We can find the (electronic) ground state of the Eq. (3.25) by using the numerical method outlined in Refs. [12]. To this end one exploits that polarons (localized electronic states in companion with vibrational displacements localized in the same lattice region) are obtained as the attractors of the map

$$\{\Phi\} \rightarrow \{\bar{\Phi}\} = H\{\Phi\}/\|H\{\Phi\}\| \tag{3.26}$$

with

$$\{\Phi\} = \begin{pmatrix} \Phi_{1\mu=1}, \Phi_{2\mu=1}, ..., \Phi_{N\mu=1} \\ \Phi_{1\mu=2}, \Phi_{2\mu=2}, ..., \Phi_{N\mu=2} \\ . \\ . \\ . \\ \Phi_{1\mu=M}, \Phi_{2\mu=M}, ..., \Phi_{N\mu=M} \end{pmatrix} , \tag{3.27}$$

where the operator H is determined by the r.h.s. of Eq. (3.26) and the norm of the state $H\{\Phi\}$ is defined as $\|H\{\Phi\}\| = \sqrt{\sum_{n\mu} (H\{\Phi\})^2}$ [12]. M determines the number of strands contained in the two-dimensional $\beta-$sheet configuration.

Note that in the limit of $b^2/a \to 0$ we obtain the expected DNLS equation for an anisotropic two-dimensional system. The ground state in the case of $d \neq 0$ and $D \neq 0$ is obtained by using the ground state of the (reduced) Eq. (3.25) as the initial condition in the complete system of equations of motion and invoking the relaxation concept. The latter is based on the reasonable assumption that the instantaneous distortions given by Eq. (3.21) are in close proximity to the genuine ground state solution in configuration space. To reach the real (genuine) ground state we add a small damping term to Eqs.(3.12),(3.14) and (3.16), respectively, and integrate numerically the complete $\beta-$sheet system of Eqs. (3.11)-(3.15) using the following initial conditions:

$$\{ \Phi_{n\mu}, 0, Q^{(0)}_{n\mu}, 0, x^{(0)}_{n\mu}, 0, y^{(0)}_{n\mu}, 0 \} , \tag{3.28}$$

where $Q^{(0)}_{n\mu}$ and $\Phi_{n\mu}$ are determined by Eq. (3.21) and (3.26), respectively. To initialize $x_{n\mu}$ and $y_{n\mu}$ we choose the elongations $r_{n,\mu}$ to be directed exclusively parallel to the x-axis (i.e $r_{n,\mu} = (x_{n,\mu} - x_{n-1,\mu})$). Therefore one gets the initial values

$$x^{(0)}_{n\mu} - x^{(0)}_{n-1,\mu} = -\frac{2b}{\alpha} \Phi_{n\mu} \Phi_{n-1,\mu}$$

and

$$y^{(0)}_{n\mu} - y^{(0)}_{n-1,\mu} = 0 .$$

After short integration times the system relaxes to the ground state solution, i.e. the real stationary solution of the full nonlinear system.

In Fig. 3.2 we display for the simplest $\beta-$sheet configuration, namely a two-strand ladder system, the localized patterns associated with the pola-

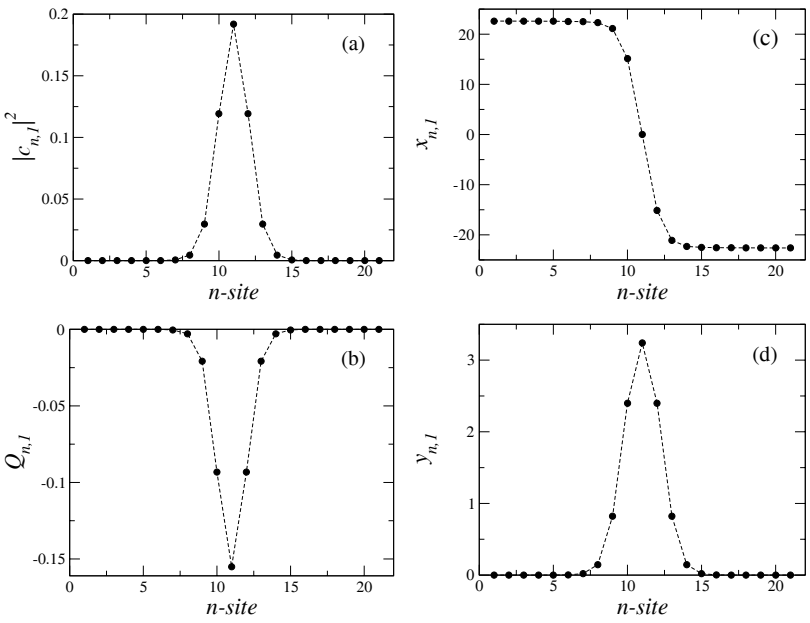

Figure 3.2: The two-strand ladder system. Polaron wave functions for $W = 0.4$, $D = 0.06$, $a = 0.1$, $b = d = 0.05$, $\kappa = 1.0$, $\beta_l = \beta_t = 0.001$, $\alpha = 0.001$ and $\gamma = 0.1$. Due to symmetry only the polaron components on the first strand are shown. (a) The electronic occupation probability $|c_{n,1}|^2$. (b) The displacements of the intramolecular coordinate $Q_{n,1}$. (c) The horizontal distortion $x_{n,1}$ of the peptide groups from their equilibrium positions. (d) The vertical distortion $y_{n,1}$ of the peptide groups from their equilibrium positions.

ronic components of the electronic, intramolecular, covalent-bond and hydrogen-bond subsystem, respectively. According to the symmetry $\Phi_{n1} = \Phi_{n2}$, $Q_{n1} = Q_{n2}$ and $x_{n1} = x_{n2}$ both strands exhibit equal amplitude patterns except for $y_{n1} = -y_{n2}$. Therefore the excitation (polaron) energy is equally shared between the two strands. Regarding the excitation pattern on an individual strand the electron is exponentially localized at the central site (see Fig. 3.2 (a)). The associated pattern of the distortions of the intramolecular oscillators is exponentially localized, too. The pattern of displacements of the peptide groups in horizontal direction $x_{n\mu}$ is characterized by a kink-like shape. Accordingly the covalent bonds to the right (left) of the central site get the more stretched (compressed) the more they are apart from the central site. In vertical direction the localized amplitudes $y_{n\mu}$ have opposite signs, i.e. $y_{n,1} \geq 0$ and $y_{n,2} \leq 0$. Hence the H-bonds get compressed. The peptide

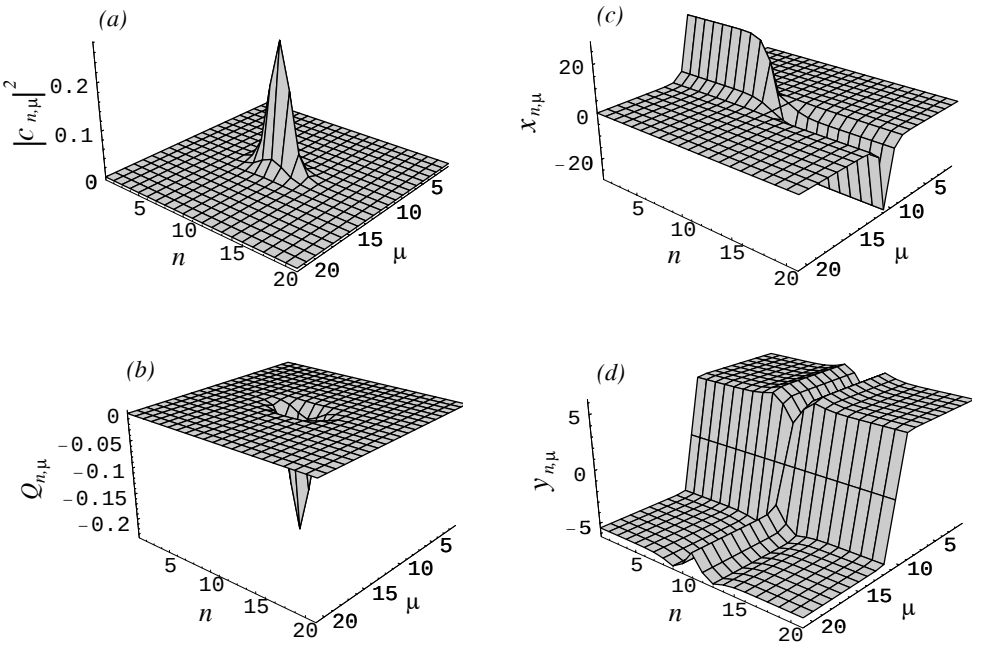

Figure 3.3: The polaron state on an extended $\beta-$sheet aggregate constituted for proposes of better visualization of 21 coupled strands Parameters: $W = 0.4$, $D = 0.06$, $a = 0.1$, $b = d = 0.04$, $\kappa = 1.0$, $\beta_l = \beta_t = 0.001$, $\alpha = 0.001$ and $\gamma = 0.1$. (a) The electronic amplitude $c_{n\mu}$. (b) Displacements of the intramolecular coordinates $Q_{n\mu}$. (c) The horizontal distortions $x_{n\mu}$ of the peptide groups. (d) The vertical distortions $y_{n\mu}$ of the peptide groups.

group at the central site has the largest amplitude of displacement from its equilibrium position and with growing distance from the central site the amplitudes of the vertical distortions decay exponentially. For the two peptide groups oppositely situated at the central sites the degree of compression is maximal and is rapidly diminishing with further horizontal distance from these sites.

Remarkably the distortions of the peptide groups in the x-direction, i.e. along the alignment of the rather rigid covalent bonds, are more pronounced than in the y-direction along which the soft H-bonds are oriented. The bond deformations are the stronger the larger the coupling parameter κ which is connected with a stronger electron localization.

We considered also the polaron states of extended $\beta-$sheet aggregates consisting of 21 coupled strands. The corresponding stationary excitation

patterns are depicted in Fig. 3.3. The exponentially localized electronic wave function is more horizontally extended than in vertical direction. This vertical confinement of the electron to only a few strands is due to the relatively small value of the corresponding transfer matrix element $W = 0.4$ preventing considerable vertical spreading of the electron and thus suppressing also the activation of electron motion along the hydrogen channel. Therefore we expect the electron to be more mobile in the vertical direction along the covalent channel (see discussion further below).

3.4 Polaron normal modes

In this section we investigate the linear stability of the polarons. Furthermore we focus interest on the existence of localized internal modes among the polaron normal modes. Such localized internal modes play a fundamental role for the formation, stability and mobility of localized states such as breathers and polarons [25, 78–82]. We impose small perturbations on the stationary states in the following way

$$Q_{n\mu}(t) = Q^{(0)}_{n\mu}(t) + \delta Q_{n\mu}(t)\,, \tag{3.29}$$

$$x_{n\mu}(t) = x^{(0)}_{n\mu}(t) + \delta x_{n\mu}(t)\,, \tag{3.30}$$

$$y_{n\mu}(t) = y^{(0)}_{n\mu}(t) + \delta y_{n\mu}(t)\,, \tag{3.31}$$

$$c_{n\mu}(t) = \{\,\Phi_{n\mu} + \delta c_{n\mu}(t)\,\} \exp\left[-i\,\frac{E}{\tau}\,t\right]\,, \tag{3.32}$$

where $\delta Q_{n\mu}$ and $\delta c_{n\mu}$ are small quantities. Substituting Eq. (3.29)-(3.32) into the system Eq. (3.11)-(3.15) and linearizing around ($Q_{n\mu} = Q^{(0)}_{n\mu}$, $x_{n\mu} = x^{(0)}_{n\mu}$, $y_{n\mu} = y^{(0)}_{n\mu}$ and $c_{n\mu} = \Phi_{n\mu}$) gives the linear system of tangent equations which we express with the perturbation vector

$$\Delta = (\delta c_{n\mu}, \delta c^{*}_{n\mu}, \delta Q_{n\mu}, \delta \dot{Q}_{n\mu}, \delta x_{n\mu}, \delta \dot{x}_{n\mu}, \delta y_{n\mu}, \delta \dot{y}_{n\mu}) \tag{3.33}$$

in matrix notation

$$\dot{\Delta} = M\,\Delta\,. \tag{3.34}$$

The periodic entries of the Jacobian matrix
$M = M(\Phi_{n\mu}, \Phi^{*}_{n\mu}, Q^{(0)}_{n\mu}(t), \dot{Q}^{(0)}_{n\mu}(t), x^{(0)}_{n\mu}(t), \dot{x}^{(0)}_{n\mu}(t), y^{(0)}_{n\mu}(t), \dot{y}^{(0)}_{n\mu}(t))$ follow from the evolution of system Eqs. (3.11)-(3.15). To analyze the system of Eq.

(3.34) we proceed in a standard way using Floquet theory. We integrate the equations of motion over one period $T = 2\pi\tau/E$ to get the Floquet map

$$\Delta(T) \;=\; F\,\Delta(0)\,, \tag{3.35}$$

giving the evolution of an initial deviation of the periodic solution after one period T with the Floquet matrix F. Linear stability of a periodic solution is assured if all the eigenvalues $R_n \exp(i\,\Theta_n)$ of F lie on the unit circle. Intensive numerical investigations in a wide parameter range have proved that all the polarons gained from the procedure outlined above are linearly stable.

Additionally, the Floquet analysis provides us with the frequencies of the normal modes via the relation $\omega_\Theta = \omega_e\Theta/(2\pi)$ with Θ expressed in rad. The isolated eigenvalue of the Floquet spectrum attributed to the frequency of a pinning mode is doubly degenerate corresponding to perpendicular directions along the covalent respectively hydrogen bonds.

3.5 Polaron assisted electron transfer

In this section we study the mobility of polarons with the help of a numerical method originally developed for breather solutions [25]. (Actually, the electronic amplitude pattern $c_{n\mu} = \Phi_{n\mu}\,\exp(-iEt)$ can be regarded as a static electron breather solution [78].) According to [25] we initiate the motion of polarons through suitable perturbations of the momentum variables $\left\{\dot{p}^{(x)}_{n\mu}\right\}$ targeted in the horizontal direction of the pinning mode component along the covalent bonds, that is we use for the numerical integration of the system Eqs. (3.11)-(3.15) the initial conditions

$$\left\{\,\Phi_{n\mu}, 0, Q^{(0)}_{n\mu}, 0, x^{(0)}_{n\mu}, 0, y^{(0)}_{n\mu}, 0\,\right\} + k\;\left\{0,0,0,0,0,\xi_{n\mu},0,0\right\}\,, \tag{3.36}$$

with the normalized momentum part ξ of the pinning mode and k is the perturbation strength. Furthermore we imposed periodic boundary conditions. Due to the lattice discreteness the polarons are pinned and have to overcome a certain Peierls-Nabarro-energy barrier in order to become mobile along the discrete lattice [79, 83]. Mobility is achieved for an overcritical perturbation strength k as long as the (stationary) polaron extension is not too small [25, 42].

In Fig. 3.4 we illustrate the initiated motion of the polaron on a two-strand ladder system. The coherently moving electron (Fig. 3.4 (a)) is accompanied

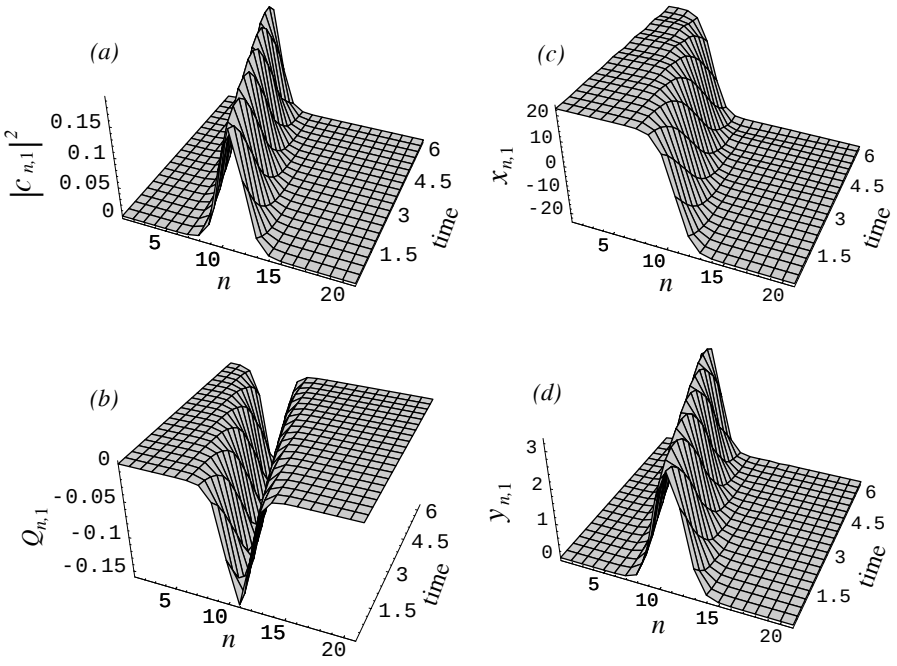

Figure 3.4: Moving polaron state on the two-strand ladder system. Parameters as in Fig. 3.2 and the kicking strength is $k = 0.3$. (a) The soliton-like electronic amplitude $|c_{n,1}|$. (b) Displacements of the intramolecular coordinates $Q_{n,1}$. (c) The horizontal distortions $x_{n,1}$ of the peptide groups. (d) The vertical distortions $y_{n,1}$ of the peptide groups.

by its localized pattern of intramolecular coordinate distortions as well as the deformation field of the horizontal and vertical displacements of the peptide groups, respectively. Note that there are (virtually) no radial losses and the polaron maintains its profile and energy content.

The evolved components of a mobile polaron on an extended two- dimensional $\beta-$sheet after 6000 time units are displayed in Fig. 3.5. The stationary polaron state illustrated in Fig. 3.3 provides the initial configuration which experiences a kick along the longitudinal momentum component of its pinning mode. The polaron has coherently moved over ten lattice sites across the covalent bonds. We remark that motion perpendicular to the covalent bonds, i.e. along a hydrogen path, can be accomplished as well through the excitation of the corresponding vertical part of the pinning mode corresponding to the momentum variables $\left\{\dot{p}^{(y)}_{n\mu}\right\}$. However, the motion along the hydrogen channel proceeds with lower velocity than along the covalent one.

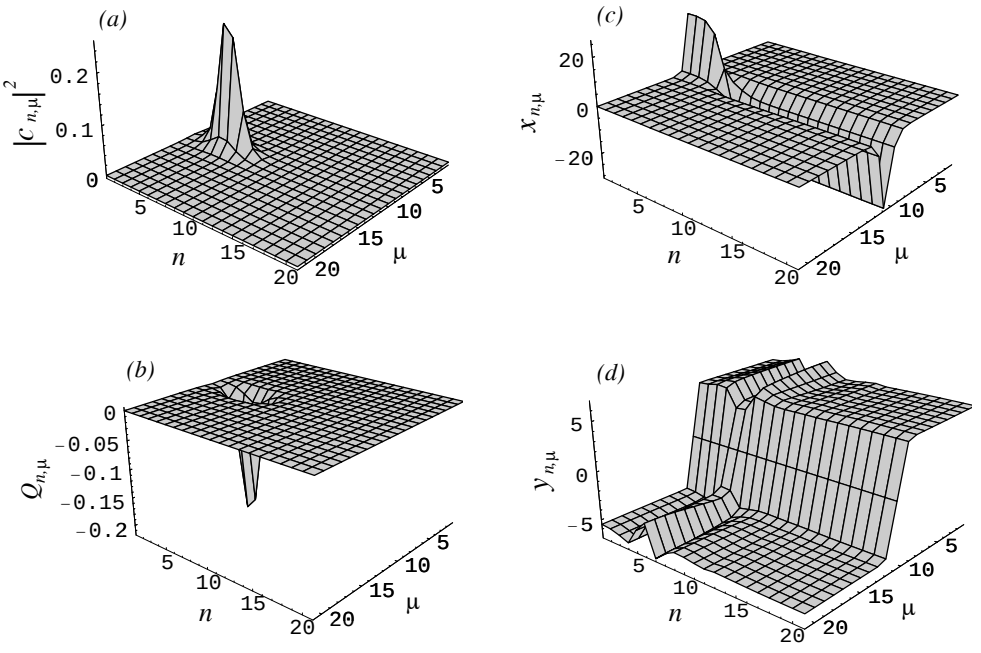

Figure 3.5: Mobile polaron on an extended two-dimensional $\beta-$sheet illustrating the spatio-temporal evolution of an initial polaron state depicted in Fig. 3.3 after 6000 time units. In the initial conditions the momentum component of the pinning mode targeted along the covalent bonds was included with kicking strength $k = 0.3$.

Remarkably, although the polaron's extension is rather small (its electronic component is confined to only five sites) it is nevertheless mobile. The latter feature has to be distinguished from the properties of the polarons of the standard two-dimensional Holstein system for which only small polaron formation is possible which, due to their small size, cannot propagate on the rigid lattice [7]-[77]. The inclusion of on-site lattice anharmonicity in the (rigid lattice) Holstein system makes the formation of medium and large polarons also possible in two and three dimensions [12, 42, 53]. Furthermore, in the presence of nonlinearity a low-frequency pinning mode vital for the activation of polaron mobility exists in all dimensions [12, 42]. Similarly, as demonstrated in this work, when the couplings of the lattice vibrations (nonrigid lattice) to the electron and the intramolecular vibrations are taken into account uniformly propagating polarons can be constructed using a low-frequency pinning mode. This underlines the crucial role played by the bond

vibrations for polaron mobility [12, 42].

3.6 Conclusions

In this chapter we have considered the ET in the context of protein $\beta-$sheet models. The regular arrangement of the protein secondary structure is modeled by a two-dimensional lattice system where each site is attributed to a peptide group allowed to perform planar motions. The hydrogen and covalent bond interactions between the peptide groups are modeled via pair potentials. Each peptide group has an internal vibrational degree of freedom representing e.g. the fast amide-I mode. The motion of the electron over the peptide groups is described by a tight-binding system. The various dynamical degrees of freedom are mutually coupled making the exchange of electronic, intramolecular and intermolecular vibrational energy, respectively, possible.

We have studied the stationary polaron problem with respect to the formation of self-trapped states. For vanishing momenta of the vibrational degrees of freedom we have been able to derive a generalized nonlinear Schrödinger equation for the electronic amplitude. Localized stationary solutions of the latter correspond then to the electronic part of the polaron. Subsequently we have inferred on the vibrational polaron patterns. The static localized electron is connected with a deformation of the protein backbone. In particular in the vicinity of the localized electron the bonds are pronouncedly deformed and in the horizontal direction we observe that to either site on which the maximal electron amplitude resides the covalent bonds are compressed respectively stretched while in vertical direction the length of the H-bonds reduces.

In the parameter range when the polarons are of large (medium) extension we have exploited a perturbation method to initiate polaron motion. To this aim we have properly kicked the momentum component in the direction of the corresponding pinning mode. In this way coherent polaron motion is accomplished providing stable electron transfer in $\beta-$sheets. Comparing the transport across the covalent respectively hydrogen channel we conclude that the former supports faster electron transfer than the latter one.

This work has demonstrated that the coupling between electronic vibrational and elastic degrees of freedom in a $\beta-$sheet model can induce stable localized mobile structure. These coherent polaron structure assist ET since

they effectively stabilize locally the vibrational and elastic degrees of freedom. As a result the electronic motion becomes more coherent and robust. It would be interesting to search experimentally for the role of these polaron in β-sheet configurations.

CHAPTER 4

THE MULTI-QUANTA HOLSTEIN MODEL

In this chapter, we study the many quanta problem of the Holstein model in both adiabatic and nonadiabatic limit. The ground state energy is calculated numerically using the concept of anticontinuous limit as well as the Toyozawa Exponential Approximation (TEA). Analytical expressions of the ground state energy in the adiabatic case are also obtained.

4.1 Introduction

In Chapters 2 and 3, we analyzed the Holstein model for the case of a single electron interacting with the lattice. In general, the same treatment can be applied for any quantum excitation (exciton) interacting with phonons. In the case where these excitations are bosons, the model can be extended to include arbitrary number of excitons. A limiting form of the many quanta Holstein model (MQHM) was successfully applied in explaining the 'anomalous' amide-I ($C = O$ stretching) band in crystalline acetanilide (ACN) [32]. Scott and co-workers [61, 84, 85], following the traditional 'polaron' theory, claimed that this observation can be assigned to a self-trapped state in which $C = O$ vibration energy can be localized to a single ACN molecule due to the interaction with the lattice. In the adiabatic and anticontinuous regime, they have shown that MQHM fits well the experimental observation not only for the fundamental frequency but also for the three higher overtones [86]. In what follows, we present an extension of this work in the non-adiabatic limit for any value of the exciton-phonon coupling.

For the purpose of this chapter, it is more convenient to rewrite the Hamiltonian of the Holstein model as follows:

$$H = H_{ex} + H_{ph} + H_{int}, \tag{4.1}$$

$$H_{ex} = E_0 \sum_i \alpha_i^\dagger \alpha_i - J \sum_{i,n_i} \alpha_i^\dagger \alpha_{n_i}, \tag{4.2}$$

$$H_{ph} = \hbar\omega_0 \sum_i (b_i^\dagger b_i + \frac{1}{2}), \tag{4.3}$$

$$H_{int} = g \sum_i \alpha_i^\dagger \alpha_i (b_i^\dagger + b_i), \tag{4.4}$$

where $\alpha_i^\dagger(\alpha_i)$ and $b_i^\dagger(b_i)$ is the standard bosonic creation (annihilation) operators of excitons and phonons respectively, J is the hopping integral between the site i and its nearest neighbors n_i, while E_0 is the exciton on-site energy and ω_0 is the optical phonon frequency. The strength exciton-phonon on-site interaction is determined by g.

Choosing J as energy unit and defining the position and momentum operators as follows:

$$u_n = \sqrt{\frac{\gamma}{2}}(b_n^\dagger + b_n), \tag{4.5}$$

$$p_n = i\sqrt{\frac{2}{\gamma}}(b_n^\dagger - b_n), \tag{4.6}$$

the Hamiltonian (4.1) can be written in the following reduced form:

$$\begin{aligned} H &= \epsilon_0 \sum_i \alpha_i^\dagger \alpha_i - \sum_{i,i_n} \alpha_i^\dagger \alpha_{n_i} \\ &+ \sum_i (\gamma \frac{p_i^2}{2} + \frac{u_i^2}{2}) + k \sum_i u_i \alpha_i^\dagger \alpha_i, \end{aligned} \tag{4.7}$$

where $\gamma = a^2 = \frac{\hbar\omega_0}{J}$ is the adiabaticity parameter, ϵ_0 and $k = g\sqrt{\frac{2\hbar\omega_0}{J}}$ are the dimensionless exciton and exciton-phonon energy respectively.

In the following sections we will study the MQHM in the non-adiabatic as well as in the adiabatic limit.

4.2 Non-Adiabatic Limit

Due to the invariance of the system under translations, the wave function of a quantum ILM can be written as a Bloch wave:

$$|\Omega(K)\rangle = \frac{1}{\sqrt{\Lambda}} \sum_n e^{-iKn} |\Psi(n)\rangle, \tag{4.8}$$

K is the wave vector, Λ is a normalization factor and $|\Psi(n)\rangle$ is the localized wave function around site n of N quanta interacting with phonons.

In order to calculate variationaly the energy of the system, we use the Toyozawa Exponential Approximation (TEA) [87]

$$|\Psi(p)\rangle = \frac{1}{\sqrt{N!}} \sum_{j_1,\ldots,j_N} C_{j_1-p,\ldots,j_N-p} \alpha_{j_1}^\dagger \alpha_{j_2}^\dagger \ldots \alpha_{j_N}^\dagger e^{i\sum_i v_{i-p} p_i} |\emptyset\rangle, \tag{4.9}$$

where $|\emptyset\rangle$ is the vacuum state for both exciton and phonon field, $C_{j_1,j_2,\ldots,j_N}$ are the probability amplitudes for finding one exciton one site site j_1, one on j_2, ... etc., and v_n describes the lattice deformation. Due to the bosonic

character of the excitons, the indices $j_1, j_2, .., j_N$ are not necessarily different and

$$C_{j_1,j_2,...,j_N} = C_{P\{j_1,j_2,...,j_N\}}, \tag{4.10}$$

where P indicates all the possible permutations of the set $\{j_1, j_2, .., j_N\}$.

Taking into account the relation between the excitons densities and the average atomic displacement, as it is described in the work of Ref. [20] the normalization condition of $\{v_n\}$ in our model with N quanta is:

$$\sum_n v_n = -kN. \tag{4.11}$$

To simplify numerical calculations we use Hartree approximation for the exciton probability amplitudes

$$C_{j_1,j_2,...,j_N} = C_{j_1} C_{j_2} ... C_{j_N}. \tag{4.12}$$

Since the behavior of $(N+1)L$ variational parameters [1] ($\{C_{j_1}, ..., C_{j_N}\}$ and $\{v_n\}$) is expected to decay exponentially in space for localized solutions in the limit of strong exciton-phonon coupling, we assume the following simple exponential functions:

$$\begin{aligned} C_n &= A\lambda^{|n|} \quad A = (\frac{1-\lambda^2}{1+\lambda^2})^{1/2} \\ v_n &= -B\mu^{|n|} \quad B = kN(\frac{1-\mu^2}{1+\mu^2}). \end{aligned} \tag{4.13}$$

The factor kN appearing in the prefactor B of Eq. (4.13) is a constant, and as e result we can neglect it and define an effective exciton-phonon coupling

$$k_N = k\sqrt{N} \tag{4.14}$$

for the N quanta case that will appear in the final form of the variational energy.

Taking into account all the these assumptions, the variational energy for each wave vector K is:

$$E_N(K) \;=\; \langle\Omega(K)|H|\Omega(K)\rangle = \frac{\sum_p e^{iKp}\langle\Psi(j)|H|\Psi(j+p)\rangle}{\sum_p e^{iKp}\langle\Psi(j)|\Psi(j+p)\rangle}, \tag{4.15}$$

[1] L is the total number of lattice sites

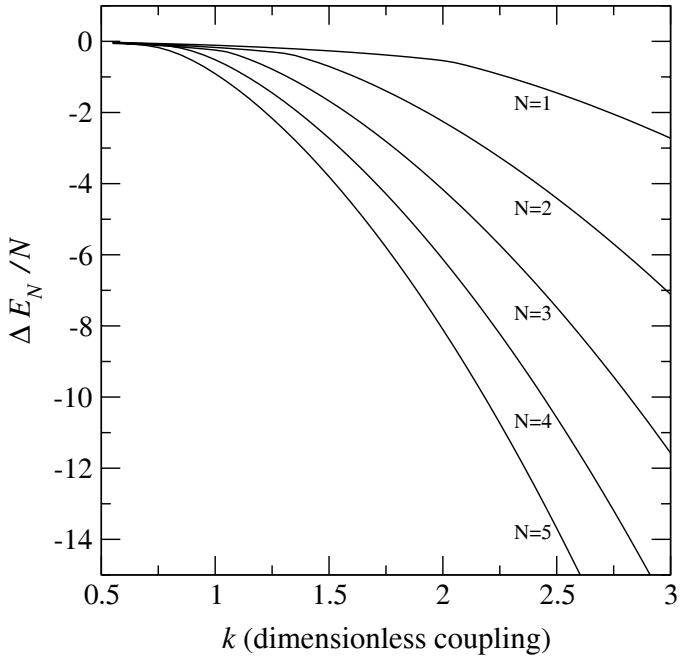

Figure 4.1: Nonadiabatic limit: The binding energy per quantum ($\Delta E_N/N$) is shown as a function of the coupling constant k for different numbers of bound quanta ($N = 1, 2..., 5$).

where the scalar products

$$\langle\Psi(j)|\Psi(j+p)\rangle = e^{-\frac{Nk_N^2}{4a}\sum_i (u_{i+p}-u_i)^2} \sum_i C^*_{i+p} C_i \tag{4.16}$$

$$\begin{aligned}\langle\Psi(j)|H|\Psi(j+p)\rangle = e^{-\frac{Nk_N^2}{4a}\sum_i (u_{i+p}-u_i)^2} \times \\ N\{\textstyle\sum_i \epsilon_0 C^*_{i+p} C_i - \sum_i C^*_{i+p}(C_{i-1}+C_{i+1}) \\ +\frac{k_N^2}{2}\sum_i u_{i+p}u_i \sum_i C^*_{i+p}C_i + k_N^2 \sum_i (u_{i+p}+u_i) C^*_{i+p} C_i\}\end{aligned} \tag{4.17}$$

do not depend on j [20]. The zero point phonon energy is eliminated in the final form of the variational energy. We note that by using the Hartree Eq. (4.12) and the exponential approximations Eq. (4.13) we obtain only two variational parameters, λ and μ, instead of the $(N+1)L$ parameters of the initial Toyozawa ansatz of Eq. (4.9).

4.2.1 Numerical results

Minimizing the variational energy of Eq. (4.15), with respect to λ and μ, using a 1D chain with periodic boundary conditions, we obtain the energy

band of ILMs. We define J_N the effective hoping integral J_N for N excitons as $J_N = B_N/4$, where B_N is the bandwidth, while the binding energy ΔE_N is the difference between the ILM energy and the energy of N extended excitons at the bottom of their bands ($i.e$ for $K = 0$). Since the effective coupling k_N is an increasing function of the number of quanta N and exciton-phonon coupling (see Eq. (4.14)) it is expected that the binding energy will grow as N or k increases. This is confirmed in Fig 4.1, where we present the binding energy per quantum as a function of k for $N = 1, 2, ..., 5$. This gain in the binding energy, due to the increase of N additionally affects the effective hopping integral J_N. In Fig. 4.2 (a) and (b), we show an example of energy bands for one and two localized excitons respectively, neglecting the on-site energy ϵ_0. In this figure, where the exciton-phonon coupling is $k = 1.2$ and the adiabaticity parameter $a = 0.1$, we observe a significant decrease of J_2 compared to J_1. Generally, the bandwidth of the ILM drops almost exponentially when increasing the number of quanta. Moreover, since the effective mass m_N^* is proportional to the inverse of J_N, the localized mode becomes heavier by increasing N. The dependence of J_N and ΔE_N on N is shown in Fig. 4.2 (c) and (d) respectively. In the limit of very large N, the bandwidth of ILM vanishes and the corresponding effective mass goes to infinite.

4.3 Adiabatic Limit

In the adiabatic limit $\gamma \to 0$, there are not lattice fluctuations, the ILM is degenerated to lattice translations and as result its energy band vanishes.

Following procedure similar to that in Chap. 2, we minimize the total energy with respect to $\{u_i\}$ by using the stationary condition

$$C_{j_1,j_2,...,j_N} = \Phi_{j_1,j_2,...,j_N} e^{-i\frac{E}{\gamma}\tau}, \tag{4.18}$$

where the coefficients $\Phi_{j_1,j_2,...,j_N}$ are time-independent and E is the sum of the tight-binding and interaction energy. The distortion of the i_{th} oscillator is given by $\partial(\langle\Psi|H|\Psi\rangle)/\partial u_i = 0$, that leads to:

$$u_i = -k\langle\Psi|\alpha_i^\dagger a_i|\Psi\rangle = -k\rho_i, \tag{4.19}$$

where the state $|\Psi\rangle$ is given by the adiabatic version of Eq. (4.9) (neglecting the lattice contribution) and

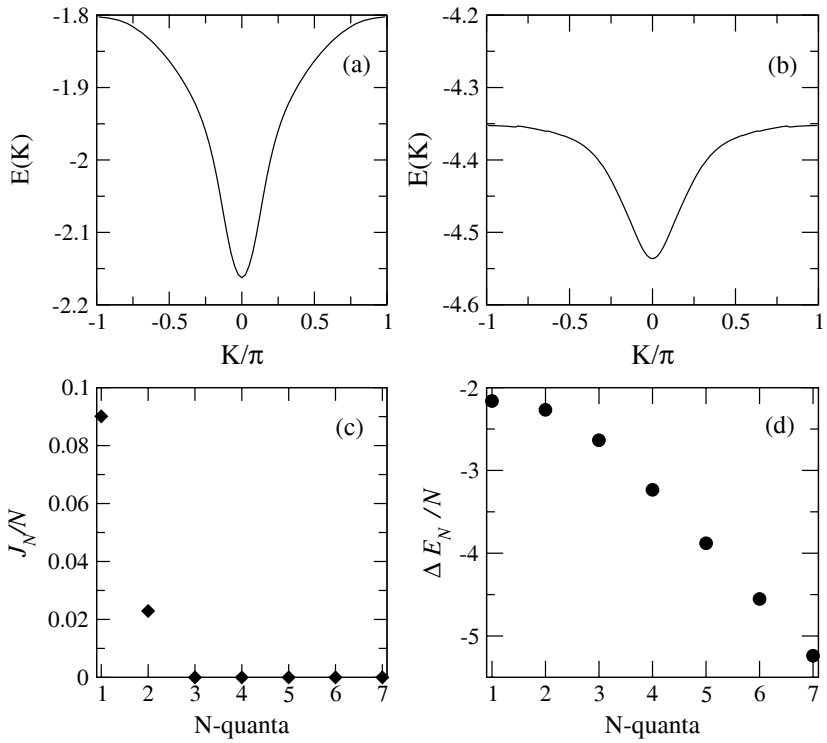

Figure 4.2: Energy band of (a) one quantum ($N = 1$) and (b) two quanta ($N = 2$). (c) Effective hopping integral J_N and (d) binding energy ΔE_N per N as a function of the number of quanta. In all figures $k = 1.2$ and adiabaticity parameter $a = 0.1$

$$\rho_i = N \sum_{i_1,\ldots,i_{N-1}} |\Phi_{i,i_1,\ldots,i_{N-1}}|^2 \,. \tag{4.20}$$

In the derivation of the last equation we have taken into account the normalization condition of the N-quanta wave function. The quantity ρ_i/N gives the probability of finding any quantum at site i. The eigenvalue equation for the N-quanta stationary states is described by the following generalized DNLS equation:

$$E\Phi_{j_1,j_2,\ldots,j_N} = (N\epsilon_0 - \Delta_N - k^2 P_N)\Phi_{j_1,j_2,\ldots,j_N}\,, \tag{4.21}$$

where

$$\Delta_N \Phi_{j_1,\ldots,j_N} = \sum_{n_{j_1},\ldots,n_{j_N}} [\Phi_{n_{j_1},\ldots,j_N} + \ldots + \Phi_{j_1,\ldots,n_{j_N}}] \tag{4.22}$$

and

$$P_N \Phi_{j_1,...,j_N} = [\rho_{j_1} + ... + \rho_{j_N}] \Phi_{j_1,...,j_N} \ . \tag{4.23}$$

In Eq. (4.22), the index n_{j_i} denotes the nearest neighboring sites to site j_i. The Eq. (4.21), including a Hubbard term, has been obtained for $N = 2$ in the study of the Holstein-Hubbard bipolaron problem [20]. As can be seen from Eq. (4.21) the ground state solutions do not depend on the parameter γ. The latter affects the dynamical properties of the system (e.g. the normal modes), since it enters the equations of motion (see for example Eq. (2.5) of Chap. 2).

The total energy of the system, including the lattice energy, is given by

$$E_N = N\epsilon_0 - \sum_{j_1,...,j_N} \Phi^*_{j_1,...,j_N} \Delta_N \Phi_{j_1,...,j_N} - \frac{k^2}{2} \sum_i \rho_i^2 \tag{4.24}$$

4.3.1 Numerical results

The ground state of Eq. (4.21) with periodic boundary conditions is calculated numerically using the same method as in Chap. 2 ([12]). The results show that, as in the one quantum case, the ground state for the N quanta is always localized for any non-vanishing coupling strength forming a many-quanta ILM. These ILMs are gradually more extended as coupling k decreases. In the limit $k \to 0$ and for an infinite lattice we obtain $E_N \to N(\epsilon_0 - 2)$, which is the ground-state energy of N non-interacting fully extended (Bloch) excitons. In Fig. 4.3 we present with solid lines numerical results obtained from Eq. (4.21) for the binding energy $\Delta E_N = E_N - N(\epsilon_0 - 2)$ per quantum as a function of coupling constant for different number of bound quanta, N. It is clearly seen that, as in the nonadiabatic case of the previous section, the absolute value of the binding energy is an increasing function of N, resulting in strong red-shifts of the overtone spectra. Additionally, the wave function of the ground state becomes more localized as N increases. The stability of ILMs in the adiabatic case has been confirmed explicitly for the one-quantum [12] and two-quanta [20] cases. Higher quanta ILMs are not expected to lose their stability since they become more localized.

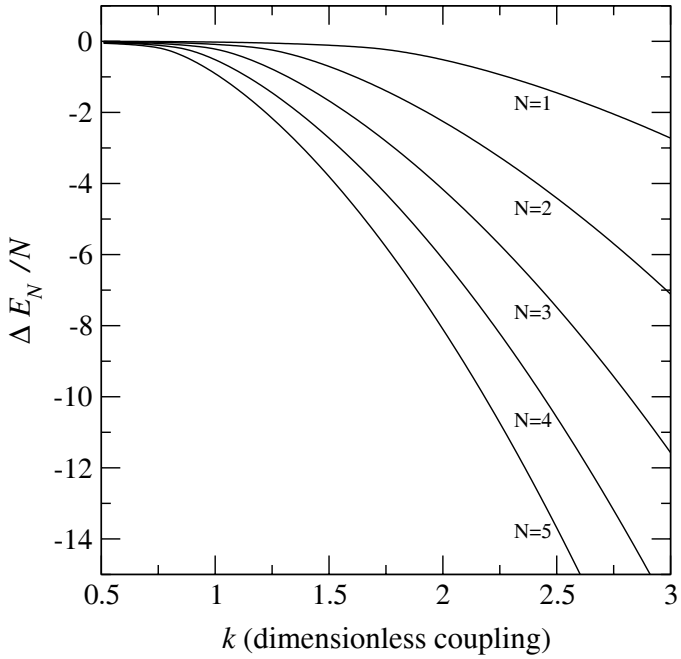

Figure 4.3: Adiabatic limit: The binding energy per quantum ($\Delta E_N/N$) as a function of the coupling constant k for different numbers of bound quanta ($N = 1, 2..., 5$).

4.3.2 Analytical results

In the framework of the Hartree approximation of the previous section the variational energy has the form:

$$E_N(k) = NE_1(k_N), \tag{4.25}$$

where

$$E_1(k_N) = \epsilon_0 - \sum_{i,n_i} C_i^* C_{n_i} - \frac{k_N^2}{2} \sum_i |C_i|^4 \tag{4.26}$$

is the polaron energy for the effective coupling k_N instead of k in 1D, 2D, and 3D. The ground state energy of Eq. (4.15) can be calculated either numerically [42, 12] or analytically [61] by using a combination of variational and perturbation approximation, in the continuous limit [7] as well as in the anti-continuous limit [12]. More precisely, the approximate analytical expression of the mean field energy in the continuous limit (large polarons) [7] is

$$E_1(k_N) = \epsilon_0 - (2 + \frac{k_N^4}{48}) \tag{4.27}$$

This expression is valid only for 1D models since in higher dimension large polarons do not exist (see Chap. 2). In the anticontinuous limit, the ground state energy is given by [61]:

$$E_1(k_N) = \epsilon_0 - \frac{k_N^2}{2} \tag{4.28}$$

in 1D, 2D as well as 3D. In the regime close to the anticontinuous limit an improved expression can also be derived [12]:

$$E_1(k_N) = \epsilon_0 - (\frac{k_N^2}{2} + \frac{2D}{k_N^2} + \frac{4D^2 - 3D}{k_N^6}), \tag{4.29}$$

where $D = 1, 2, 3$ for one-, two-, and three-dimensional systems respectively.

It is worthwhile to point out that according to polaron theory in 2D and 3D there are two critical coupling values k_{c_1} and k_{c_2} that determine three different regions. For $k \geq k_{c_2}$ the polaron is always the ground state of the system, for $k < k_{c_1}$ the ground state is completely delocalized with energy $E_d = -2D$ (in units of J), while in the intermediate region, where $k_{c_1} \leq k < k_{c_2}$ polarons are metastable, *i.e* polaron formation is possible but its energy is higher than the energy of the corresponding delocalized state. In the MQHM the effective exciton-phonon coupling k_N is an increasing function of the number of quanta N (Eq. (4.14)). In the limit of small k, where a single quantum is delocalized, the condition that determines the specific regime depends on N. In this case, and for the sake of clarity, it is necessary to define two critical values of N, N_{c_1} and N_{c_2}, related to the critical couplings k_{c_1} and k_{c_2} respectively. Thus, if $k < k_{c_1}$, the number of quanta N has to be greater than the critical value N_{c_2} in order the effective coupling to be greater than k_{c_2} and to have localized states. This means that if $N < N_{c_1}$ the overtone spectra is a multiple of fundamental energy while for $N > N_{c_2}$ there will appear a red-shift of the overtones in the energy diagram. From experimental point of view this analysis would indicate for the effective dimensionality of the system.

4.4 Conclusions

In this section we have studied the 1D many quanta Holstein model in the adiabatic as well as in the nonadiabatic limit. For the latter case, we used a

combination of Hartree approximation and TEA in order to obtain a variational form of the ILM energy. These approximations simplify significantly the final expression of the variational energy, since the latter depends only on two parameters, instead of (N+1)L of the N-excitons interacting with lattice. Minimizing numerically this energy we obtained the ILM bands . Numerical results suggest that there is a significant gain of the binding energy as the number of quanta N increases and this results to a strong redshift of the energy spectrum. Another interesting result is that the effective hopping integral of ILM decays almost exponentially by increasing N. In the limit of very large N the ILM bandwidth vanishes, $i.e$ the solution is localized on a single site and the corresponding effective mass diverges.

In the adiabatic approximation where there are no lattice fluctuations the ILM energy band vanishes. This enables us to extract a generalized DNLS for the N-quanta problem without using any approximation as in the nonadiabatic case. Using the exact numerical procedure of the anticontinuous limit, we calculated the ground state energy and found a result analogous to that of the nonadiabatic limit. Specificallly the binding energy is found to be an increasing function of the number of quanta and the corresponding ground state becomes more localized as N increases. Once again, in the limit of large N the ILM is localized to a single site rendening this solution completely immobile. Using the Hartree approximation we arrive at an expression for the ground state energy that is similar to that for the polaron energy. The difference with the polaron theory is that the electron-phonon strength k is now renormalized to an effective coupling $k_N = k\sqrt{N}$. Using the well known analytical expressions for the polaron ground state energy in the continuous and anticontinuous limit, we obtained the corresponding energy for the N-quanta problem. The main result is that in 2D and 3D, the condition that determines when a solution is extended or localized depends not only on the exiton-phonon coupling but also on the number of quanta and as a result an initially extended exciton can be gradually localized by increasing N.

CHAPTER 5

ADIABATIC POLARON THEORY FOR METAL-HALOGEN MATERIALS

We consider an intra-molecular excitation that interacts with optical lattice vibrations and analyze the ground state energy and wavefunction when N vibrational excitation quanta are present. In the one-dimensional case we find strong red-shifts in the overtone spectra and an increasing spatial localization as the number of quanta increases. Through model parameter fitting we achieve very good quantitative agreement with experimental Resonant Raman scattering measurements in the quasi-one-dimensional charge transfer solid PtCl. Accurate analytical expressions for the red-shifts are also obtained.

5.1 Introduction

Halogen-bridged transition-metal compounds, subsequently denoted as MX, have recently received much attention due to their quasi-one-dimensional structure that simplifies experimental investigations and theoretical modeling. Their structure consists of alternating transition metal (M = Ni, Pd or Pt) and halogen (X = Cl, Br or I) atoms along chains, which are aligned parallel to each other and surrounded by various types of ligand structure L (ethylamine, ethylenediamine, etc.). These materials are generally Peierls distorted, with the halide ions displaced from the central position to a location closer to the metals. The most important property of MX solids is the exhibition of a remarkable range of strengths of competing electron-electron and electron-phonon forces. This competition can be manipulated and tune MX ground state properties, either through application of pressure or by chemical variation of M, X, or L. This tunning produces a wide range of Peierls distortion: from the strong highly Peierls-distorted regime of PtCl, to the weakly distorted PtI or the undistorted case of PtBr. This tunability of the ground state provides the opportunity to obtain clear spectral signals of photoinduced gap states such as polarons, bipolarons, excitons, etc. that are accompanied by local lattice distortion. Both the low-dimensionality and the ability to tune in a controllable way the ground state makes MX compounds good model systems for testing theories of one-dimensional solids.

5.2 Experimental observation of intrinsic localized modes in PtCl

In the limit of strong electron-phonon interaction the photexcited gap states create a strong lattice deformation that effectively results to high anharmonic interaction between vibrational modes. This lattice anharmonicity and the discrete crystalline structure of MX materials are ideal properties for experimental observation of ILMs. Indeed, during 1999, Swanson et.al [35] reported experimental observation of ILM in PtCl that is a representative of MX family presenting the strongest electron-phonon interaction. Its

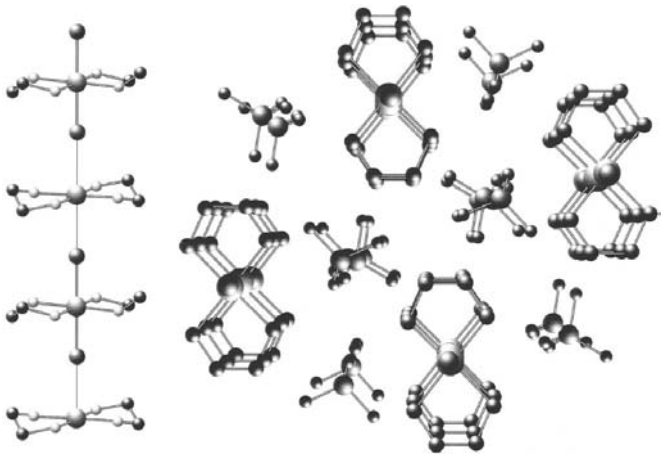

Figure 5.1: Structure of $\{[Pt(en)_2][Pt(en)_2Cl_2](ClO_4)_4\}$ (en = ethylenediamine; H atoms are omitted). One PtCl chain is shown on the left. Each Pt atom is coordinated by two ethylenediamine units in a near square planar geometry, while Cl^- ions connect the Pt sites along the chain. The packing arrangement of the 1D chains and their ClO_4^- counterions is shown on the right (see Ref. [35]) .

structure is shown in Fig. 5.1, and consist of quasi-one-dimensional array of repeated $\{Pt^{2+}\cdots Cl^- - Pt^{4+} - Cl^-\cdots\}$ units with $(en)_2$ [1] ligads attached to each Pt ion. The Cl^- ions are Peierls-distorted closer to Pt^{4+} ions. The distance Pt^{4+}–Cl^- is 2.318 Å, while $Pt^{2+}\cdots Cl^-$ is 3.085 Å.

Resonant Raman spectra were obtained using Ar^+ laser illumination at 514 nm of a single crystal of PtCl mounted in a close cycle helium cryostat at approximately 12 K. The fundamental frequency and the overtones spectra for pure $Pt^{35}Cl$ and $Pt^{37}Cl$ isotopic samples is presented in Fig. 5.2 and Fig. 5.3 respectively. The fundamental frequency for $Pt^{35}Cl$ is at 312 cm^{-1} while for $Pt^{37}Cl$ at 304 cm^{-1}. In both cases Resonant Raman Spectroscopy (RRS) indicates a strong red-shift of the overtones according to the fundamental frequency.

A simple brownian representation of RRS in PtCl presented in the work of Ref. [88] is shown in Fig. 5.4. In the first stage shown in Fig. 5.4 (a), a photon is absorbed and a hole is transferred form Pt^{4+} ion to Pt^{2+}. After this transfer, Cl^- is no longer at the minimum of its energy and starts to

[1] en=ethylenediamine

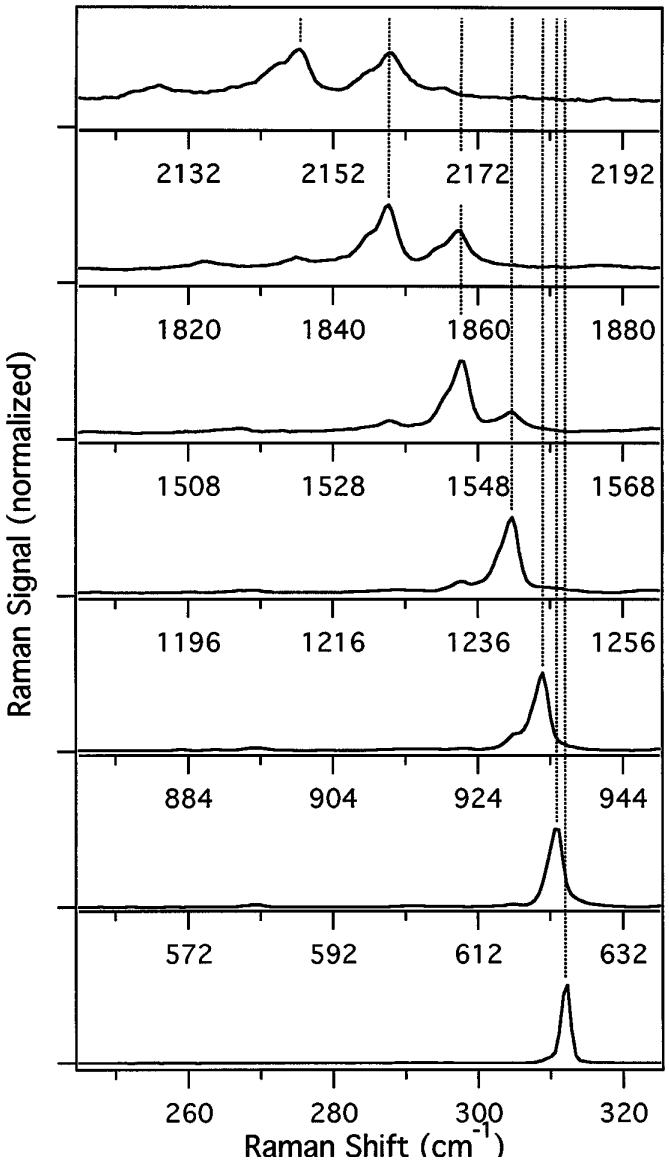

Figure 5.2: Fundamental and overtone spectra of isotopically pure $Pt^{35}Cl$. Moving upward in each panel, each x axis is offset by the appropriate integral multiple of the 312 cm^{-1} fundamental frequency. All spectra have been scaled vertically to equal peak intensities (see Ref. [35]).

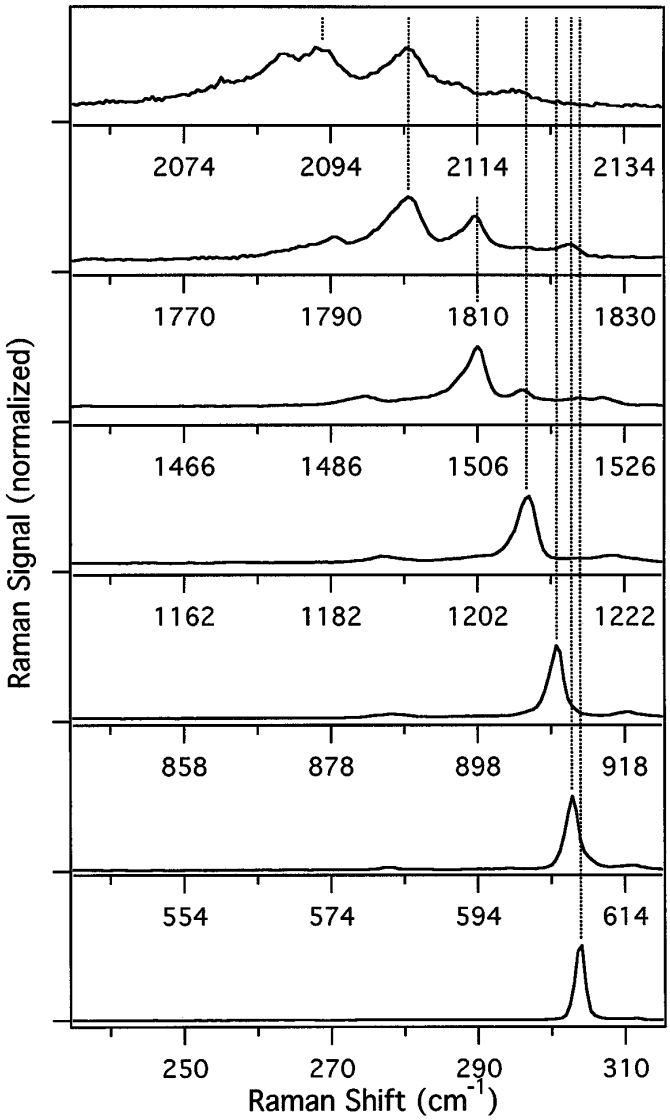

Figure 5.3: Fundamental and overtone regions of the isotopically pure $Pt^{37}Cl$, presented as in Fig. 5.2, but with 304 cm^{-1} offsets (see Ref. [35]).

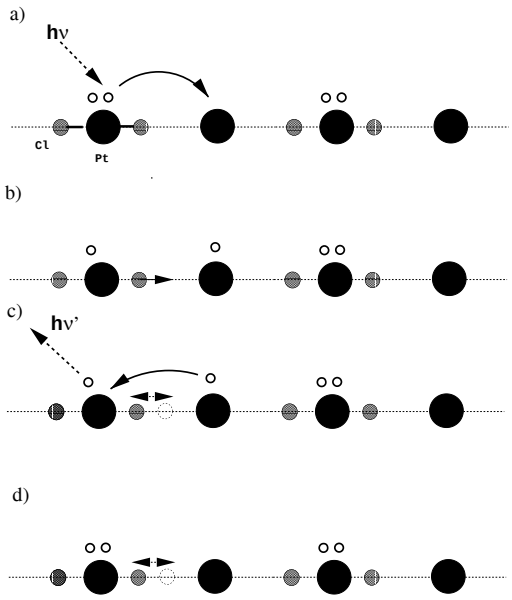

Figure 5.4: A simple picture of a resonant Raman scattering event in the localized (atomic) limit; explanation of the processes is given in the text (see Ref. [88]).

move toward to the left Pt ion (Fig. 5.4 (b)). After some time the hole hops back and a phonon is emitted (Fig. 5.4 (c)), while some energy remains in the lattice and Cl^- oscillates around its equilibrium position (Fig. 5.4 (d)). The quantum levels of this vibration are then observed as peaks in the RRS.

The concept of multi-quanta bound states in nonadiabatic and adiabatic Peierls-Hubbard models was used in order to explain this unusual red-shifted multi-quanta evolution of the fundamental frequency. In the former case a four-site model seems to fit the experimental results well [35, 89]. In the latter adiabatic case the success of the adiabatic approach is restricted to a small number of bound quanta, since at higher energies the theoretical predictions deviate significantly from the experimental observations [88]. In the former case, the potential disadvantages are the large number of system parameters, the small lattice size used in the numerical calculations, and the assumption that the vibrational quanta are almost localized at a single unit cell.

5.3 An effective multiquanta model for PtCl

In this work we use a simpler many-quanta effective model to describe the localization of the vibrational energy in molecular crystals. Our motivation is the simple picture offered in Ref. [88] [2] for an intra-molecular vibrational excitation on a trimer ($PtCl_2$) caused by charge transfer between Pt^{4+} and Pt^{2+}. Since such excitations are delocalized in an extended lattice due to quantum mechanical tunneling, a coupling with an external field is necessary for ILM formation. It is known that in materials like $PtCl$ there is a very strong interaction of the electronic motion with the ionic arrangement [90, 91]. The resulting nonlinearity through the electron-phonon coupling can be phenomenologically represented by an effective interaction of the intra-molecular mode with a bath of another degree of freedom. Here, we represent the latter by a soft optical phonon with frequency ω_0 lying in the range of the observed red-shifts. The effective coupling of the intra-molecular mode with optical phonons is easily connected with the calculated parameters of the underlying electron-phonon Hamiltonian [91], using a first order expansion of the electron induced nonlinear potential close to the anticontinuous limit. In such a model an adiabatic treatment of the optical phonons leads to a generalized Discrete Nonlinear Schrondiger equation (DNLS), allowing the localization of the vibrational excitation.

Specifically, we consider an one-dimensional chain each site of which corresponds to a $\{Pt^{2+}\cdots Cl^{-}-Pt^{4+}-Cl^{-}\cdots\}$ unit of PtCl. Assuming that an intra-molecular vibrational excitation (exciton) with on-site energy E_0 can hop from one site i to its nearest neighbors via the transfer matrix element J and also that it is locally coupled with the Einstein oscillators of frequency ω_0, then the resulting Hamiltonian is equivalent to that of Eq. (4.7) (in dimensionless units). In the adiabatic limit ($\gamma \to 0$) the corresponding generalized DNLS of N-excitons interacting with the lattice is given by Eq. (4.21).

5.3.1 Numerical Fit

As we already have described in Chap. 4, the strong nonlinearity due to the coupling with the lattice leads to greater localization and increased red-

[2] see also Sec. 5.2

shifts at higher energies. Similar features are observed in the experimental RRS overtone spectra of $PtCl$ [35]. Using our exact numerical procedure of Sec. 4.3, we can fit the experimental data of the overtone shifts of $PtCl$. According to our model the *relative* red-shift of the overtones

$$r_N(k, \epsilon_0) = \frac{NE_1 - E_N}{E_1} \tag{5.1}$$

depends on two model parameters: the coupling constant k and the on-site energy ϵ_0 of the quanta.

In Fig. 5.5 (a), we present the relative red-shifts calculated from our numerical results through parameter fitting, and compare them with the experimental data [35] for $Pt^{37}Cl$. The best fit is achieved for $k = 1.19$ and $\epsilon_0 = 191$. From these dimensionless values we obtain $J = 1.61\ cm^{-1}$ in order to have the first peak at $304\ cm^{-1}$, as observed in Ref. [35]. For the fitted value of coupling constant k the probability to find any quantum on site i (ρ_i/N) is displayed in Fig. 5.5 for the one, two and three vibrational localized excitons, respectively. We observe that the ILM corresponding to the second overtone $(N = 3)$ is localized on almost one lattice site in agreement with the experimental observations [35]. However, the adiabatic single localized exciton $(N = 1)$ is extended to about 15 unit cells. As a result, in the framework of the semiclassical equations of motion, the ILM can uniformly propagate through the lattice. Generally, the semiclassical mobility of such one-exciton ILMs is numerically tested for $k < 1.5$ (see Chap. 2 and Ref. [42]). The corresponding fit for $Pt^{35}Cl$ and the comparison with the experimental data [35] is shown in Fig. 5.5 (c). In this case the fitting parameters are $k = 1.15$ and $\epsilon_0 = 170$. The first peak at $312\ cm^{-1}$ for this isotope [35] is obtained for $J = 1.86\ cm^{-1}$.

5.3.2 Analytical Fit

In the anticontinuous regime ($k >> 1$), where ILMs are localized at one site, an analytical expression is available for the relative red shifts, obtained through substitution of Eq. (4.28) ([61]) in Eq. (5.1). Then

$$r_N(\beta) = \frac{1}{2\beta - 1}(N^2 - N)\ , \tag{5.2}$$

where $\beta = \frac{\epsilon_0}{k^2}$. This formula is not well applicable in the case of $PtCl$ since for small quanta numbers the ILM is not localized at a single unit cell (see Fig.3 for $N = 1$ and 2). Fitting of expression (5.2) with the $Pt^{37}Cl$ and $Pt^{35}Cl$ data is presented in Fig. 5.5 (b) and (d) respectively for comparison of the one-site localized adiabatic red-shifts (Eq. (5.2)), with the corresponding nonadiabatic results [89]. We see that the analytical, one-parameter adiabatic fitting is slightly worse than the numerical, multiple parameter nonadiabatic one.

However, a more convenient analytical description of the $PtCl$ red shifts can be found. As is clearly seen from Fig. 5.6, the one-quantum ILM is far from being single-site localized, and therefore its energy E_1 considerably departs from the anticontinuous limit value. On the other hand, in the same figure is also seen that the ILMs for higher number of excitons are almost localized at a single site. In Sec. 4.3.2 we have already present analytical expression of the N-excitons energy in both anticontinuous and continuous limit. Motivated by the numerical result of Fig. 5.6, we can improve the analytical expression of Eq. (5.2) for the relative redshift. Using Eq. (5.1), where E_1 is given by eq.(4.27) and E_N for $N \geq 2$ is given from eq.(4.29), we obtain for the relative red shifts:

$$r_N(k, \epsilon_0) = \frac{(\frac{k^2}{2}N^2 + \frac{2}{k^2} + \frac{1}{k^6 N^2}) - N(2 + \frac{k^4}{48})}{\epsilon_0 - (2 + \frac{k^4}{48})} \ . \tag{5.3}$$

Fitting this expression with the $Pt^{37}Cl$ data we find $k = 1.2$ and $\epsilon_0 = 195$ while for $Pt^{35}Cl$ $k = 1.17$ and $\epsilon_0 = 181$. In Fig. 5.5 (a) and (c), we plot Eq. (5.3) for the fitted values of parameters for $Pt^{37}Cl$ and $Pt^{35}Cl$ respectively. We note that this analytical relation approaches the experimental and the exact numerical data very well. A more accurate variational bridging of the continuous with the anticontinuous limit results is also possible [92].

5.4 Conclusions

In summary, inspired by experimentally observed intrinsic localization of vibrational energy in $PtCl$, we have studied a Holstein-type model describing intra-molecular *many* quanta excitations coupled with optical phonons. The adiabatic treatment of the lattice allows the numerical calculation of the N quanta ground state, which always forms an ILM. The inherent nonlinearity

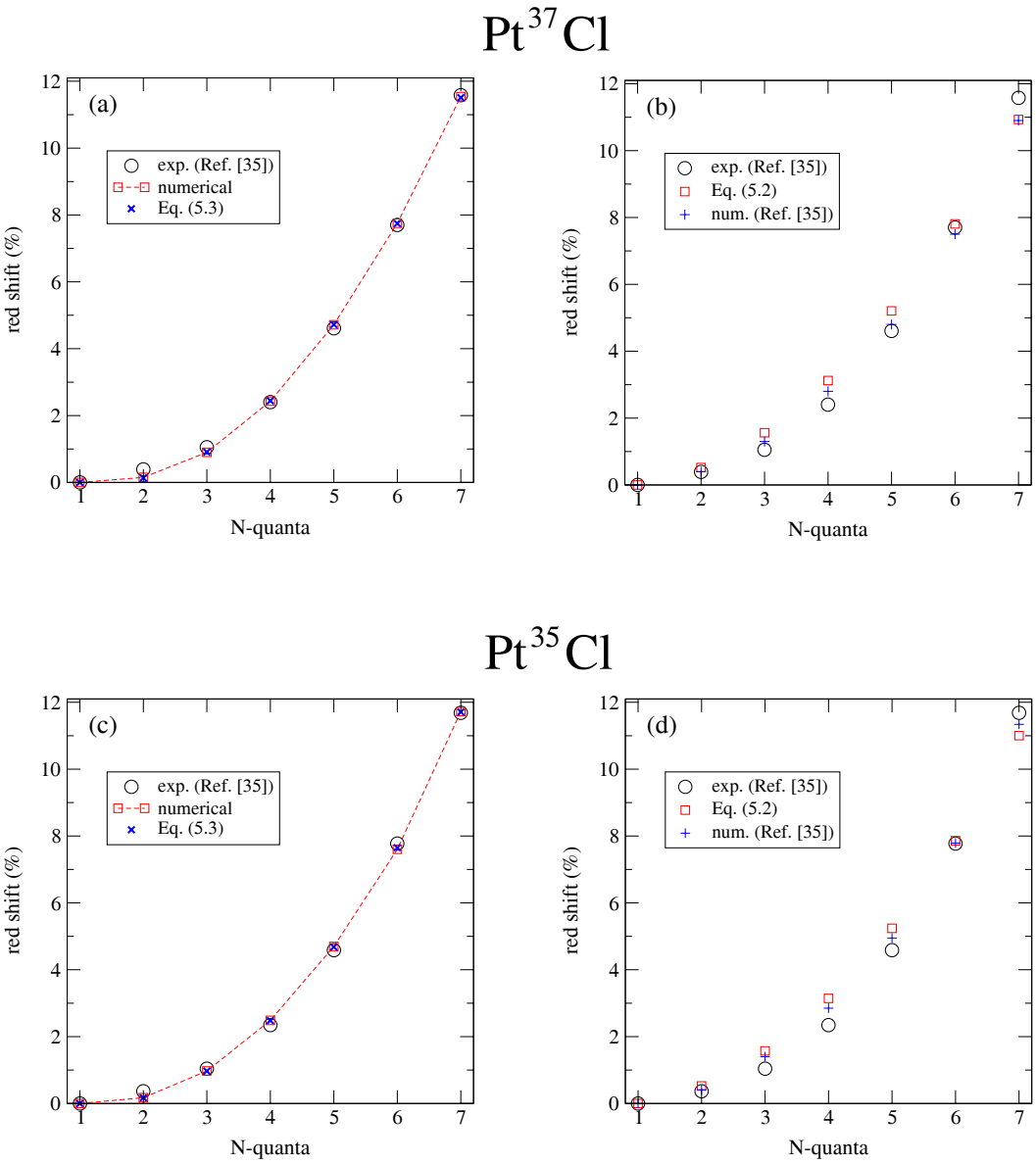

Figure 5.5: (a), (b): Relative red-shifts (%) of the $Pt^{37}Cl$ overtone spectra as a function of the number N of quanta. Circles are experimental [35] results. In subfigure (a), squares connected with the dashed line correspond to numerical fitting and data represented by **x** result from a analytical expression of Eq. 5.3. In (b), triangles result from the analytical one-parameter fitted expression in the anticontinuous limit (Eq. (5.2)), while crosses correspond to nonadiabatic numerical results of Ref. [35].
(c), (d): Relative red-shifts (%) of the $Pt^{35}Cl$ overtone spectra as a function of the number N of quanta. The symbols are equivalent to those of (a) and (b).

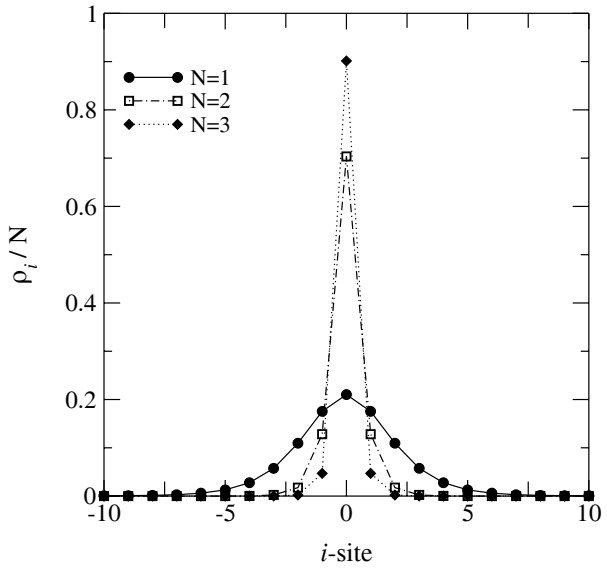

Figure 5.6: The probability of finding any quantum on lattice site i (ρ_i/N) versus i for $N = 1, 2$ and 3 quanta. The coupling constant is $k = 1.19$.

of the system results in stronger localization and correspondingly increased overtone red-shifts at higher energies. Fitting the two parameters of our phenomenological model, we achieve very good agreement with experimental data in $PtCl$ by a nonlinear renormalized one-quantum ILM extending over about fifteen unit cells. In the adiabatic approximation we are able to deal with ILMs that extend to many lattice sites and are not restricted to a single site, as usually assumed in nonadiabatic studies [93]. Using the continuous approximation for the single-quantum energy and the anticontinuous limit for the many-quanta energy, an accurate analytical expression is obtained for the $PtCl$ red-shifts. The physical mechanism underlying our model to explain the $PtCl$ ILMs is the formation of vibrational polarons (which should not be confused with electronic polarons). Possible application of the results presented in this work to other halogen-bridged mixed valence transition metal compounds or quasi one-dimensional molecular materials remains to be tested. A limitation of the proposed model is that it does not take explicitly into account the electronic degrees of freedom -that are actually responsible for the resulting strong nonlinearity- and consequently cannot predict electronic properties of the ILMs. These can be approximately provided through the electronic rearrangement involved in molecular vibrations and will be discussed elsewhere.

Part II

Discrete Breathers

CHAPTER 6

ENERGY RELAXATION IN DISCRETE NONLINEAR LATTICES

In this chapter, we present a brief review of the the breather construction methods and breather dynamical properties, as well as the numerical investigation of energy relaxation in discrete nonlinear lattices in one and two spatial dimensions. We find that energy relaxation follows a stretched exponential law and we study its dependence on the initial temperature. We attribute this behavior to hierarchies of discrete breathers that relax with different time constants leading to a hierarchy of relaxation time scales in the system. Using heuristic arguments we derive a nonlinear diffusion equation for the local energy density of the oscillators that results in similar relaxation dynamics.

6.1 Introduction: A brief review of discrete breather theory

During 1994, six years after the introduction of the breather concept [22], Mackay and Aubry [23] published the first rigorous theorem for DB existence as exact solutions of nonlinear lattices. In the preceding years, breathers were known to be approximate solutions that exist in very simple models. According to this theorem, DB existence requires not only lattice anharmonicity but also the condition that their frequency and its harmonics lie outside the linear phonon spectrum. Whenever the latter condition is not satisfied there is resonance with phonons and the breather solution decays. This occurs due to the extended nature of linear modes that can carry away DB energy destroying completely its localization. It is thus necessary the linearized spectrum to be bounded or to exhibit gaps. This condition is fulfilled only in the case of discrete systems; in continuous systems on the other hand phonon dispersion relation is extended to infinity (see for example [83]). Generally speaking, nonlinearity and discreteness are the essential properties of systems for breather existence.

The DB existence theorem is based in the concept of the anticontinuous limit and the model that was used in that work was a discrete 1D array of harmonically coupled nonlinear oscillators (Klein-Gordon systems). In the anticontinuous limit, where the coupling strength (C) between the ocsillators is zero, DBs are trivial solutions of such systems. In this limit, the simpler breather solution can be obtained if we initially displace a single oscillator in a given amplitude and keep the rest of them at their equilibrium position. Subsequently, the initially displaced oscillator can oscillates around the local minimum of the anharmonic potential, while the others remain static since there is no coupling between of them. Thus, in this simple example, we can have a localized solution (at one site) that is time periodic with frequency that depends on the initial oscillator displacement. Using the implicit function theorem, it can be proved that breathers can persist for $C \neq 0$ but for coupling values not greater than a maximum value, C_{max} . The theorem is

valid also in more complex systems of arbitrary dimensionality.

One of the main restriction of the approached based on the Mackay-Aubry theorem is the requirement that the systems contain on-site nolinearity; as a result, important models such as the Fermi-Pasta-Ulam (FPU) chains one cannot be incuded directly. However, in some cases as FPU chains, this problem can be overcomed [94] with a transformation that reforms the initial lattice Hamiltonian to a new one that contains an effective local nonlinear potential. In more complex nonlinear systems where this transformation is impossible, we can alternatively use a fictitious on-site potential that enables us initially to find a breather solution. It has been shown [94] that by decreasing gradually the magnitude of this potential, breather solutions can exist even in the limit where this potential is completely disappeared.

As an example of the above procedure we present here a specific breather solution and its dynamical behaviour [95]. We assume a 1D Klein-Gordon system with double-well (ϕ^4) on-site lattice nonlinearity:

$$H = \sum_i [\frac{p_i^2}{2} + \frac{C}{2}(x_i - x_{i-1})^2 + \frac{1}{2}(1 - x_i^2)^2], \tag{6.1}$$

where p_i and x_i are the momentum and the displacement from the equilibrium position of the i-th oscillator respectively, and C is the harmonic coupling strength between nearest neighboring oscillators. A breather solution that is obtained using the method of the anticontinuous limit is presented in Fig. 6.1, where is the spatial exponential decay of solution is observed. The time evolution of this breather is presented in Fig. 6.2.

For eight years, the study of breathers was restricted in their construction methods and their dynamical properties. In 1996, D. Chen *et.al.* [25] presented a numerical method for constructing mobile breathers in one-dimensional systems. This method was based on an appropriate perturbation of the velocity variables $\{\dot{x}_i\}$ in the direction of the corresponding part of the pinning-mode. In that work, authors also present results about the effective mass and collision properties of breathers. In Fig 6.3 [95] is shown the time evolution of the breather presented in Fig. 6.1 and 6.2

The idea of using the pinning mode in order to excite DBs and render them mobile is restricted only in the systems where this mode exists. For example in systems with hard-ϕ^4 on-site nonlinearity the pinning mode does not exist and as a result the generation of moving breathers is impossible.

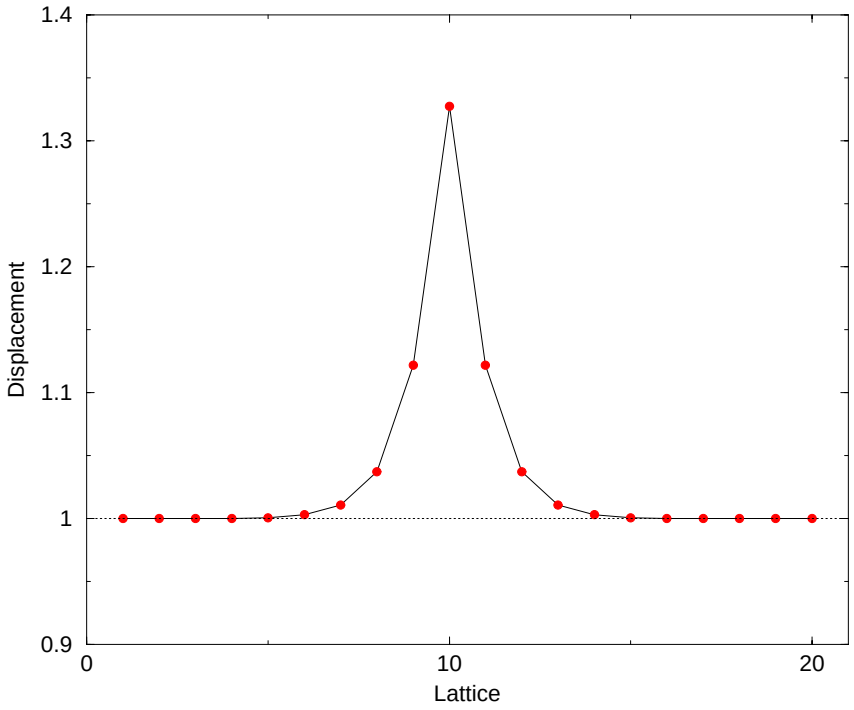

Figure 6.1: A single breather in the double-well ϕ^4 potential. of frequency $w_b = 1.32$ and coupling strength $C = 0.131$ [95].

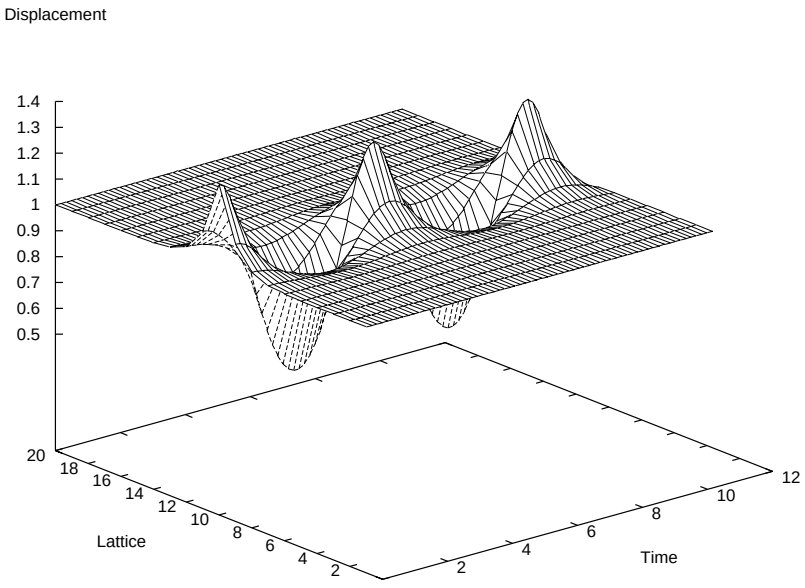

Figure 6.2: Time evolution of the initial breather state of Fig. 6.1 [95].

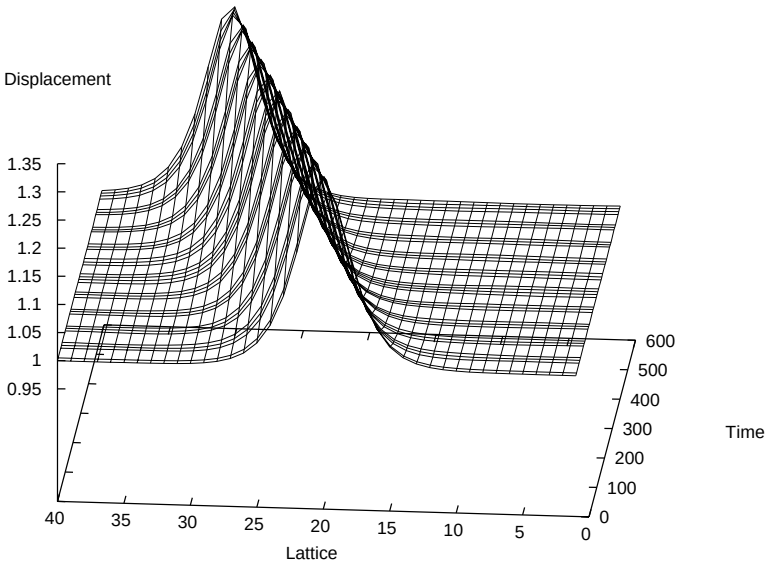

Figure 6.3: Time evolution of the mobile breather presented in Fig. 6.1 The breather is plotted every period [95]

This problem was overcomed in 2001 [28, 96] when instead of pinning mode the derivative of the breather solution was utilized. The latter trick enables the construction of moving breathers almost in any nonlinear system. Since then, many works where done, extending the study of mobile breathers in more complex systems such as biological models, in any dimension. It is worthwhile noting that the method of pinning mode is also applicable in polaron theory [42]. In Chap. 2, we used this method to construct moving polarons in the adiabatic Holstein model [7] in one-, two-, and three dimensions. However, we should mention that this method is approximate and small energy emission due to the initial perturbation is observed. The existence of exact moving DB solution is an open question in breather theory.

6.2 Nonlinear lattices out of thermodynamic equilibrium

It is well known that when some initial energy amount ($E(0)$) is locally injected in a harmonic system, it relaxes spontaneously to thermal equilib-

rium following the standard diffusion laws of heat. Energy relaxation of the normalized total energy $E(t)/E(0)$ is a simple exponential that does not depend on the initial energy. However, there are more complex systems, such as spin glasses, polymers and biopolymers [97], that present an 'unusual' slow relaxation behaviour at low temperatures. This is closely associated with the existence of many metastable states separated by energy barriers, that forbid easy energy transfer across the system. Recently, it has been shown [26] that anomalous relaxation phenomena can also appear in nonlinear lattices at relatively high temperatures. In this case, the reason for the energy localization is the spontaneous breather generation that can persist for very long times. At low temperatures, nonlinear systems become actually linear and the energy relaxation follows the standard exponential law. In this section, we show that the spontaneously breather generation in nonlinear lattices leads to a stretched exponential energy relaxation rate that depends on the initial lattice temperature. The model used for that propose is described below.

We consider a two dimensional nonlinear lattice constituted typically of 44x44 lattice sites. The nonlinear oscillators located at each site interact linearly with their nearest neighbors through coupling constants k_x and k_y in the x and y directions of a square lattice respectively. The Hamiltonian of the systems is:

$$\begin{aligned} H &= \sum_{<i,j>}^{N} [\frac{1}{2}\dot{u}_{ij}^2 + \frac{1}{2}k_x(u_{i+1,j} - u_{i,j})^2 \\ &\quad + \frac{1}{2}k_y(u_{i,j+1} - u_{i,j})^2 + V(u_{ij})] \end{aligned} \tag{6.2}$$

where the indexes i, j refer to the x and y direction respectively, $u_{ij} \equiv u_{ij}(t)$ is the oscillator displacement at site (i,j) while $V(u_{ij})$ is the on-site nonlinear potential in the same location. For the present work we used the following three different on-site potentials ($x \equiv u_{ij}$):

$$V_1(x) = \frac{1}{2}x^2 + \frac{1}{4}x^4 \tag{6.3}$$

$$V_2(x) = \frac{1}{2}\left[1 - e^{-x}\right]^2 \tag{6.4}$$

$$V_3(x) = \frac{1}{2}\frac{x^2 + ax^4}{1 + x^2}, \quad a = 0.2 \tag{6.5}$$

The potentials $V_1(x)$ and $V_2(x)$ are the "hard" - ϕ^4 and the Morse potentials

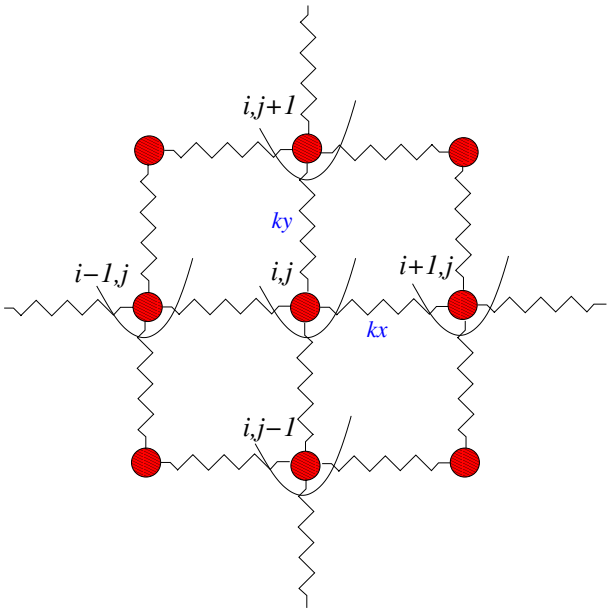

Figure 6.4: A schematical representaion of the model (see text for details)

respectively, while $V_3(x)$ has been used in the work of Ref. [98]. A schematical representation of the model is shown in Fig. 6.4.

The investigation of the lattice energy relaxation follows closely the method of ref. [26]. We use initially a Langevin algorithm in order to bring the system at a given initial temperature T. Subsequently, we bring the system in contact with a zero temperature bath created through two layers of border oscillators that are damped. Due to the presence of the zero-temperature heat bath the nonlinear system relaxes to equilibrium (at zero temperature) following the dynamical equations of motion:

$$\begin{aligned} \ddot{u}_{ij} &= k_x\left(u_{i+1,j} - 2u_{ij} + u_{i-1,j}\right) + k_y\left(u_{i,j+1} - 2u_{ij} + u_{i,j-1}\right) \\ &\quad -V'(u_{ij}) - \gamma(\delta_{i,\mu} + \delta_{j,\mu})\dot{u}_{i,j} \end{aligned} \tag{6.6}$$

where δ denotes the Kronecker delta and $\mu = 1, 2, 43, 44$ are the border oscillators. The mass of the oscillators was set to unity. We note that in Eqs. (6.10) each degree of freedom u_is is scalar.

6.3 Spontaneous breather generation

The total energy of the system is numerically evaluated by solving equations of motion with the fourth order Runge-Kutta method. Several initial

configurations are used for the averaged total energy relaxation as a function of time. Results of the normalized total energy relaxation for all three on site potentials at different lattice temperatures are shown in Fig. 6.5. We note that, as in the one dimensional case [26], strong departure from an expected exponential relaxation at progressively higher initial temperatures. This occurs, due to the increased stability of the breather modes with energy (temperature) leading to longer and longer relaxation time scales. The process of nonlinear lattice relaxation proceeds through a cascade of nested processes: at earlier times linear (phonon) mode transfer and dissipation occurs, while also energy nonlinear modes (low energy breathers lying above the energy gap [99]) also dissipate. Subsequently, as time passes, higher and higher energy modes relax and dissipate. The hierarchy of relaxation processes is manifested empirically in a sequence of pseudo characteristic times [100] $t_1^* < t_2^* < ...$ in between which the energy relaxation curve can be approximated by exponentials of the form $e^{-\sigma t}$, with $\sigma = \sigma(T)$, *i.e* with a temperature dependent time constant. An example of such behavior is depicted in Fig. 6.5 (d) for the potential V_1 at an initial temperature $T = 0.2$ This figure shows that at early times (in units of 100 periods of the linearized potentials) phonon dissipation takes place while breather relaxation occurs much latter. We also show the slow time evolution after the pseudo-characteristic time t^* [100]. The empirical study of the lattices of the three potentials V_1, V_2 and V_3 has demonstrated that in the case of the immobile breathers of the potential V_1 a single pseudo-characteristic time t^* suffices for the characterization of the relaxation properties of the lattice (as in the case of reference [100]) while for the mobile breathers of the softer potentials V_2 and V_3 the relaxation process is more complex, leading to a sequence of event times.

The relative participation of linear and non linear modes in energy relaxation for the hard V_1 potential is seen clearly in Fig. 6.6 while in Fig. 6.7 we focus on a specific lattice neighborhood occupied by a localized breather mode and and follow its time development (see Fig. 6.8 for better view). We notice the relative robustness of the breather mode once formed, and the very slow dissipation of the adjacent sites.

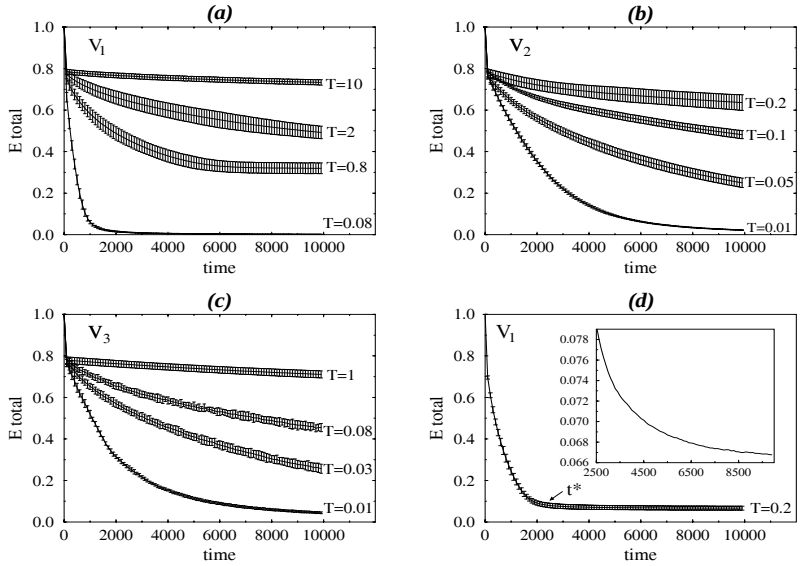

Figure 6.5: Normalized energy relaxation as a function of time for potentials in (a) V_1, (b) V_2 and (c) V_3 each at four different temperatures. In (d) we plot the energy relaxation for potential V_1 with initial temperature $T = 0.2$ and show the presence of a pseudo-characteristic time t^*. In the insert we show energy relaxation for $t > t^*$.

6.4 Stretched exponential energy relaxation

Extensive numerical simulations with all three potentials and use of χ^2-fitting has shown that the following stretched exponential form fits well the energy relaxation curves:

$$E(t) \;=\; E(0)\; e^{-\alpha t^{\beta}} \tag{6.7}$$

where the coefficients $\alpha,\ \beta$ are temperature dependent. The best fits for $\alpha = \alpha(T)$ and $\beta = \beta(T)$ for the three potentials considered here are shown in Fig. 6.9 as a function of the initial temperature T. We note that the fit for the hard-ϕ^4 potential V_1 was better ($\chi_1^2 \approx 10^{-5}$) than the corresponding one for V_2 ($\chi_2^2 \approx 10^{-4}$). We found that both curves $\alpha(T)$ and $\beta(T)$ are well fitted by the following function:

$$f(T) \;=\; \frac{c}{1 + [\frac{T}{T_0}]^p} \;+\; d \tag{6.8}$$

where $\chi^2 \approx 10^{-4}$. While the exponent p as well as the parameters c, d and T_0 vary depending on the potential used, it is remarkable that a single functional

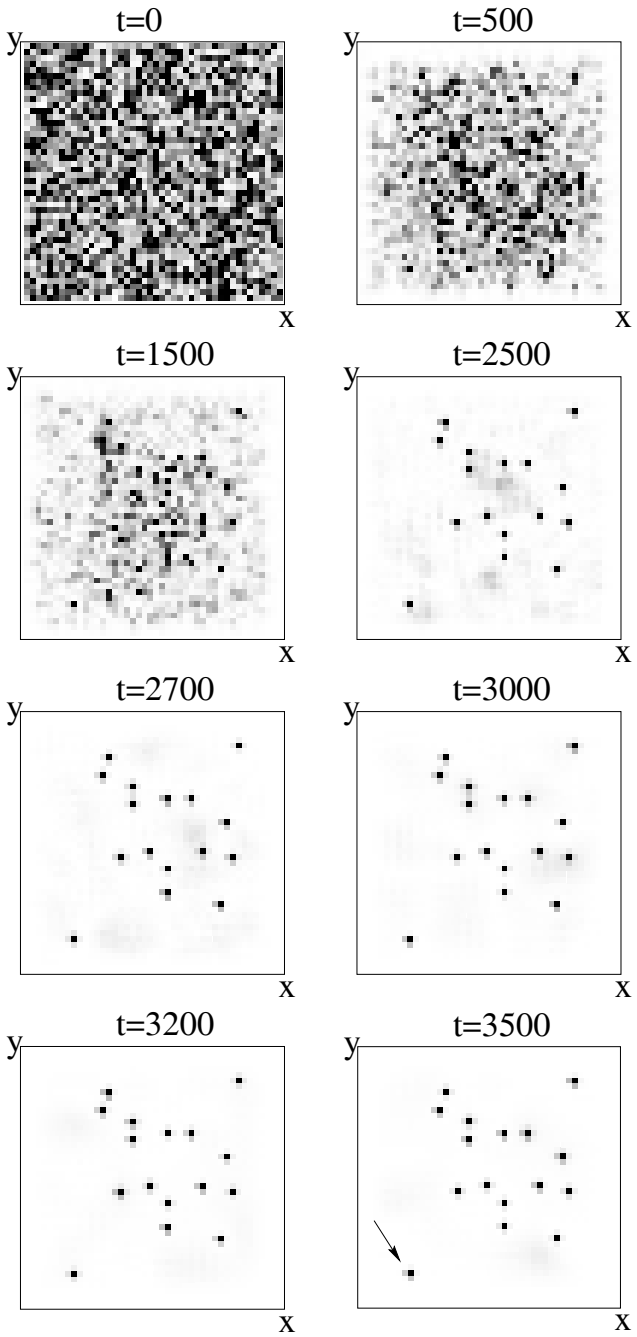

Figure 6.6: Spatiotemporal breather energy landscape. We follow the approach to equilibrium of a 2d lattice with on-site potential V_1 and initial temperature $T = 0.2$. We plot the symmetrized local energy density (darker spots designate higher local lattice energies) in two spatial dimensions and note the persistence of breathers to times much longer after the phonon dissipation. The arrow designates a breather whose time evolution is depicted in Fig. 6.7

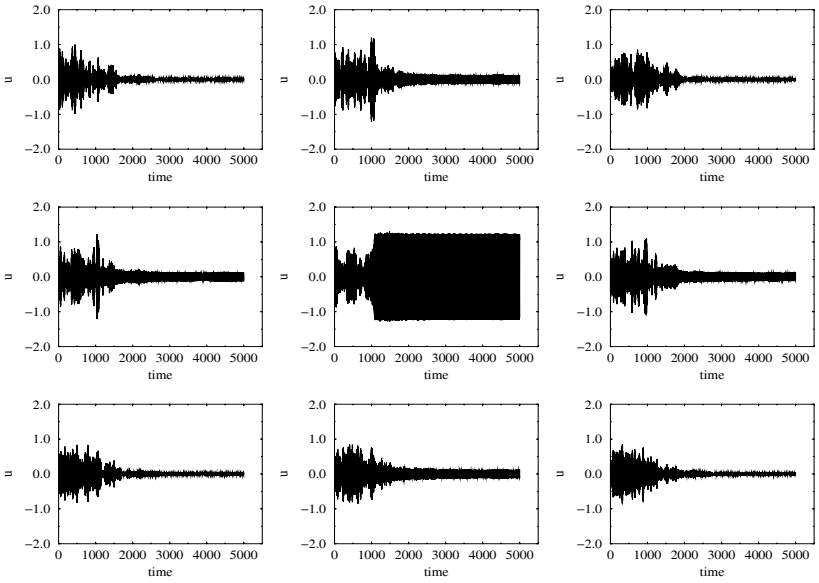

Figure 6.7: Time evolution of a spontaneously generated breather event (shown with an arrow in Fig. 6.6) in a 2d lattice with on-site potential V_1 and initial temperature $T = 0.2$. We follow the central cite as well as the eight sites around the dominant breather site. The coherence between the central site and the nearest neighbor sites is evident.

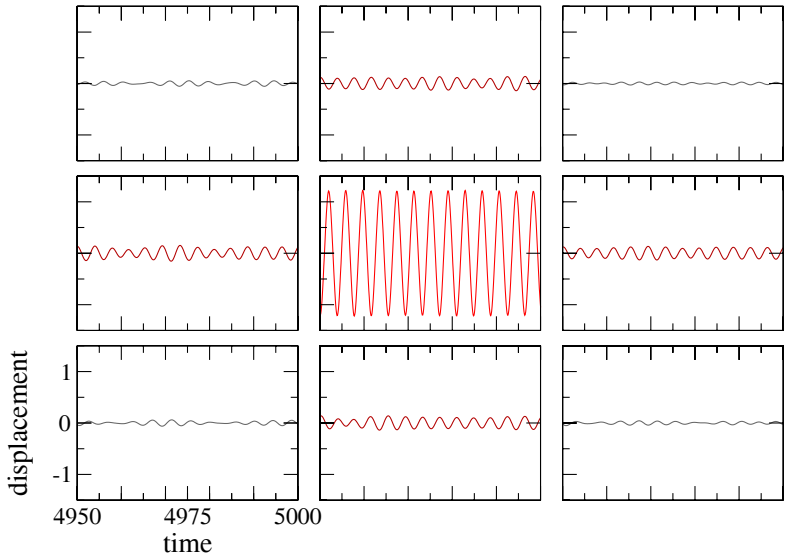

Figure 6.8: A zoom in time of Fig. 6.7 for better view of breather evolution.

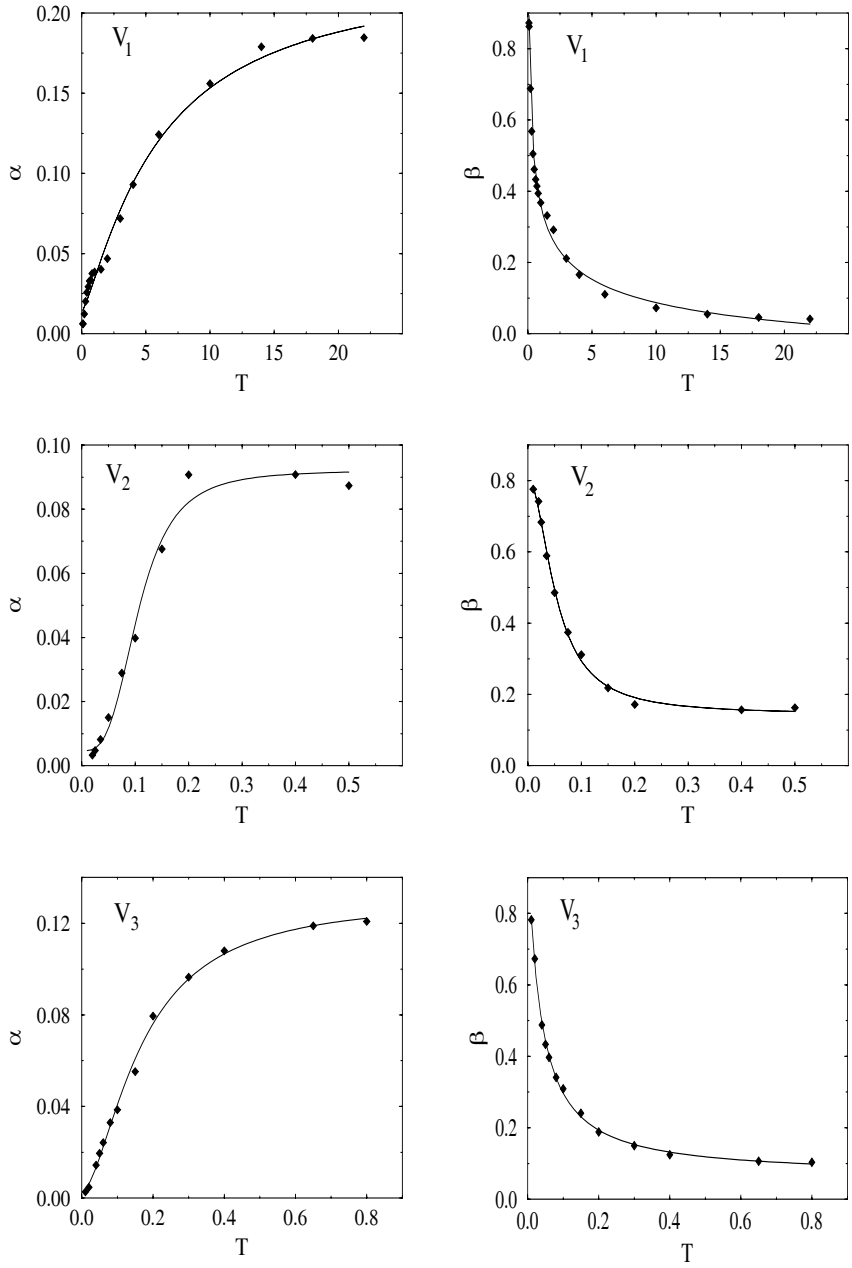

Figure 6.9: Numerical data and best fits for the stretched exponential parameters α (left column) and β (right column) for all three potentials V_1, V_2 and V_3 (from top to bottom) as a function of temperature T.

expression fits well both the temperature-dependent exponent $\beta(T)$ as well as the prefactor $\alpha(T)$.

An intuitive model for statistical energy relaxation in a breather infested system would have to take into account the observed fact that the energy transfer rate from a breather site to adjacent sites diminishes with the energy disparity between the sites. Considering for simplicity the one dimensional case and denoting by ρ_n the energy density at a lattice site n, we can postulate a rate equation for the energy randomization process as

$$\dot{\rho}_n = f(\rho_{n+1} - \rho_n)(\rho_{n+1} - \rho_n) + f(\rho_{n-1} - \rho_n)(\rho_{n-1} - \rho_n) \tag{6.9}$$

where $f(x)$ is an appropriate even function.

Assuming as a first step a continuum limit where $\rho_n(t)$ turns into $\rho(x,t)$, Eq. (6.9) becomes a nonlinear diffusion equation of the form

$$\rho_t \;=\; (f(\rho_x)\rho_x)_x \tag{6.10}$$

where subscripts denote differentiations with respect to the corresponding variable and the nonlinear function $f(\rho_x)$ should be a monotonously decreasing function. It is known that nonlinear diffusion equations of this and similar types result in algebraic time evolutions and posses self-similar solutions[101]. We thus find that the emerging picture of energy diffusion in extended nonlinear systems is one involving non-standard relaxation [102], multiple time-scales and multifractality, as also was seen from the simulation.

These properties could possibly lead to unconventional energy scaling with the system size, a feature that have been observed in lattices with long range interactions [103].

6.5 Conclusions

Numerical experiments with one and two dimensional nonlinear lattice systems have shown that the presence of breathers induces a stretched exponential lattice energy relaxation in the system. This law stems from the hierarchical relaxation processes that occur in these complex extended systems. The stretched nature of the exponential relaxation signifies that the dynamical processes involving nonlinear localized modes have fractal or multi-fractal nature that needs to be explored. Furthermore, the heuristic connection with

a porous medium-like relaxation corroborated the complex, multi-fractal nature of the processes involved. The results from numerical experiments presented here call for a statistical theory that will explain the specific temperature relaxation laws of extended nonlinear lattice systems.

CHAPTER 7

DISCRETE BREATHERS IN REAL SYSTEMS

In this chapter, we propose a practical numerical method for breather generation. The main advantage of this method is that it is applicable in any system independently of dimensionality and the complexity of its force field. This enables us to search for DB existence in real systems. Using this method, we investigate breathers solutions in Benzene and crystalline Silicon. Other properties of breathers such as energy and stability are also discussed.

7.1 Introduction

The method that is mostly used during several years for breather construction is that the one based on the Anticontinuous Limit (AL) concept [23]. The main advantage of this method is its high accuracy since it does not assume any theoretical approximation and as result its accuracy depends only on machine precision. However, from the computational point of view this method is very slow because it encompasses a demanding numerical computation of a tanget map matrix and its inverse [94]. In practice, the application of the AL is restricted only in very simple 1D models.

During the last years, a great effort has been devoted in developing more efficient numerical methods that are applicable in systems with higher dimensionality. Other methods in this direction are the Rotating Wave Approximation (RWA) [22] and the Algebraic Method (AM) [104]. Both these methods are approximate since they are based on the assumption that the space and time part of the breather solution are decoupled. In the RWA this separation of variables is effected through use of only the first term of Fourier expansion of the breather solution and assumes that the time-dependent part is eliminated from the equations of motion. The space part of DB can be determined by solving numerically the resulting nonlinear system of equations. The AM assumes that the time part of the Newton equation can be solved analytically and thus only the space part remains that is computed in way similar to that of the RWA. Comparing the RWA and the AM methods we find that the second is more accurate since in latter the time part of the breather solution is solved exactly.

The main disadvantage of the methods described previously is that they are restricted only to systems where the force field is given by an analytical expression. If this expression is more complicated, then these methods are not actually applicable. In the case where the potential is given only numerically, as in framework of Tight Binding Molecular Dynamic (TBMD), the application of these methods is not possible.

In the following section, we develop a practical method for finding DBs that works for general complex force fields that is based on the Fourier ex-

pansion of the space variables.

7.2 A practical method for breather construction in complex systems

We assume a d dimensional system of atoms that are moving under the influence of a general force field. The equation of motion of each atom is

$$m_i \ddot{\mathbf{R}}_i(t) = \mathbf{F}_i(\{\mathbf{R}_i(t)\}), \tag{7.1}$$

where m_i and $\mathbf{R}_i$ is the mass and position vector of atom i respectively, while $\mathbf{F}_i$ is the force exerted on atom i by all the other atoms of the system.

For each of these atoms we seek a breather solution with frequency ω_b that is outside the phonon band. The time evolution of the breather solution for each atom i has a Fourier expansion expressed as follows:

$$\mathbf{R}_i(t) = \sum_{n=0}^{n_{max}} \tilde{\mathbf{R}}_{i,n} \cos(n\omega_b t), \tag{7.2}$$

where $\tilde{\mathbf{R}}_{i,n}$ is the time Fourier Transform of $\mathbf{R}_i(t)$ and n_{max} is the maximum harmonic to be used in the expansion; when $n_{max} \to \infty$ Eq. (7.2) is exact. We note that the force $\mathbf{F}_i(t)$ is also periodic in time with frequency ω_b and, as result, Newton's equations of motion in the frequency domain become

$$\tilde{\mathbf{R}}_{i,n} = -\frac{\tilde{\mathbf{F}}_{i,n}}{m_i n^2 \omega_b^2}, \quad n = 1, ..., n_{max}, \tag{7.3}$$

where $\tilde{\mathbf{F}}_{i,n}$ is the Fourier transform of $\mathbf{F}_i$.

We seek solutions for ω_b and $\tilde{\mathbf{R}}_i$ as given in Eq. (7.3). The solutions are found **iteratively** using the procedure described below. (superscripts "( )" denote the number of the iterative step)

- **Step (0):** Guess an initial value for the breather frequency $\omega_b^{(0)}$ outside the phonon band.

  Denoting by J the breather central site, we set the initial atomic positions $\mathbf{R}_i[0]$ as

  $$\mathbf{R}_J(0) = \mathbf{Z}_J, \text{ and } \mathbf{R}_i(0) = 0 \text{ for } i \neq J,$$

and

$$\tilde{\mathbf{R}}_{i,1}^{(0)} = \mathbf{R}_i(0), \quad \tilde{\mathbf{R}}_{i,n} = 0 \ \text{ for } \ n > 1,$$

where $\mathbf{Z}_J$ is fixed quantity.

- **Step (1):**

  (a) Computation of force on each atom i assuming that the other atoms move according to $\mathbf{R}_i^{(0)}(t)$

  (b) Computation of the Fourier transform of the force $\mathbf{F}_i^{(1)}(t)$ acting on each atom i for all harmonics, i.e.,

  (c) Computation of the Fourier transform of the atomic position vector $\mathbf{R}_i(t)$ for each atom using Eq. 7.3, i.e.,

$$\tilde{\mathbf{R}}_{i,n}^{(1)} = -\frac{\tilde{\mathbf{F}}_{i,n}^{(1)}}{m_i n^2 (\omega_b^{(0)})^2}, \quad n = 1, ..., n_{max},$$

  excluding the first harmonic of the central breather atom which is held constant and thus does not depend on ω_b:

$$\tilde{\mathbf{R}}_{J,1}^{(1)} = \mathbf{Z}_J.$$

  (d) Recomputation of the breather frequency ω_b using the first harmonic of the central-atom position and force vectors. The new breather frequency $\omega_b^{(1)}$ that replaces $\omega_b^{(0)}$ is the solution of the equation

$$m_J (\omega_b^{(1)})^2 \tilde{\mathbf{R}}_{J,1}^{(1)} + \tilde{\mathbf{F}}_{J,1}^{(1)} \ = \ 0.$$

  The quantity $\tilde{\mathbf{F}}_{J,1}^{(1)}$ contains the effect of all other atomic positions and in general, $\omega_b^{(1)} \neq \omega_b^{(0)}$.

Step (1) is repeated and after k iterations we obtain

$$\tilde{\mathbf{R}}_{i,n}^{(k)} = \frac{\tilde{\mathbf{F}}_{i,n}^{(k)}}{m_i n^2 (\omega_b^{(k-1)})^2}$$

always excluding the first harmonic of the central atom that is held constant. The breather frequency in the kth step satisfies the equation

$$m_J (\omega_b^{(k)})^2 \tilde{\mathbf{R}}_{J,1}^{(1)} + \tilde{\mathbf{F}}_{J,1}^{(k)} \ = \ 0.$$

The procedure ends when there is convergence to specific values of ω_b and $\tilde{\mathbf{R}}_i$.

In the case of $n_{max} \to \infty$ the resulting breather solution is exact. Although we note that we have neglected the contribution of the harmonic $n = 0$ since it cannot be determined through Eq. (7.3). In practice this coefficient is very small for symmetric potentials and does not affect significantly the solution. Furthermore improvement of this method in the case of non-symmetric potentials by using Car-Parinello technique is in progress and will be present elsewhere. Extensive numerical testing of this method in simple models has shown that we can obtain solution with sufficient accuracy compared with the exact solution of the anticontinuous limit method. Moreover this method is remarkably faster than the AL method. In the next two sections we use this method to search the possibility of DBs existence in real systems.

7.3 Benzene Breathers

Most real systems in condensed matter physics and biology are described with models that are characterized by strong nonlinearity. Although this property is ideal for the breather existence there little work on this direction in the literature [105–107] primarily because an algorithm for DB construction in real systems does not exist. The method described previously provides however an efficient tool for DB construction in real systems. To test the validity of the method, we choose first the benzene, one of the simplest representative of organic compounds. Benzene (C_6H_6) is an aromatic hydrocarbon that consists of six carbon atoms (C) and six hydrogen atoms (H) arranged in a ring structure (see Fig. 7.1). One hydrogen atom is attached to each carbon while the latter atoms are connected with alternating double and single bonds. The distance length between carbons is the same for single and double bonds and equal to the 1.401Å, while $C-H$ distance is 1.081 Å.

Although benzene is seemingly a simple molecule, any realistic representation of it would involve highly nonlinear interatomic interactions making it a good candidate for having DBs. In order to study this possibility we use the Merck Molecular Force Field (MMFF) [108]. This is an empirical potential that is characterized by high nonlinearity since it includes almost all internal terms (bonds, angles, stretch-bend, out-of-plain bending and dihedrals) as

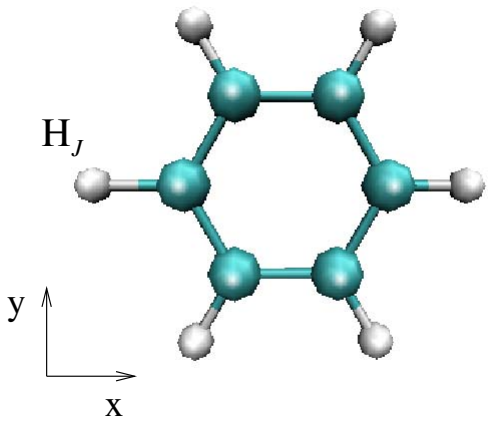

Figure 7.1: Benzene structure. Large circles (green) correspond to carbon atoms, while the smaller ones (white) to hydrogens. H_J denotes the central hydrogen of breather.

well as van der Walls and electrostatic terms; MMFF is briefly described in the following subsection.

7.3.1 Merck Molecular Force Field (MMFF)

The total energy of MMFF is the sum of the following individual energy terms (subscript '0' denotes the value of each variable at the equilibrium position):

- **Bond**

$$E_{bond} = K_{bond}(r_{ij} - r_{ij}^0)^2(1 + cs(r_{ij} - r_{ij}^0) + \frac{7}{12}cs^2(r_{ij} - r_{ij}^0)^2),$$

  where K_{bond} is the force constant, r_{ij} bond length between atoms i, j and cs the so called cubic-stretch constant.

- **Angle Bending**

$$E_{angle} = K_\theta(\theta_{ijk} - \theta_{ijk}^0)^2(1 + cb(\theta_{ijk} - \theta_{ijk}^0)),$$

  where K_θ is the force constant, θ_{ijk} bond angle between atoms i, j and k, and cb the cubic-bend constant.

- **Near Linear/Linear Angle**

$$E_{angle,linear} = K_{ijk,linear}(1 + cos(\theta_{ijk})),$$

where $K_{ijk,linear}$ is the corresponding force constant

- **Stretch-Bond**

$$E_{stretch-bond} = [K_{ijk}(r_{ij} - r^0_{ij}) + K_{kji}(r_{kj} - r^0_{kj})](\theta_{ijk} - \theta^0_{ijk}),$$

where K_{ijk} and K_{kji} are the force constants coupling ij the kj stretches to the ijk angle.

- **Out-of Plane Bending**

$$E_{OOP} = K_{OOP}(\chi_{ijk;l}),$$

where K_{OOP} is the force constant and $\chi_{ijk;l}$c is the angle between the bond jl and the plane the ijk, where j is the central atom.

- **Dihedral/Torsial**

$$E_{torsion} = \frac{1}{2}[V_1(1 + cos(\Phi)) + V_1(1 + cos(2\Phi)) + V_1(1 + cos(3\Phi))],$$

where V_i, $i = 1, 2, 3$, is force constants for the terms in the Fourier series and Φ the dihedral angle.

- **Van der Waals**

$$E_{vdW} = \epsilon_{ij}(\frac{1.07R^*_{ij}}{R_{ij} + 0.07R^*_{ij}})^7(\frac{1.12(R^*_{ij})^7}{R^7_{ij} + 0.07(R^*_{ij})^7}),$$

where R^*_{ij} is the minimum interaction energy distance between atoms i and j (based on parameterized atomic polarizability), and ϵ_{ij} the well depth between atoms i and j (based on the Slater-Kirkwood expansion, including polarizability and number of electrons).

- **Electrostatic**

$$E_{electrostatic} = \frac{q_i q_j}{D(R_{ij} + \delta)^n},$$

D is the dielectric constant, δ the electrostatic buffering constant and q_i the atomic charge on atom.

All benzene properties, such as ground state energy, forces or vibrational spectrum are calculated by using CHARMM (Chemistry at HARvard Molecular Mechanic) program written by Carplus and co-workers (1983) [109].

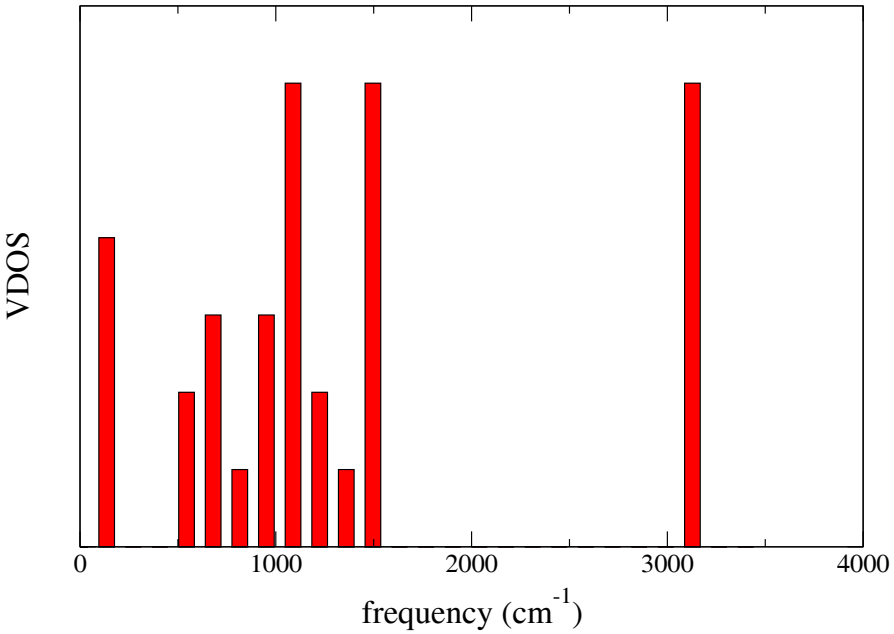

Figure 7.2: Vibrational Density Of States (VDOS) for C_6H_6

7.3.2 Breather generation in Benzene

The vibrational spectrum of benzene is made of two bands. The upper one corresponds to the $C-H$ stretching while the lower to the rest of benzene normal modes. The Vibrational Density Of States (VDOS) of benzene using MMFF, is presented in Fig. 7.2. We will present results for breathers that correspond to the $C-H$ stretching.

In order to construct a classical breather in benzene we choose a single hydrogen as a central particle (see Fig. 7.1). The initial displacement from the equilibrium position is $|\delta\mathbf{R}_J^{(0)}| = 0.1\ \mathring{A}$ towards to the nearest carbon atom, while for the initial breather frequency we chose $\omega_b^{(0)} = 3091\ cm^{-1}$. In this example, using fifteen harmonics in the Fourier expansion, our method converged after 10 iterations to the frequency $\omega_b = 3234\ cm^{-1}$. In Fig. 7.3, we present the convergence of breather frequency for each iterative step. The final amplitude of the central hydrogen is $|\mathbf{R}_J| = 0.11\mathring{A}$ that is greater than the initial one due to the contribution of the other harmonics. The nearest carbon to the central hydrogen is displaced on the opposite direction with smaller amplitude. The amplitudes of the rest atoms are smaller as we move away from the central hydrogen atom.

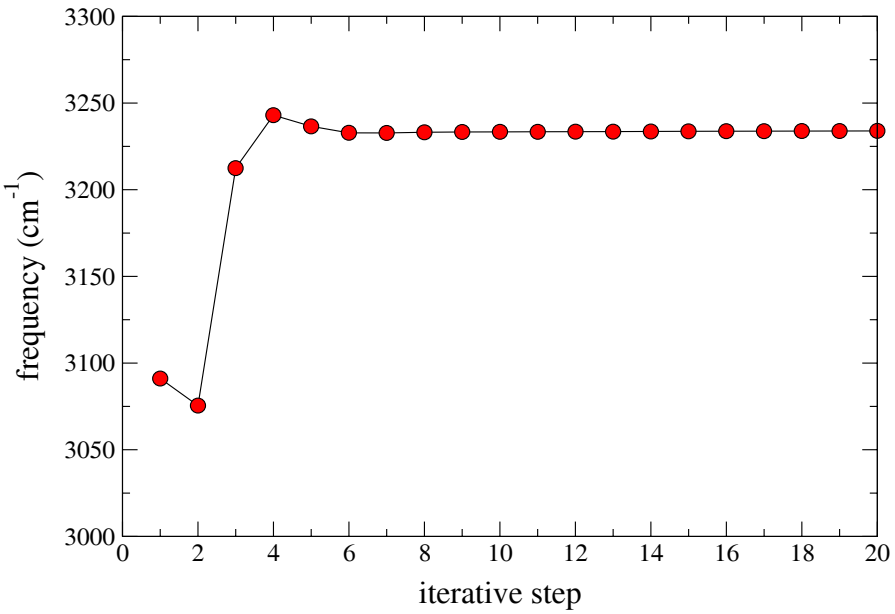

Figure 7.3: Benzene breather frequency for each iterative step.

Molecular dynamic shows that the breather solution is stable for approximately 100 periods. We note that although an essentially exact DB was constructed the frequency is higher than the expected one. Generally, in soft potentials, the DB frequency is a decreasing function of amplitude (see for example the work of Ref. [107]). In the case of $C-H$ stretching in benzene, the potential is not only soft but also non-symmetric and as we already have mentioned, the contribution of the 0_{th} harmonic is not negligible for non-symetric potentials. This is the main reason for the unexpected value of DB frequency. In the case of Silicon that is presented in the next chapter, the potential is almost symmetric and this approximation does not affect significantly the DB frequency.

7.4 Silicon Breathers

Carbon, silicon and germanium are a particularly interesting group of covalent crystals for condensed matter physics. The common feature of all tree of them is that have four valance electrons and construct diamond structure. The diamond structure is characterized by the fact that each atom has fourth neighbors. The covalent binding consists of electron pair bonds between a

given atom and each of its nearest neighbors.

In this section, we focus on crystalline Silicon (c-Si) but our studies can be extended to the other crystals as well. The main reason we choose silicon is because microelctronic technology, one of the most important achievements of our time, is dominated exclusively by this material. In fact, there are materials such as gallium arsenide (GaAs) that have better properties but silicon is the second most frequent element on the earth, and the accessible part of the earth consists of 27.5% of this element (predominantly as silicon dioxide, SiO_2). The diamond structure of c-Si is illustrated in Fig. 7.4. The distance between an atom and its nearest neighbors is 2.35 $\mathring{A}$ while the ground state energy per atom is -4.63 eV.

In general the theoretical models that have been developed for atomistic simulation in these crystals can be separated in two categories: Quantum mechanical (QM) and semi-classical approaches (SC). Although QM methods can give information regarding electronic properties of these materials that are in very good agreement with experimental observation, they are computationally very expensive and fail to describe interesting phenomena that involves large number of atoms. For that purpose, during the last two decades, a great deal of studies have been devoted in developing semiclassical-empirical potentials that give the opportunity to study clusters with large number of atoms. The main disadvantage of empirical potentials i the fact that they have to be adopted for each material separately. In this work we will use Tersoff potential for silicon [110, 111]. A brief description of the Tersoff potential is given in the following subsection.

7.4.1 Tersoff Potential

The Tersoff potential has been developed in order to include two body and three body terms. More specifically the total energy is given by:

$$E = \sum_i E_i = \frac{1}{2} \sum_{i \neq j} V_{ij},$$

where the interatomic energy V_{ij} is a modified Morse potential

$$V_{ij} = f_c(r_{ij})[Ae^{-\lambda_1 r_{ij}} + b_{ij} BAe^{-\lambda_2 r_{ij}}]$$

that includes bond-angle force through the function

$$b_{ij} = (1 + \beta_i^n \zeta_{ij}^n)^{-1/2n_i},$$

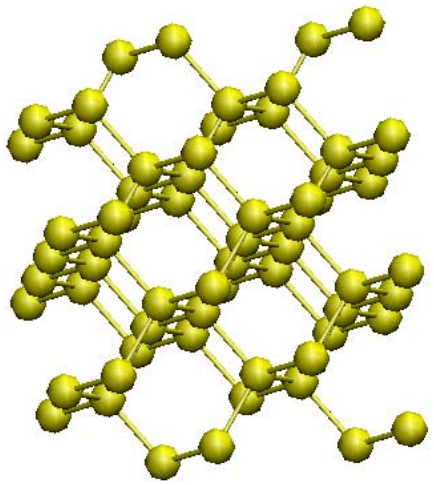

Figure 7.4: Silicon structure

$$\zeta_{ij} = \sum_{k \neq i,j} f_c(r_{ik}) g(\theta_{ijk}),\ g(\theta_{ijk}) = 1 + c_i^2/d_i^2 - c_i^2/[d_i^2 + (h_i - cos(\theta_{ijk}))^2]$$

where r_{ij} is the bond length between atoms i and j, while θ_{ijk} the angle between atoms i, j and k. The range of the force action is controlled through the cut-off function

$$f_c(r_{ij}) = \begin{cases} 1, & r_{ij} < R_{ij} \\ \frac{1}{2} + \frac{1}{2} cos[\pi(r_{ij} - R_{ij})/(S_{ij} - R_{ij})], & R_{ij} < r_{ij} < S_{ij} \\ 0, & r_{ij} > S_{ij}. \end{cases}$$

where $R = 3.0\mathring{A}$ and $D = 0.2\mathring{A}$. The other parameters of interatomic potential are explicitly given in the work of Ref. [110, 111] All c-Si properties, such as ground state energy, forces or vibrational spectrum are calculated by using MC (Monte Carlo) program written by P. C. Kelires (1990).

7.4.2 Breather generation in crystalline Silicon

Silicon vibrational spectrum constitutes of one band that is ranges from $100cm^{-1}$ to $540cm^{-1}$ (see Fig. 7.5); as a result, we will search for breather

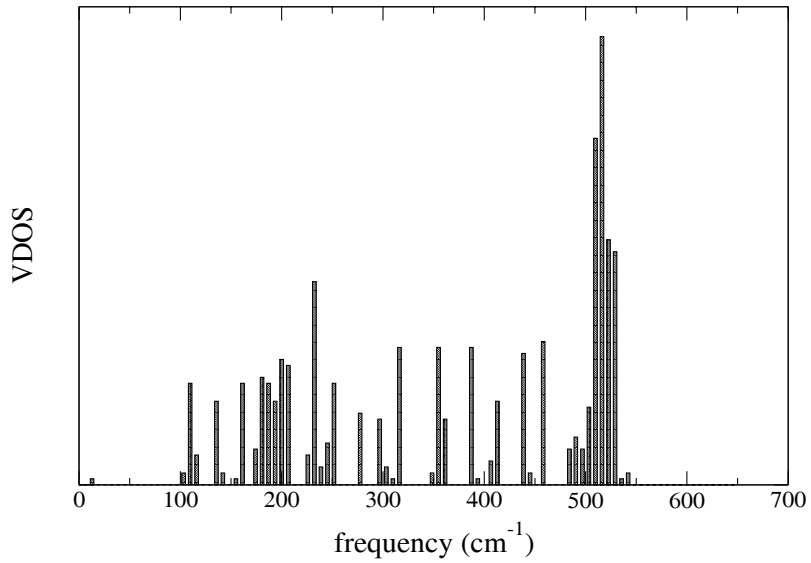

Figure 7.5: VDOS of Silicon

solutions beyond the upper limit of c-Si vibrational spectrum. We select as initial value for breather frequency $\omega_b^{(0)} = 542\ cm^{-1}$, while the magnitude of the central atom displacement Si_J is $|\delta\mathbf{R}_i^{(0)}| = 0.15$ Å, pointing towards to one of each neighbors. Using 15 harmonics in the Fourier expansion, the iterative method converged after 25 steps (Fig. 7.6) to frequency $\omega_b^{(0)} = 564\ cm^{-1}$. In Fig. 7.7 we plot a colored representation of the breather solution while in Fig. 7.8 the corresponding amplitudes of the silicon atoms. Although we initially have selected a single atom as the central site, the iterative method converged in a solution with two central atoms. The second one is the nearest neighbor in the direction toward which the Si_J was initially displaced. Both central breather atoms have the same final amplitude that is equal to 1.81 $\mathring{A}$. The six nearest neighbors to the central atoms have much smaller amplitude than either of them. The displacement of the remaining atoms falls exponentially as we move away from the breather center. This is clearly seen in the inset of Fig. 7.8 where we plot all different amplitudes of the breather solution in decreasing order. Molecular dynamic simulations show that the silicon breather is stable for very long time; in Fig. 7.9, we show the time evolution $|\mathbf{R}_J|$ for approximately 100 periods.

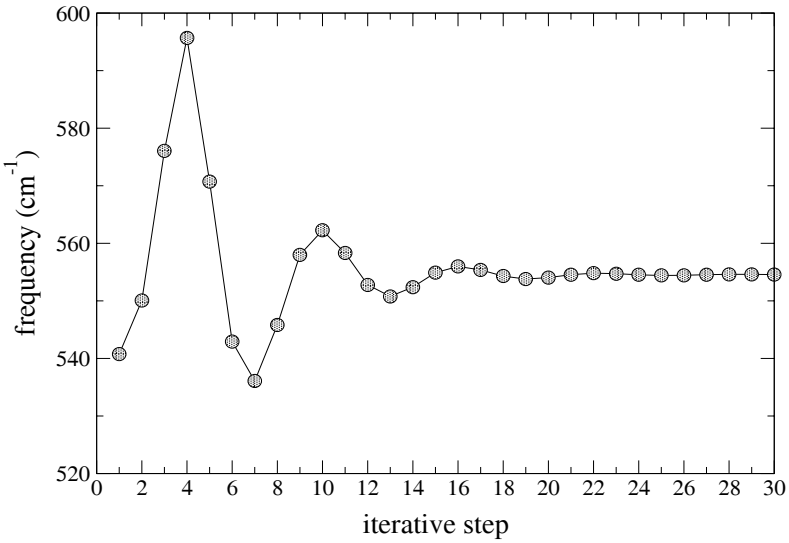

Figure 7.6: Silicon breather frequency for each iterative step.

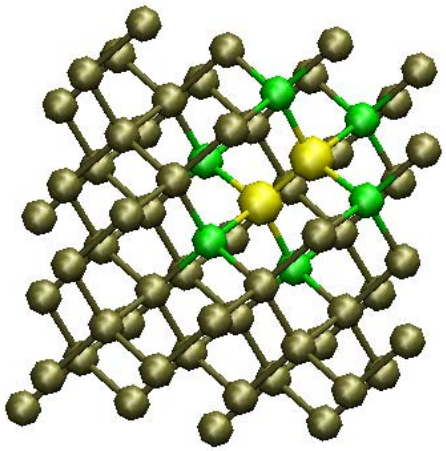

Figure 7.7: A colored representation of Silicon Breather. Yellow atoms correspond to the central breather sites, while their sixth nearest neighbors are colored with green. The rest silicon atoms are colored with grey.

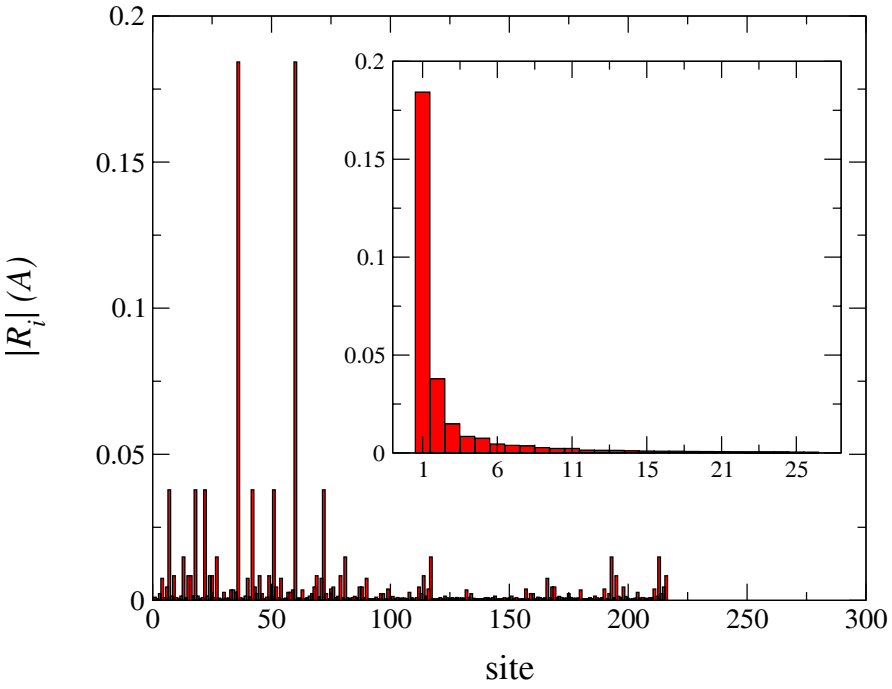

Figure 7.8: The displacement $|R_i|$ of each atom i from the equilibrium position for the breather solution shown in Fig. 7.7. In the inset, we show all the different amplitudes that appear in the breather solution, in decreasing order.

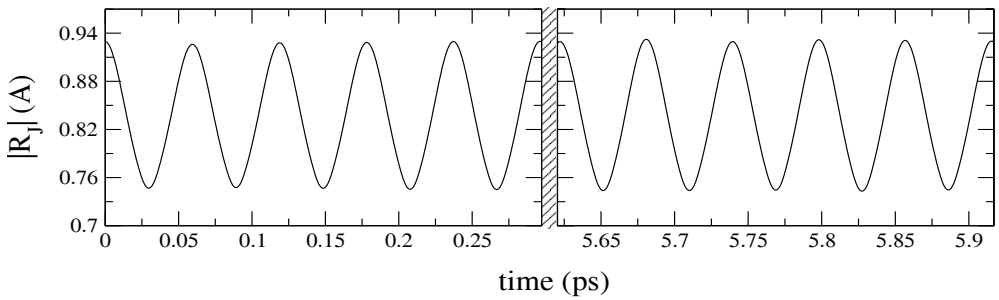

Figure 7.9: Time evolution of the central silicon atom.

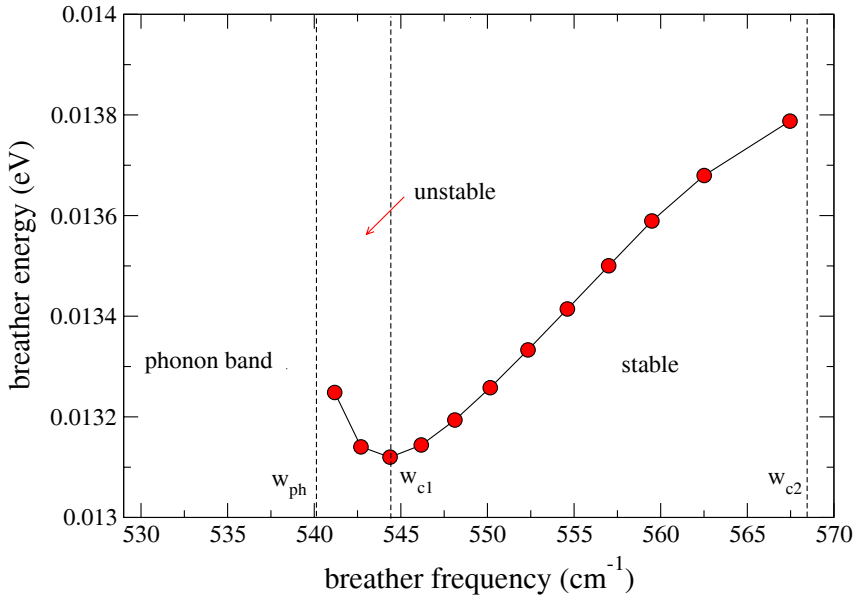

Figure 7.10: Silicon breather energy per atom as a function of its frequency

The dependence of the breather energy on frequency is shown in Fig. 7.10. We note that stable breather solutions can be found only in the interval $[\omega_{c_1}, \omega_{c_2}]$. For $\omega_b > \omega_{c_2}$ there are no solution at all. This is attributed to the behavior of the Tersoff potential in the direction that we have initially displaced the central atom; as the atom moves towards its nearest neighbor the potential becomes harder while in the opposite direction since there are no nearest neighbors the potential softens and finally becomes completely flat. The breather solution for $\omega_b > \omega_{c_2}$ corresponds to an initial displacement where the central carbon is inserted in the flat region of the potential. In this case the motion is not bounded anymore and, as a result, the generation of a breather is not possible.

As the DB frequency is diminished towards the phonon band, the breather energy decreases until ω_b becomes equal ω_{c_1}, where it has a local minimum. For $\omega_{ph} < \omega_b < \omega_{c_1}$ the breather energy increases. We have observed that although the iterative method converges to a DB in this frequency range these DB solutions are unstable. Molecular dynamic simulations show that these solutions are destroyed after approximately 10 periods. Thus we conclude that there is an energy gap in the upper edge of the phonon band and the region of the stable breather solutions. This phenomenon has also been

observed in DNLS in two and three dimensions [112].

7.4.3 Do Silicon Breathers exist at room temperature?

Both benzene and silicon breathers, have been constructed at zero temperature. The question that arises immediately is whether these solutions are stable at no zero temperatures. To test this possibility, we considered a Silicon crystal of 64 atoms, used Monte Carlo method to set initially the lattice at temperature T and subsequently added a breather solution to the lattice. The final energy of the system is very close to kT since approximately only 8 silicon atoms of the DB contribute significantly to the total lattice energy. This modification of the final temperature disappears if we assume larger silicon systems. Molecular dynamic simulations of the silicon breather presented in the previous section have shown that the DB is stable at room temperature for very long times. In Fig. 7.11 we show the breather time evolution at the room temperature for 100 DB periods. For higher temperatures, ($T \gtrsim 500$ K) the silicon breather ceases to be stable and its lifetime decreases remarkably by increasing the lattice temperature. In Fig. 7.11 we present the time evolution of breathers in two lattices at T=300 K and T= 1000 K respectively. We observe that in the latter case the DB decays after approximately 10 periods.

7.5 Conclusions

In summary, we proposed a new practical method for breather generation in real systems. The main advantage of this method is that it works independently of the complexity of the force field and the system dimensionality. It is based on the Fourier expansion of the breather but it can efficiently involve as many coefficients as needed for better accuracy of the solution. Using this method, we found DBs in benzene and crystalline Silicon and have shown that solutions are stable for very long time. Moreover, we have shown that silicon breathers can survive at room temperature. These results open possibilities for direct experimental investigation of the presence and possible utility of nonlinear localized modes in various materials.

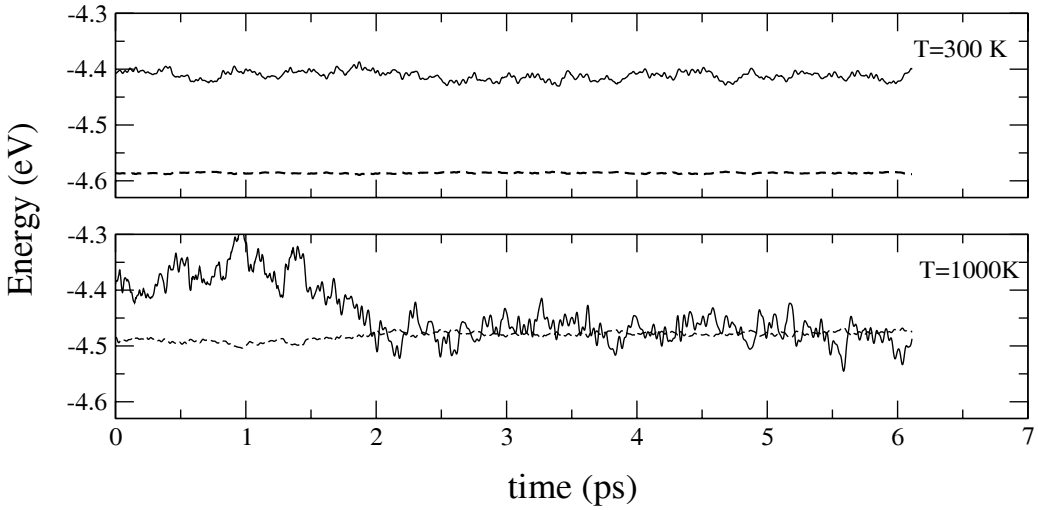

Figure 7.11: Time evolution of the breather energy (solid lines) per atom at $T = 300K$ and $T = 1000K$. The dashed lines correspond to the energy per atom of the rest sites. The breather period is 0.06 ps

List of Figures

Bibliography

[1] P. W. Anderson, Phys. Rev. **109**, 1492 (1958).

[2] *Green's functions in Quantum Physics*, E. N. Economou (Springer-Verlag, New York, 1983).

[3] L. Landau, Sov. Phys. **3**, 664 (1933).

[4] S.I. Pekar, J. Phys. (Moscow) **10**, 341 (1946).

[5] H. Frohlich, Proc. R. Soc. London, Ser. A **251**, 219 (1952).

[6] R. P. Feynman, Phys. Rev. **97**, 660 (1955).

[7] T. Holstein, Ann. Phys. (N.Y) **8**, 325, 343 (1959).

[8] D. Emin and T. Holstein, Phys. Rev. Lett. **36**, 323 (1976).

[9] Y. Toyozawa, Prog. Theor. Phys. **26**, 29 (1961).

[10] S. Aubry, A. G. Abramivici, and J. L. Raimbdault, J. Stat. Phys. **67**, 675 (1992).

[11] V. V. Kabanov and O. Yu. Manshtakov, Phys Rev. B **47**, 6060 (1993).

[12] G. Kalosakas, S. Aubry, and G.P.Tsironis, Phys. Rev. B **58**, 3094 (1998).

[13] G. Kopidakis, C. M. Soukoulis and E. N. Economou, Phys. Rev. B **51**, 1995 .

[14] Aldo H. Romero, David W. Brown, and Katja Lindenberg, Phys Rev. B **59**, 13728 (1999).

[15] Marco Zoli, Phys Rev. B **57**, 10555 (1998).

[16] H. D. Raedt and A. Lagendijk, Phys Rep. **127**, 233 (1985).

[17] A. S. Alexandrov, V. V. Kabanov, and D. K. Ray, Phys Rev. B **49**, 9915 (1994).

[18] A. Alexandrov and J. Ranninger, Phys. Rev. B **24**, 1164 (1981).

[19] D. Emin and M. S. Hillery, Phys. Rev. B **39**, 6575 (1989).

[20] Proville and S. Aubry, Physica D, Eur. Phys. J. B .

[21] *Solitons in Molecular Systems*, A. S. Davydov (Reidel, Dordrecht, 1985).

[22] A. J. Sievers and S. Takeno, Phys. Rev. Lett. **61**, 970 (1988).

[23] R. S. MacKay and S. Aubry, Nonlinearity **7**, 1963 (1994).

[24] S. Aubry, Physica D **103**, 201 (1997).

[25] Ding Chen, S. Aubry and G. P. Tsironis, Phys. Rev. Lett. **77**, 4776 (1996).

[26] G. P. Tsironis and S. Aubry, Phys. Rev. Lett. **77**, 5225 (1996).

[27] K. O. Rasmussen, S. Aubry, A. R. Bishop and G. P. Tsironis, **15**, 169 (2000).

[28] *Statistical Properties of Nonlinear Classical Models*, Maria Eleftheriou (PhD thesis, Univ. of Crete, in preperation).

[29] M. Eleftheriou and G. P. Tsironis, (unpublished).

[30] W. Z. Wang *et al*, Phys. Rev. Lett. **76**, 3598 (1996). **76**, 3598 (1996).

[31] W. Z. Wang *et al*, Phys. Rev. Lett. **80**, 3284 (1998). **80**, 3284 (1998).

[32] G. Careri *et al*, Phys. Rev. B **30**, 4689 (1984) **30**, 4689 (1984).

[33] D. M. Alexander and J. A. Krumhansl, Phys. Rev. B **33**, 172 (1986).

[34] G. Kalosakas, S. Aubry, and G. P. Tsironis, Phys. Let. A **247**, 413 (1998).

[35] B. I Swanson *et al*, Phys. Rev. Lett. **82**, 3288 (1999).

[36] H.S. Eisenberg, Y. Silberberg, R. Morandotti, A.R. Boyd, and J.S. Aitchison, Phys. Rev. Lett. **81**, 3383 (1998).

[37] R. Morandotti, U. Peschel, J.S. Aitchison, H.S. Eisenberg, and Y. Silberberg, Phys. Rev. Lett. **83**, 2726 (1999).

[38] U. T. Schwarz, L.Q. English, and A.J. Sievers, Phys. Rev. Lett. **83**, 223 (1999).

[39] E. Trias, J.J. Mazo, and T.P. Orlando, Phys. Rev. Lett. **84**, 741 (2000).

[40] P. Binder, D. Abraimov, A.V. Ustinov, S. Flach, and Y. Zolotaryuk, Phys. Rev. Lett. **84**, 745 (2000).

[41] A. Xie, L. van der Meer, W. Hoff, and R.H. Austin, Phys. Rev. Lett. **84**, 5435 (2000).

[42] N. K. Voulgarakis and G. P. Tsironis, Phys. Rev. B **63**, 14320 (2001).

[43] N. K. Voulgarakis, D. Hennig, H. Gabriel, and G. P. Tsironis, J. Phys.: Condens. Matter **13**, 9821 (2001).

[44] N. K. Voulgarakis, G. Kalosakas, A. R. Bishop, and G. P. Tsironis, Phys. Rev. B **64**, R20301 (2000).

[45] A.Bikaki, N. K. Voulgarakis, S. Aubry and G. P. Tsironis, Phys. Rev. E **59**, 1234 (1999).

[46] N. K. Voulgarakis, G.Archontis, S. Skourtis, and G. P. Tsironis, (in preperation).

[47] N. K. Voulgarakis, G. Hadjisavvas, P. C. Kelires, and G. P. Tsironis, (in preperation).

[48] St, Pneumatikos, O. Yanovitskii, Th. Fraggis, and E. N. Economou, Phys. Rev. Lett. **68**, 2370 (1992).

[49] E. N. Economou, O. Yanovitskii, and Th. Fraggis, Phys. Rev. B **47**, 740 (1993).

[50] A. V. Zolotaryuk, A. Mistriotis, and E. N. Economou, Phys. Rev. B **48**, 13518 (1993).

[51] Y. Gaididei, N. Flytzanis, A. Neuper, and F. G. Martens, Phys. Rev. Lett. **75**, 2240 (1995).

[52] Dirk Hennig, Phys. Rev. E **62**, 2846 (2000).

[53] Y. Zolotaryuk, P. L. Christiansen, and J. Juul Rasmussen, Phys. Rev. B **58**, 14305 (1998).

[54] Marco Zoli, Phys. Rev. B **61**, 41523 (2000).

[55] A. S. Alexandrov and P. E. Kornilovich, Phys. Rev. Lett. **82**, 807 (1999).

[56] L. Proville and S. Aubry, Physics D **113**, 307 (1998).

[57] Proville and S. Aubry, Physica D, Eur. Phys. J. B. **11**, 41 (1999).

[58] N. K. Voulgarakis and G. P. Tsironis, (in preparation).

[59] A.S. Davydov and N.I. Kislukha, Sov. Phys. JETP **44**, 571 (1976).

[60] A. S. Davydov, Phys. Rev. B **25**, 898 (1982).

[61] A.C. Scott, Phys. Rep. **217**, 1 (1992).

[62] O.H. Olsen, M.R. Samuelsen, S.B. Petersen, and L. Nørskov, Phys. Rev. A **38**, 5856 (1998).

[63] A.V.Zolotaryuk, P.L. Christiansen, and A.V. Savin, Phys. Rev. E **54**, 3881 (1996).

[64] P.L. Christiansen, A.V. Zolotaryuk, and A.V. Savin, Phys. Rev. E **56**, 877 (1997).

[65] A.V. Zolotaryuk, K.H. Spatschek, and A.V. Savin, Phys. Rev. B **54**, 266 (1996).

[66] S. Caspi and E. Ben-Jacob, Europhys. Lett. **47**, 552 (1999).

[67] Englander, N.R. Kallenbach, A.J. Heeger, J.A. Krumhansl, and S. Litwin, Proc. Nat. Acad. Sci. USA **77**, 7222 (1980).

[68] M. Peyrard and A.R. Bishop, Phys. Rev. Lett. **62**, 2755 (1989).

[69] G. Gaeta, C. Reiss, M. Peyrard, and T. Dauxois, Riv. Nuovo Cim. **17**, 1 (1994).

[70] *Dynamics of Proteins and Nucleic Acids*, J.A. McCammon and S.C. Harvey (University Press, Cambridge, UK, 1987).

[71] *Introduction to Protein Structure*, C. Branden and J. Tooze (Garland Pub. Inc., ADDRESS, 1991).

[72] J.P. Schneider and J.W. Kelly, Chem. Rev. **95**, 2169 (1995).

[73] S.H. Gellmann, Curr. Opin. Chem. Biol. **2**, 717 (1998).

[74] A. Agegeli, M. Bell, N. Boden *et al*, Nature **386**, 259 (1997).

[75] I.A. Nyrkova, A.N. Semenov, A. Aggeli, and N. Boden, Eur. Phys. J. B **17**, 481 (2000).

[76] S. Yomosa, Phys. Rev. A **32**, 1725 (1985).

[77] B. Gerlach and H. Lowen, Rev. Mod. Phys. **63**, 63 (1991).

[78] D. Hennig and G.P. Tsironis, Phys. Rep. **307**, 333 (1999).

[79] M. Peyrard and M.D. Kruskal, Physica D **14**, 88 (1984).

[80] M. Johansson and S. Aubry, Nonlinearity **10**, 1151 (1997).

[81] T. Cretegny and S. Aubry, Phys. Rev. B **55**, 11929 (1997).

[82] C. Baesens, S. Kim, and R.S. MacKay, Physica D **113**, 242 (1998).

[83] S. Flach and C. R. Willis, Phys. Rep. **295**, 181 (1988).

[84] A. C. Scott *et al*, Phys. Rev. B **32**, 5551 (1985).

[85] A. C. Scott *et al*, Phys. Rev. B **39**, 12883 (1989).

[86] *Nonlinear Science*, A. C. Scott (Oxford applied and engineering mathematics, Oxford, 1999).

[87] *Polarons and Excitons*, Y. Toyozawa (C. G. Kuiper and G. D. Whitfield, Oliver and Boyd, Edinbourg, 1963).

[88] K. Kladko, J. Malek, and A. R. Bishop, J. Phys.: Condens. Matter **11**, 415 (1999).

[89] H. Fehske *et al*, Physica B **281**, 673 (2000).

[90] J. T. Gammel *et al*, Phys. Rev. B **45**, 6408 (1992).

[91] D. Baeriswyl and A. R. Bishop, Phys. Scripta **19**, 239 (1987).

[92] N. K. Voulgarakis, G. Kalosakas, A. R. Bishop, and G. P. Tsironis, (in preperation).

[93] Twelve-site studies of nonadiabatic $PtCl$ chain are now available by H. Fehske, G. Wellein and A. R. Bishop, (work in progress).

[94] J. L. Marin and S. Aubry, Nonlinearity **9**, 1501 (1994).

[95] *Numerical investigation of discrete breather dynamical properties in several ordered and disordered nonlinear lattices*, Panagiotis Maniadis (PhD thesis, Univ. of Crete, 2001).

[96] M. Ibanes, J. M. Sancho, and G. P. Tsironis, Phys. Rev. E **65**, 41902 (2002).

[97] *Phase Transitions and Relaxations in Systems with Competing Energy scales*, T.Riste and D. Sherrington (Klower Academic, Dordrecht, 1993).

[98] D. W. Brown, L. Bernstein and K. Lindenberg, Phys. Rev. E **54**, 3352 (1996).

[99] S. Flach, K. Kladko and R. S. MacKay, Phys. Rev. Lett. **78**, 1207 (1997).

[100] K. Y. Tsang and K. L. Ngai, Phys. Rev. E **54**, R3067 (1996).

[101] *Nonlinear diffusion problems*, D. G. Aronson (eds A. Fasano and M.Primicerio, Springer-Verlag, Berlin, 1986).

[102] P. Allegrini, P. Grigolini and A. Rocco, Phys. Lett. A **233**, 309 (1997).

[103] C. Anteneodo and C. Tsallis, Phys. Rev. Lett. **80**, 5313 (1998).

[104] G. P. Tsironis, G. P. Tsironis, J. Phys. A **34**, 8465 (2002).

[105] S. A. Kiselev and A. J. Sievers, Phys. Rev. B **55**, 5755 (1997).

[106] J.D. Kress, A. Saxena, A.R. Bishop and R.L. Martin, Phys. Rev. B **58**, 6161 (1998).

[107] G. Kopidakis S. Aubry, Physica B **296**, 237 (2001).

[108] T. A. Halgren, J. Comp. Chem. **17**, 490 (1996).

[109] B. R. Brooks, R. E. Bruccoleri, B. D. Olafson, D. J. States, S. Swaminathan, and M. Karplus, Comp. Chem. **4**, 187 (1983).

[110] J. Tersoff, Phys. Rev. Lett. **56**, 632 (1986).

[111] J. Tersoff, Phys. Rev. B. **39**, 5566 (1989).

[112] S. Flach, K. Kladko, and R. S. MacKay, Phys. Rev. Lett. **78**, 889 (1997).